UNIVERSITÀ DEGLI STUDI DI MILANO

Scuola di Dottorato in Fisica, Astrofisica e Fisica Applicata

Dipartimento di Fisica

Corso di Dottorato in Fisica, Astrofisica e Fisica Applicata

Ciclo XXXIV

Configuration mixing investigation in germanium isotopes

Settore Scientifico Disciplinare FIS/04

Tesi di Dottorato di:
Carlotta PORZIO

Supervisore
Prof. Silvia LEONI

Co-Supervisore
Dr. Adam B GARNSWORTHY

Coordinatore
Prof. Matteo PARIS

Anno Accademico 2020-2021

Referees of the thesis:

Prof. Paul Garrett
Department of Physics, University of Guelph, N1G2W1 Guelph, Canada

Dr. Adriana Nannini
INFN Sezione di Firenze, IT-50019 Firenze, Italy

Commission of the final examination:

Prof. Silvia Leoni
Dipartimento di Fisica, Università degli Studi di Milano, 20133 Milano, Italy

Prof. Riccardo Raabe
Instituut voor Kern- en Stralingsfysica, Katholieke Universiteit Leuven, Leuven B-3001, Belgium

Prof. Peter Reiter
Institut für Kernphysik, Universität zu Köln, 50937 Köln, Germany

Final examination:

13th December 2021

Dipartimento di Fisica, Università degli Studi di Milano, 20133 Milano, Italy

Considerate la vostra semenza:
fatti non foste a viver come bruti
ma per seguir virtute e canoscenza.

Inferno XXVI, vv. 118-120

Internal illustrations:

Carlotta Porzio

Design:

Anna Lisa Varri, Carlotta Porzio

MIUR subjects:

FIS/04 – Fisica Nucleare e Subnucleare

PACS:

23.40.-s, 29.30.Kv, 21.10.Ky

CONTENTS

List of Figures **ix**

List of Tables **xiii**

Introduction **xv**

1 Theory **1**
1.1 Nuclear Deformation 1
1.1.1 Nuclear Surface Parametrization 2
1.1.2 Rotational and vibrational motion of axially symmetric deformed nuclei 3
1.1.3 Axially asymmetric nuclei 4
1.2 The Shape Coexistence Phenomenon 5
1.3 Radioactive Decay 7
1.3.1 β Decay 7
1.3.2 Electromagnetic Transitions 8
1.4 $E0$ Transitions 11
1.5 $B(E2)$ Reduced Transition Probabilities 14
1.6 The Germanium Isotopic Chain 14

2 Experimental Setup **21**
2.1 Radioactive Beam Production at TRIUMF 21
2.2 Overview of the GRIFFIN Spectrometer 22
2.2.1 The Moving Tape Collector 24
2.2.2 The GRIFFIN Clover Detectors 24
2.2.3 The PACES Array 25
2.2.4 Zero Degree Scintillator 25
2.2.5 Lanthanum Bromide Detectors 26
2.3 Data Acquisition 26
2.4 Detector Calibrations and Performances 27
2.4.1 GRIFFIN Energy Calibration 27

2.4.2 GRIFFIN Addback and Cross-Talk Corrections 28
2.4.3 GRIFFIN Summing Corrections 35
2.4.4 GRIFFIN Detection Efficiency 36
2.4.5 PACES Energy Calibration 37
2.4.6 PACES Detection Efficiency 37
2.5 Experimental Details of S1716 Beam Time 47
2.5.1 October 2017 Beam Time 48
2.5.2 September 2019 Beam Time 49

3 Analysis Techniques 51
3.1 Data Sorting 51
3.2 Coincidence Timing Conditions 51
3.3 Peak Fitting 53
3.4 Determining Electromagnetic Mixing Ratios through Angular Correlations 53
3.4.1 Angular Correlation of γ rays in cascade 53
3.4.2 Angular Correlation Analysis with the GRIFFIN Spectrometer 57
3.5 Determining Internal Conversion Coefficients 59
3.6 Determining Electric Monopole Transition Strengths 59
3.7 Determining γ-ray Decay Branching Ratios 62
3.7.1 Gating from Above 62
3.7.2 Gating from Below 63
3.7.3 Setting Upper Limits 64

4 Results and Discussion 67
4.1 Electromagnetic Mixing Ratios 67
4.1.1 Previous Results from Literature 67
4.1.2 Angular Correlation Analysis 68
4.2 Internal Conversion Coefficients 71
4.2.1 Dataset of 2017 75
4.2.2 Dataset of 2019 75
4.2.3 Internal Conversion Coefficient Results 78
4.3 Upper Limits on $E0$ $0_2^+ \rightarrow 0_1^+$ Transition Intensities 79
4.4 $E0$ Transition Strengths 80
4.5 γ-ray Decay Branching Ratios and Transition Probabilities 81
4.5.1 ^{74}Ge 81
4.5.2 ^{76}Ge 84
4.5.3 ^{78}Ge 87
4.5.4 Reduced Transition Probabilities 87
4.6 Discussion 90

5 Conclusions 95

Appendices **99**

A Radioactive-Ion Beam Intensity Calculation **99**

B Angular Correlation Analysis: Additional Plots **103**

C Angular Correlation Analysis: Covariance Matrices **107**

Bibliography **109**

Acknowledgments **115**

LIST OF FIGURES

1.1 β, γ Deformation Plane 2
1.2 Comparison of Davydov and Wilets-Jean Triaxial Models 4
1.3 Shape Coexistence across the Chart of Nuclides 5
1.4 Potential Energy Surfaces for Ni even-even Isotopes 6
1.5 Decay Scheme of ^{238}U 12
1.6 Level Schemes for the ^{70,72,74,76,78}Ge Isotopes 15
1.7 Proton and Neutron Single Particle Level Diagrams 17
1.8 Potential Energy Surfaces for Ge Isotopes calculated by Sun *et al.* 17
1.9 Potential Energy Surfaces for Ge Isotopes calculated by Nikšić *et al.* 19

2.1 Map of the Low-Energy Experimental Area of the TRIUMF-ISAC Facility 22
2.2 Solidworks Rendering of the GRIFFIN Spectrometer 23
2.3 Photograph of the GRIFFIN Array 23
2.4 Photograph of the PACES array 25
2.5 Photograph of the Zero Degree Scintillator Detector 25
2.6 GRIFFIN Crystals Energy Calibration using the Same Quadratic Calibration on the Whole Energy Range 29
2.7 GRIFFIN Crystals Energy Calibration using Two Different Quadratic Calibration below and above 1.6 MeV 30
2.8 Time Difference Spectrum for γ-γ hits recorded by GRIFFIN Crystals and BGO Shields 31
2.9 ^{152}Eu Source GRIFFIN Spectrum with and without Compton Suppression 31
2.10 ^{152}Eu Source GRIFFIN Spectrum in Singles and in Addback Mode 32
2.11 Cross-Talk Coefficients Determination for GRIFFIN using ^{60}Co Source Data 33
2.12 GRIFFIN Energy Spectrum in Addback Mode before and after Cross-Talk Correction 34
2.13 γ-Ray Coincidence Summing 35
2.14 Detection Efficiency Curve of GRIFFIN 38
2.15 $2_1^+ \rightarrow 0_1^+$ Transition of ^{72}Ge in PACES Electron Spectrum in Singles from the 2017 Dataset 41

2.16 $2_1^+ \rightarrow 0_1^+$ Transition of ^{72}Ge in PACES Electron Spectrum in Singles from the 2019 Dataset 41
2.17 PACES Electron Spectrum in Singles for ^{74}Ge from the 2019 Dataset 43
2.18 PACES Electron Spectrum in Singles for ^{76}Ge from the 2019 Dataset 43
2.19 $2_1^+ \rightarrow 0_1^+$ Transition of ^{76}Ge in PACES Electron Spectrum in γ-coincidence from the 2019 Dataset 44
2.20 $2_1^+ \rightarrow 0_1^+$ Transition of ^{78}Ge in PACES Electron Spectrum in Singles from the 2019 Dataset 44
2.21 ^{207}Bi Source PACES Electron Spectrum 46

3.1 Time Difference Spectrum for γ-γ Hits recorded by GRIFFIN 52
3.2 Time Difference Spectrum for γ-electron Hits recorded by GRIFFIN and PACES 52
3.3 γ-ray Cascade Sketch 54
3.4 Examples of Theoretical Angular Correlations $W(\theta)$ 55
3.5 Gating from Above 63
3.6 Gating from Below 64
3.7 Critical Limit 65

4.1 Angular Correlation of the $4_1^+ \rightarrow 2_1^+ \rightarrow 0_1^+$ γ-Ray Cascade of ^{78}Ge 70
4.2 Angular Correlation of the $0_2^+ \rightarrow 2_1^+ \rightarrow 0_1^+$ γ-Ray Cascade of ^{78}Ge 70
4.3 Angular Correlation of the $2_2^+ \rightarrow 2_1^+ \rightarrow 0_1^+$ γ-Ray Cascade of ^{72}Ge 72
4.4 Angular Correlation of the $2_2^+ \rightarrow 2_1^+ \rightarrow 0_1^+$ γ-Ray Cascade of ^{74}Ge 72
4.5 Angular Correlation of the $2_2^+ \rightarrow 2_1^+ \rightarrow 0_1^+$ γ-Ray Cascade of ^{76}Ge 73
4.6 Angular Correlation of the $2_2^+ \rightarrow 2_1^+ \rightarrow 0_1^+$ γ-Ray Cascade of ^{78}Ge 73
4.7 $2_2^+ \rightarrow 2_1^+$ Transition of ^{72}Ge in PACES Spectrum from the 2017 Dataset 74
4.8 $2_2^+ \rightarrow 2_1^+$ Transition of ^{72}Ge in PACES Spectrum from the 2019 Dataset 74
4.9 $2_1^+ \rightarrow 0_1^+$ and $2_2^+ \rightarrow 2_1^+$ Transitions of ^{74}Ge in PACES Spectrum from the 2019 Dataset 76
4.10 $2_2^+ \rightarrow 2_1^+$ Transition of ^{76}Ge in PACES Spectrum from the 2019 Dataset 78
4.11 $2_2^+ \rightarrow 2_1^+$ Transition of ^{78}Ge in PACES Spectrum from the 2019 Dataset 79
4.12 GRIFFIN Coincidence Energy Spectrum for ^{74}Ge, Gated on the 715-keV Transition 82
4.13 ^{74}Ge Partial Level Scheme 83
4.14 GRIFFIN Coincidence Energy Spectrum for ^{76}Ge, Gated on the 2040-keV Transition 84
4.15 ^{76}Ge Partial Level Scheme 85
4.16 GRIFFIN Coincidence Energy Spectrum for ^{78}Ge, Gated on the 927-keV Transition 86
4.17 GRIFFIN Coincidence Energy Spectra for ^{78}Ge, Gated on the 2119-keV and the 1186-keV Transitions 88
4.18 ^{78}Ge Partial Level Scheme 89
4.19 Sketch of Rotational Bands with $K = 0$ and $K = 2$ 91

A.1 Example of Tape Cycle 100

B.1 Angular Correlation of the $4_1^+ \to 2_1^+ \to 0_1^+$ γ-Ray Cascade of ^{72}Ge 104
B.2 Angular Correlation of the $4_1^+ \to 2_1^+ \to 0_1^+$ γ-Ray Cascade of ^{74}Ge 104
B.3 Angular Correlation of the $0_2^+ \to 2_1^+ \to 0_1^+$ γ-Ray Cascade of ^{74}Ge 105
B.4 Angular Correlation of the $4_1^+ \to 2_1^+ \to 0_1^+$ γ-Ray Cascade of ^{76}Ge 105
B.5 Angular Correlation of the $0_2^+ \to 2_1^+ \to 0_1^+$ γ-Ray Cascade of ^{76}Ge 106

LIST OF TABLES

1.1 Transitions Probabilities $\lambda(\sigma L)$ in terms of γ-Ray Transition Energy E_γ and of Reduced Transition Probability $B(\sigma L)$ 9

2.1 Sources Activity used in Determining the GRIFFIN Efficiency Curve 36
2.2 Summing-Out Contribution in GRIFFIN Spectrum for the $2_1^+ \rightarrow 0_1^+$ Transitions of ^{72,74,76,78}Ge 40
2.3 Conversion Electron Efficiency of the PACES crystals 42
2.4 Supplementary Measure of the Conversion Electron Efficiency of the PACES crystals for the 2019 Dataset 45
2.5 Photo-Efficiency of PACES Crystals for the 2019 Dataset 47
2.6 Halflives, Ground State Spin and Parity and Q-values for β^- decay of ^{72,74,76,78}Ga Isotopes 47
2.7 Data Collection Details for the four Ga Beams Delivered in the 2017 and 2019 Experiments 48
2.8 Detector Count Rates observed in the 2019 Experiment 50

4.1 Mixing Ratio Values for $2_2^+ \rightarrow 2_1^+$ Transitions of the ^{72,74,76,78}Ge Isotopes Measured Prior to this Work 68
4.2 Angular Correlation Results for Stretched $E2$-$E2$ γ-Ray Cascades of the ^{72,74,76,78}Ge Isotopes 69
4.3 Mixing Ratio Measurements for $2_2^+ \rightarrow 2_1^+$ Transitions of the ^{72,74,76,78}Ge Isotopes 71
4.4 Internal Conversion Coefficients Measured with the 2017 Dataset 75
4.5 Internal Conversion Coefficients Measured with the 2019 Dataset 76
4.6 Internal Conversion Coefficients Obtained Combining the 2017 and 2019 Datasets Information 79
4.7 Upper Limits on the Ratio $\lambda_{\text{ce,K}}(E2)/\lambda_\gamma(E2)$ for the $0_2^+ \rightarrow 0_1^+$ Transitions of the ^{74,78}Ge Isotopes 80
4.8 $E0$ Transition Strength Measurements for the $2_2^+ \rightarrow 2_1^+$ and $0_2^+ \rightarrow 0_1^+$ Transitions of the ^{72,74,76,78}Ge Isotopes 81

4.9 Branching Ratio Measurements for the 0_2^+ Level of ^{76}Ge 86
4.10 List of γ-Ray Decay Branches from the Newly Observed 3666-keV Level 87
4.11 Branching Ratio Measurements for the 0_2^+ Level of ^{78}Ge 90
4.12 $B(E2)$ Values for $0_2^+ \rightarrow 2_1^+$ and $0_2^+ \rightarrow 2_2^+$ Transitions 90

C.1 Covariance Matrices for the Linear Fits of the Angular Correlations of the $2_2^+ \rightarrow 2_1^+ \rightarrow 0_1^+$ γ-Ray Cascades of the ^{72,74,76,78}Ge Isotopes 108

INTRODUCTION

Protons and neutrons of atomic nuclei can arrange in both spherical and non-spherical configurations. Nuclear structure studies aim to understand the origin of such different arrangements of nucleons inside the nucleus that results from the nuclear interactions that bind them together. Nuclei can exhibit configurations which lie close in energy, yet present different deformations. Such phenomenon is referred to as *shape coexistence* and its occurrence in nuclei is thought to pervade the entire nuclear chart [1, 2]. Excited states with similar energies and same spin and parity can also mix, so that the observed states are the result of mixing of different configurations.

In this context, the structure of Ge isotopes has been widely investigated both with theoretical and experimental studies over the years, yet the understanding of their nature still remains challenging. The energy systematics of the first excited 0^+ state of the even-even Ge nuclei ($Z = 32$) comes to a minimum at $N = 40$ (^{72}Ge). The interpretation of transfer reaction data collected in the '70-'80s indicate the occurrence of maximal configuration mixing between the ground state and first excited 0^+ state in this nucleus. Such a mixing is thought to lessen moving away from $N = 40$, in correspondence with the increase of the excitation energy of the 0^+_2 state. A recent, very detailed Coulomb excitation study supports the interpretation of strong mixing of the 0^+_1 and 0^+_2 states in ^{72}Ge [3]. However, the nature of the configurations that mix and their evolution along the Ge isotopic chain is still elusive, with evidence for triaxiality [3, 4], but uncertainty on the softness along the γ degree of freedom.

Electric monopole ($E0$) transition strengths, $\rho^2(E0)$, have been identified as a sensitive probe of configuration mixing [5]. Indeed, a large $\rho^2(E0)$ value can be associated with strong mixing between nuclear configurations with different mean-square charge radii. Therefore, they are considered as a key means by which one can investigate nuclear structure and shape coexistence phenomena in nuclei.

In this thesis, a study of configuration mixing in the even-even Ge isotopes at and near stability ($A = 72, 74, 76, 78$) has been carried out through the measurement of $E0$-transition strength in $I_i = I_f$ transitions. In particular, the focus has been set on the transitions with $I = 2$, $2^+_2 \rightarrow 2^+_1$. The first and second 2^+ state belong to the ground state and "γ-vibrational" bands. In the case of an axially symmetric system, these nominally

have quantum number $K = 0$ and $K = 2$, respectively, where K is the projection of the total angular momentum of the considered nuclear state along the symmetry axis of the system. In this case, $\Delta K = 2$ and an $E0$ transition between these states would be forbidden. In the case of an axially asymmetric (*triaxial*) system, as with the Ge nuclei under investigation, K is no longer a good quantum number. Therefore, as a result of triaxiality, the states belonging to the ground state band and the so-called γ band can present multiple K components. This will be referred to in the following as K-mixing. Moreover, also configuration mixing could bring different K components to the wave function of each 2^+ state, allowing a $\Delta K = 0$ transition to proceed between the first and second 2^+ state, and thus generating $E0$ strength. The competition of two such mechanisms has been investigated in this work.

The β-decay experiments presented in this thesis have been performed at the TRIUMF laboratory (Vancouver, Canada). Radioactive ion beams of ^{72,74,76,78}Ga were produced at the Isotope Separator and Accelerator (ISAC) facility via the isotope separation on-line (ISOL) technique. These were implanted at the center of the GRIFFIN decay station and ultra-high-statistics datasets were collected. Following the β decay of the gallium isotopes, the germanium isotopes of interest (^{72,74,76,78}Ge) were populated in their excited states. In the nuclear de-excitation process, γ rays and internal-conversion electrons were emitted. In our spectroscopic study, these were detected by the GRIFFIN spectrometer and its ancillary detectors. GRIFFIN is a high-purity germanium clover detector array, meant for high-precision γ-ray spectroscopy studies [6]. In the experiments considered in this work, GRIFFIN has been equipped with ancillary detectors, including PACES, a Si(Li) crystal array for the detection of internal-conversion electrons, and the Zero Degree Scintillator, a plastic scintillator for β particles detection.

This thesis is organized as follows. In Chapter 1, an overview of the nuclear structure properties relevant for this work, such as nuclear deformation and shape coexistence, will be given. Afterwards, the radioactive processes exploited in this experimental work to populate the nuclei of interest and to perform a spectroscopic study will be briefly described. A discussion will follow on how electric monopole and quadrupole transitions can probe the nuclear structure. Finally, a review of the current experimental and theoretical knowledge on the structure of even-even Ge isotopes will be provided. Chapter 2 contains the experimental details, starting from the radioactive beam production at the TRIUMF-ISAC facility, followed by a description of the GRIFFIN decay station, its ancillary detectors, and their characterization. In Chapter 3, the analysis techniques exploited in this work will be presented. In particular, it will be focused on conversion electron spectroscopy techniques to measure internal conversion coefficients and on $\gamma\gamma$ angular correlation analyses to measure the mixing ratio δ of a γ-ray transition. The measured internal conversion coefficients and mixing ratios are, indeed, required to determine the $E0$ strength of a nuclear transition connecting states with the same spin and parity I^π, and $I > 0$. In Chapter 4, the results of the analysis performed via both γ-ray and electron spectroscopy will be presented. A discussion of such results will follow, in the greater context of both experimental and theoretical studies of configuration mixing in the even-even Ge isotopes around $N = 40$. Finally, the outcome of this work will be summarized in Chapter 5.

1

THEORY

The aim of this work is to investigate the structure of the even-even isotopes of the Ge isotopic chain at and near stability ($A = 72, 74, 76, 78$). Experimental and theoretical studies of the germanium isotopes point increasingly toward the emergence of triaxiality, configuration mixing, and shape coexistence phenomena. This work focuses on the electric monopole ($E0$) transition strengths, which can probe the mixing of nuclear configurations associated with different shapes.

In this chapter, the formalism used to describe nuclear deformations will be briefly recalled. An overview of the shape coexistence phenomenon and its occurrance in the nuclear chart will be given. A discussion will follow about the radioactive decays used to perform the spectroscopic work presented in this thesis. Further to this, a description of electric monopole and quadrupole transitions and their role in providing a fingerprint for shape coexistence in nuclei will be provided. Finally, state-of-the-art descriptions of the Ge isotopic chain will be presented, with special emphasis on recent Coulomb excitations and transfer reaction experimental results.

1.1 Nuclear Deformation

Far from closed shells, nuclei can present stable deformations. In this section, a review of the formalism used to describe nuclear deformations, rotational motion of the non-spherical systems and vibrational motion around deformed equilibrium shapes is given.

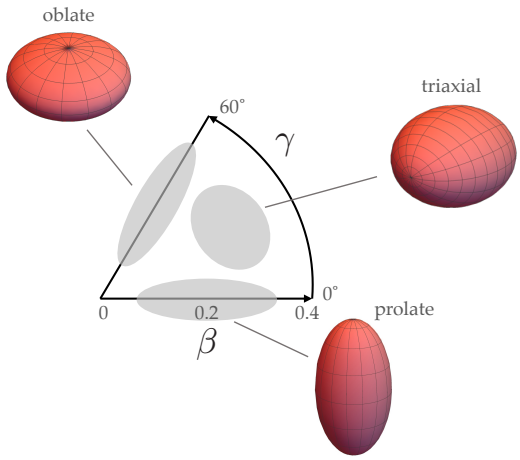

Figure 1.1: Quadrupolar deformations ($\lambda = 2$) of the nuclear surface shown in the β, γ plane. Areas of the plane corresponding to prolate deformations ($\gamma = 0°$), oblate deformations ($\gamma = 60°$) and triaxial shapes are highlighted. The typical scale for the β parameter is also indicated.

1.1.1 Nuclear Surface Parametrization

It is common to parametrize the surface of a deformed nucleus in the space-fixed system writing its radius R in terms of spherical harmonics:

$$R(\theta, \phi) = R_0 \left[1 + \sum_{\lambda\mu} \alpha^*_{\lambda\mu} Y_{\lambda\mu}(\theta, \phi) \right] \tag{1.1}$$

where R_0 is the radius of the spherical nucleus with the same volume [7, 8]. The sum over λ can be restricted to $\lambda \geq 2$, since the term $\lambda = 0$ corresponds to a change in nuclear volume relative to the spherical case, while $\lambda = 1$ describes a translation of the whole system (for small deformations). The most common deformation is quadrupolar ($\lambda = 2$), which corresponds to an ellipsoid-like shape. In such a case, there are five expansion coefficients $\alpha_{\lambda\mu}$. Of those, three represent the orientation of the body-fixed system relative to the space-fixed system; they correspond to the three Euler angles. In the body-fixed system, the five coefficients $\alpha_{\lambda\mu}$ reduce to only two real independent variables a_{20} and $a_{22} = a_{2-2}$, that together with the three Euler angles provide a full description of the system. It is possible to introduce the β, γ parameters, in place of a_{00} and a_{22}:

$$a_{20} = \beta \cos\gamma \tag{1.2}$$

$$a_{22} = \frac{1}{\sqrt{2}} \beta \sin\gamma \tag{1.3}$$

The parameter β ($\beta \geq 0$) describes the extent of the ellipsoidal deformation, while γ indicates the deviation from axial symmetry. The parameter γ ranges from $0°$ to $60°$.

A value of $\gamma = 0°$ describes an axially-symmetric nucleus with a prolate shape, while $\gamma = 60°$ corresponds to an axially-symmetric oblate shape. For values of γ between $0°$ and $60°$ the axial symmetry is lost: the shape is referred to as *triaxial*. The quadrupole deformations can thus be represented in the β, γ plane shown in Fig. 1.1.

1.1.2 Rotational and vibrational motion of axially symmetric deformed nuclei

Deformed nuclei can undergo collective rotations [7, 8]. These are characterized by a rotational angular momentum $\boldsymbol{R}$, which in the case of axially-symmetric nuclei is perpendicular to the symmetry axis. In addition to the rotational motion, the nuclear surface can vibrate around the equilibrium deformed shape. Such a vibrational motion can be described as boson excitations (phonons) that carry the intrinsic angular momentum $\boldsymbol{\lambda}$. The nuclear system will have also an intrinsic angular momentum $\boldsymbol{J}_{\text{intr}}$. Therefore, the total angular momentum will be $\boldsymbol{I} = \boldsymbol{J}_{\text{intr}} + \boldsymbol{\lambda} + \boldsymbol{R}$, with projection K along the symmetry axis. Since $\boldsymbol{R}$ has no component along the symmetry axis, only $\boldsymbol{J}_{\text{intr}}$ and $\boldsymbol{\lambda}$ will contribute to the K projection. When considering the ground state configurations of even-even nuclei, which are those relevant for this thesis, the intrinsic angular momentum of the system is $\boldsymbol{J}_{\text{intr}} = 0$, and the observed projection of the total angular momentum is $K = 0$ (no vibrational phonons are present). In the following discussion, only the case of even-even nuclei with $\boldsymbol{J}_{\text{intr}} = 0$ will be considered.

The most common low-lying vibrational excitation in deformed nuclei are quadrupole vibrations ($\lambda = 2$), similarly to the fact that the most common deformation in nuclei is quadrupolar. Consider nuclei whose equilibrium shape is axially symmetric and invariant under reflection over a plane perpendicular to the symmetry axis, as in the case of quadrupole axial deformed nuclei. The vibrational modes can be described by the projection K of the vibrational angular momentum along the symmetry axis. For symmetry reasons, there is a degeneracy of modes $\pm K$. The vibrations with $K = 0$ represent an oscillation along the β degree of freedom, hence they are referred to as β vibrations. In the case of $K = 2$ mode, the vibration occurs along the γ degree of freedom (γ vibrations) and thus the axial symmetry is instantaneously broken. The modes $K = \pm 1$ can be neglected, since they describe a rotation along an axis perpendicular to the symmetry one, therefore they do not correspond to an oscillation around the equilibrium shape.

Rotational bands can be superimposed to such intrinsic vibrational states of the nucleus, thus yielding the so-called β and γ bands in the nuclear excitation spectrum. In this case, the total angular momentum of the system will have values $I = K$, $K + 1$, $K + 2$..., except for the case $K = 0$, for which only even values of I are allowed. The energy dependence of the rotational states relative to the bandhead energy of the intrinsic excitation is:

$$E_{\text{rot}}(I) = \frac{\hbar^2}{2\mathscr{I}} [I(I+1) - K(K+1)] \tag{1.4}$$

where $\mathscr{I}$ is the moment of inertia of the system.

Despite the β and γ vibrational picture being employed for years in the description of low energy excitations in deformed nuclei, some arguments have been raised, recently, over the relevance of this interpretation for a large number of nuclear systems. This follows from critical reviews of experimental findings, which seem to point to alternative

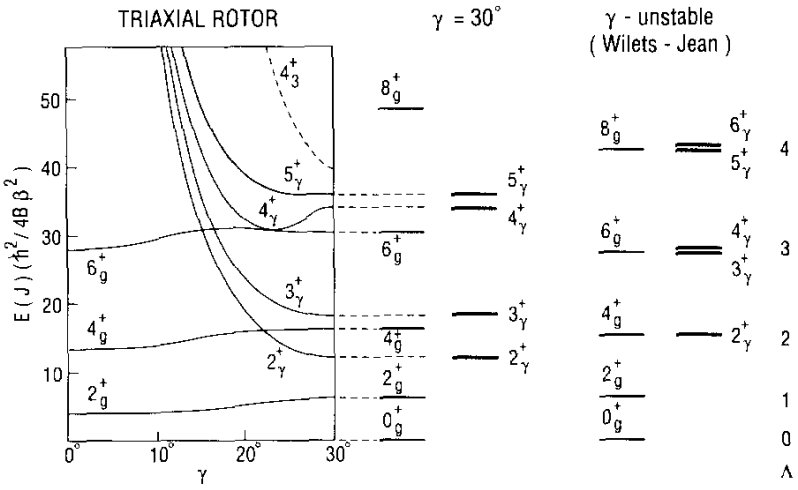

Figure 1.2: Comparison of predictions of the Davydov γ-rigid model (with $\gamma = 30°$) and of the Wilets-Jean γ-soft model for the ground state and γ bands. From the spacing of the levels in the γ band predicted with the two different models emerges that a positive staggering [$S(I) > 0$, for even I] is an indicator of a rigid triaxial rotor, while a negative one [$S(I) < 0$, for even I] is an indicator of a γ-soft system. Reprinted from Ref. [14], Copyright (1991), with permission from Elsevier.

interpretations based, for example, on shape coexistence phenomena [9, 10, 11].

1.1.3 Axially asymmetric nuclei

When considering nuclei that present a stable axial asymmetry, the description provided thus far does not hold anymore and deviations from the $I(I+1)$ rotational spectrum are observed [8]. Historically, two main models have been used to describe such nuclei. The first one has been developed by Davydov and coworkers [12]. Here, a collective potential energy $V(\gamma)$ is assumed, with a steep minimum at a certain γ value that corresponds to a triaxial deformation, hence treating the system as a *rigid* triaxial rotor. On the other hand, Wilets and Jean developed a model assuming a collective potential energy centered at a finite β value, but flat along the γ degree of freedom [13]. Namely, this model describes the deformed nucleus as free to vary along the γ degree of freedom. In this case, the nucleus is referred to as γ-*soft*.

As a means to distinguish between rigid and soft triaxiality, the energy staggering S of the γ vibrational states has been proposed [14]. This can be defined as

$$S(I) = \frac{(E_I - E_{I-1}) - (E_{I-1} - E_{I-2})}{E(2^+_{\rm gs})} \tag{1.5}$$

where the energies refer to states of the γ band of spin I, but for $E(2^+_{\rm gs})$, which indicates the energy of the ground-state band 2^+ state. It is found that such a staggering has

opposite sign in the γ-rigid and γ-soft models. In particular, for even values of I, $S(I)$ is positive in the γ-rigid case, while negative $S(I)$ values are an indication of γ softness. This can be observed in Fig. 1.2, where a comparison of predictions from the rigid and soft models is shown. The ground state band energies result similar in the two cases, but a different staggering emerges in the energies of the γ band states.

1.2 The Shape Coexistence Phenomenon

Shape coexistence in nuclei refers to the presence of low-lying nuclear states with similar excitation energy, which exhibit distinct and well-defined intrinsic shapes [1]. Extensive experimental and theoretical work has been focused on such a phenomenon over the past 60 years, that is widespread in the nuclear chart and thought to occur in nearly all nuclei, pursuing a unified description of coexistence in nuclei [2]. Figure 1.3 shows regions of the nuclear chart where evidence of shape coexistence has been found up to 2011, year of publication of the latest review on the topic by Heyde and Wood [1]. The region of interest for this thesis work ($Z = 32$, $N \sim 40$) is labelled by H in the figure.

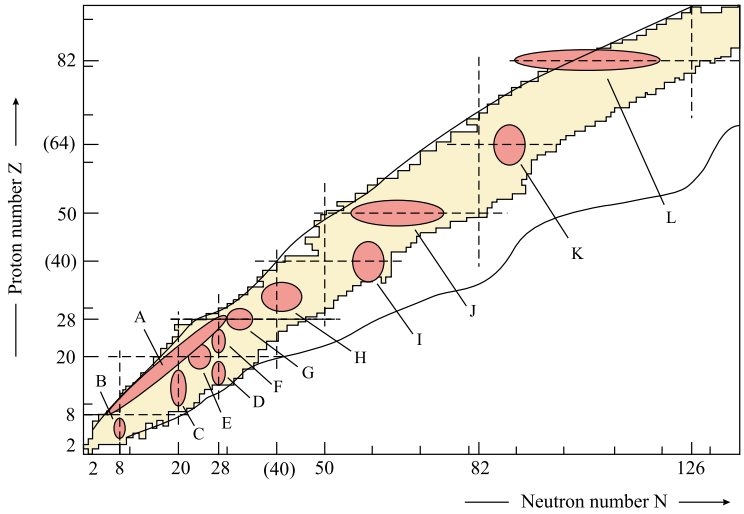

Figure 1.3: Regions of nuclear shape coexistence discussed in the latest review paper on the topic by Heyde and Wood [1] are highlighted in pink along the nuclear chart. The region of interest for this thesis work ($Z = 32$, $N \sim 40$) is labelled by H. Reprinted figure with permission from Ref. [1]. Copyright (2011) by the American Physical Society.

Nuclear theory uses two main approaches to describe this phenomenon. The first one is via microscopic shell models [15], while the second one via mean-field models [16, 17]. In the first approach, multiple particle-hole excitations across closed shells are attributed as the origin of collective nuclear excitations, which become manifested in the form of 0^+ states at low excitation energy. In the second approach, the ground state energy of the nuclear system is calculated through constrained Hartree-Fock methods [18]. The constraint is set by requiring the nuclear density to assume a certain low-multipole de-

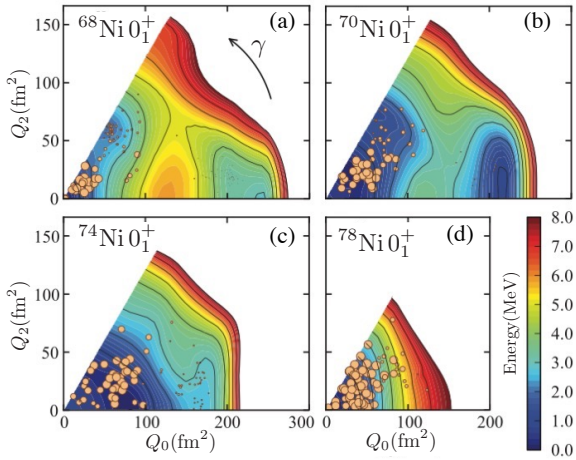

Figure 1.4: Potential energy surfaces calculated for the Ni isotopes with mass $A = 68$, 70, 74, 78, in panels (a), (b), (c) and (d), respectively. The Q_0 and Q_2 quadrupole moments here used provide an equivalent description than the β and γ parameters described in the text. The contour plot indicates the energy relative to the minimum. Figure adapted from Ref. [21].

formation, and then sampling the deformation space. In the case of quadrupole deformations, this procedure yields a potential energy surface (PES) built on the β, γ deformation plane (introduced in Fig. 1.1) [19, 20]. Shape coexistence appears in the form of multiple minima in such surfaces, which correspond to ground states associated with different nuclear deformations. Examples of calculated PESs of Ni nuclei are shown in Fig. 1.4 [21], which were obtained by the constrained Hartree-Fock method with an A3DA-like Hamiltonian [22]. In panel (a), one can observe the presence of a main minimum around spherical-oblate shapes for the nucleus ^{68}Ni, as well as a second minimum corresponding to a prolate deformation. In panel (b), a similar scenario holds for ^{70}Ni. The PESs of ^{74}Ni and ^{78}Ni in panels (c) and (d) present, instead, only one spherical minimum. In Section 1.6, PESs for the even-even Ge isotopes relevant to this work will be shown.

An interplay between theory and experiment is crucial to reach a comprehensive and unified description of shape coexistence. Spectroscopic fingerprints of nuclear deformation, and hence of shape coexistence, are measurements of $E2$ matrix elements obtained through multistep Coulomb excitation experiments and $B(E2)$ values via lifetime measurements. Strengths of $E0$ transitions are also accounted as indicators of shape coexistence, since they depend on the mixing of intrinsic configurations with different deformations. $E0$ transitions and their strength will be discussed in detail in Section 1.4, while $E2$ transitions and $B(E2)$ reduced transition probabilities will be treated in Section 1.5. First, though, an overview of the radioactive decay processes which were employed in this experimental work to populate the nuclei of interest and to investigate their nuclear transitions will be provided (Section 1.3).

1.3 Radioactive Decay

All radioactive decay processes, such as α-, β- and γ-ray decay, follow the fundamental law of radioactive decay, which reads:

$$\frac{dN}{dt} = -\lambda N \tag{1.6}$$

with N number of radioactive nuclei present at a certain time, λ decay constant of the process and λN decay rate [23, 24]. The solution of this equation, with boundary condition $N(t=0) = N_0$ initial number of particle, is:

$$N(t) = N_0 e^{-\lambda t} \tag{1.7}$$

The decay constant λ is related to the halflife $T_{1/2}$, namely the time such that the number of radioactive elements is reduced to half of its original value, via the following relation:

$$T_{1/2} = \frac{\ln 2}{\lambda} = \tau \ln 2 \tag{1.8}$$

where the lifetime τ has been defined as $\tau \equiv 1/\lambda$.

1.3.1 β Decay

In a β-decay process, a neutron is converted into a proton, or viceversa, accompanied by the emission of an electron and a neutrino or by the capture of an orbital electron [25]. The electrons emitted in such a process are also referred to as β particles. There are three basic β decay processes:

$$n \rightarrow p + e^- + \bar{\nu} \quad (\beta^- \text{ decay}) \tag{1.9}$$

$$p \rightarrow n + e^+ + \nu \quad (\beta^+ \text{ decay}) \tag{1.10}$$

$$p + e^- \rightarrow n + \nu \quad (\text{electron capture}) \tag{1.11}$$

It is possible to define the Q-value of those decays as the difference between the initial and final mass energies. If $Q > 0$, the process will spontaneosly occur (exothermic process). It follows that a free neutron can undergo a β^- decay, while a free proton decay (β^+ decay) is not energetically possible, reminding that the neutron mass is $m_n = 939.565$ MeV, while the proton mass is $m_p = 938.272$ MeV [26].

Consider the β^- decay of a nucleus of the element X with Z protons and N neutrons in its ground state (parent nucleus) into a nucleus of the element Y with $Z+1$ protons and $N-1$ neutrons in its ground state (daughter nucleus):

$${}^{A}_{Z}X_N \rightarrow {}^{A}_{Z+1}Y_{N-1} + e^- + \bar{\nu} \tag{1.12}$$

In this case the Q-value of the ground state-to-ground state process will be written as:

$$Q_{\beta^-} = M_{\mathrm{P}}c^2 - M_{\mathrm{D}}c^2 \tag{1.13}$$

where M_{P} and M_{D} indicate the parent and daugther *atomic* masses, respectively, when the differences in electron binding energy are neglected [25]. For the β^--decay process to spontaneously occur, thus, it must hold $M_{\mathrm{P}} > M_{\mathrm{D}}$. The daughter nucleus can also be populated in an excited nuclear state, that will then decay to the ground state via γ-ray decay or other electromagnetic transitions (see the following section). The β^--decay process has been exploited in this work to populate the germanium nuclei of interest in their excited nuclear states (see Chapter 2).

1.3.2 Electromagnetic Transitions

A nucleus in an excited state of energy E_i can be de-excited to a lower state of energy E_f through an electromagnetic transition. Examples of such transitions are photon emission (or γ-ray decay), internal conversion decay, two-photon emission. For the scope of this thesis, the first two mentioned processes are relevant and will be discussed in the following paragraphs.

γ-ray Decay

The most common form of nuclear de-excitation transitions for a bound nuclear system is the γ-ray decay, namely the emission of a photon. Consider a transition between initial and final states of energy E_i and E_f, respectively. For the conservation of energy, the nuclear de-excitation energy, $\Delta E = E_i - E_f$, is converted into energy of the photon, E_γ, and recoil energy of the nucleus, $E_\gamma^2/2Mc^2$ [25]. Since $\Delta E \ll Mc^2$, where Mc^2 is the rest mass of the nucleus, the approximation $E_\gamma \cong \Delta E$ holds.

Electromagnetic transitions obey angular momentum conservation. Hence, considering a transition from an initial nuclear excited state with spin I_i to a final state I_f, conservation of angular momentum implies that

$$\boldsymbol{I}_i = \boldsymbol{L} + \boldsymbol{I}_f \tag{1.14}$$

with $\boldsymbol{L}$ total angular momentum of the photon. The possible values for L are then restricted by the rule:

$$|I_i - I_f| \leq L \leq I_i + I_f \tag{1.15}$$

Note that photon emission is not allowed for monopole ($L = 0$) transitions, since photons must carry away at least one unit of angular momentum. Hence, for transitions such that $I_i = I_f$ the lowest multipole order for γ-ray decay is dipole ($L = 1$). In the case of transitions between states with spin $I_i = I_f = 0$, where only $L = 0$ is allowed by the selection rule in Eq. (1.15), single photon emission is forbidden. These states can, though, decay through internal conversion, or other processes.

In a nuclear de-excitation transition, parity must also be conserved. Therefore, if there is no change in parity between the initial and final nuclear states, the emitted radiation field must have even parity. On the contrary, if the parity changes, the radiation field must have odd parity. The parity of the radiation field of multipolarity L is defined

$\lambda(E1)$	=	1.59×10^{15}	E_γ^3	$B(E1)$
$\lambda(E2)$	=	1.22×10^{9}	E_γ^5	$B(E2)$
$\lambda(E3)$	=	5.67×10^{2}	E_γ^7	$B(E3)$
$\lambda(E4)$	=	1.69×10^{-4}	E_γ^9	$B(E4)$
$\lambda(M1)$	=	1.76×10^{13}	E_γ^3	$B(M1)$
$\lambda(M2)$	=	1.35×10^{7}	E_γ^5	$B(M2)$
$\lambda(M3)$	=	6.28×10^{0}	E_γ^7	$B(M3)$
$\lambda(M4)$	=	1.87×10^{-6}	E_γ^9	$B(M4)$

Table 1.1: Transition probabilities $\lambda(\sigma L)$ for γ-ray transitions of electric (E) or magnetic (M) character and different multipolarities L written in terms of the γ-ray transition energy E_γ and of the reduced transition probability $B(\sigma L)$. $\lambda(\sigma L)$ are expressed in s^{-1}, $B(EL)$ in units of $e^2\mathrm{fm}^{2L}$, $B(ML)$ in units of $\mu_N^2\mathrm{fm}^{2L-2}$, while the transition energies E_γ are in MeV [29].

as:

$$\pi(ML) = (-1)^{L+1} \tag{1.16}$$

$$\pi(EL) = (-1)^{L} \tag{1.17}$$

where E and M define the electric or magnetic character of the field.

For a γ-ray transition that can have mixed multipolarities, L and L', it is possible to define the mixing ratio δ as the ratio of the reduced matrix elements for each multipole operator:

$$\delta_\gamma \equiv \frac{\langle I_f||\sigma' L'||I_i\rangle}{\langle I_f||\sigma L||I_i\rangle} \tag{1.18}$$

where I_i and I_f are the initial and final state of the transition, respectively, $\sigma = E$ or M indicates either electric or magnetic radiation and, by convention, L' is taken as greater than L [27]. Hence, δ^2 expresses the ratio of the transition probabilities of the two competing de-excitation modes, σL and $\sigma' L'$. The sign of δ depends on the definition of the reduced matrix elements. In this work, the sign convention introduced by Krane and Steffen is adopted [28].

Given a γ-ray transition of character σ and multipolarity L, it is possible to define its reduced transition probability as [29]:

$$B(\sigma L; I_i \to I_f) = \frac{1}{2I_i + 1}|\langle\psi_f||m(\sigma L)||\psi_i\rangle|^2 \tag{1.19}$$

where $|\psi_i\rangle$ and $|\psi_f\rangle$ indicate the initial and final states with spin I_i and I_f, respectively, and $m(\sigma L)$ is the multipole operator. Such reduced transition probabilities are connected to the transition probabilities $\lambda(\sigma L)$ by the relationships listed in Table 1.1.

Given the relationship between the reduced transition probability $B(\sigma L)$ and the transition probability $\lambda(\sigma L)$ and reminding that the lifetime τ of a nuclear states is defined as $\tau \equiv 1/\lambda$, it is possible to extract $B(\sigma L)$ values from lifetime measurements. Note

that if the nuclear state can be de-excited via multiple decay branches, one will need to use the *partial* lifetime τ_γ connected to the γ-ray decay branch considered to calculate $\lambda(\sigma L)$. The partial lifetime is defined as following:

$$\tau_\gamma = \tau \frac{I_{\text{total}}}{I_\gamma(\sigma L)} \tag{1.20}$$

where $I_\gamma(\sigma L)$ is the intensity of the γ-ray decay branch of interest and I_{total} is the sum of the intensities of all the possible decay branches. In case of γ-ray transitions with mixed multipolarities, the mixing ratio δ defined in Eq. (1.18) must be taken into account when determining the intensity $I_\gamma(\sigma L)$.

The reduced transition probabilities can be expressed in *Weisskopf units* (from the name of Weisskopf, who firstly introduced them [30]), also referred to as single-particle estimates. These are connected to the usual units by [29]:

$$B_{\text{W}}(EL) = \frac{1}{4\pi}\left(\frac{3}{L+3}\right)^2 1.2^{2L} A^{2L/3} \quad e^2\,\text{fm}^{2L} \tag{1.21}$$

$$B_{\text{W}}(ML) = \frac{10}{\pi}\left(\frac{3}{L+2}\right)^2 1.2^{2L-2} A^{(2L-2)/3} \quad \mu_N^2\,\text{fm}^{2L-2} \tag{1.22}$$

where the subscript W stands for Weisskopf. They represent an estimate of the reduced transition probability under the assumption of treating single-particle configurations. In the following, the Weisskopf units will be adopted and will be indicated by W.u.

Internal Conversion Decay

The internal conversion decay competes with γ-ray emission in nuclear de-excitation [25]. In such a process, an atomic electron is emitted from the nucleus due to the Coulomb interaction between the atomic electrons and the protons in the nucleus [31]. The kinetic energy of the emitted conversion electron is equal to the difference between the nuclear de-excitation energy, ΔE, and the binding energy of the electron, B_{e}, that must be supplied to liberate the electron out of its shell:

$$T_{\text{ce}} = \Delta E - B_{\text{e}} \tag{1.23}$$

The electron binding energy B_{e} varies with the atomic shell considered. Hence, conversion electrons emitted from different shells will have a different kinetic energy. A conversion electron spectrum will thus present multiple discrete peaks corresponding to each nuclear transition, in contrast with a γ-ray spectrum, where only one peak corresponds to a certain nuclear transition. The multiple components appearing in the conversion electron spectrum for each transition are labelled according to the electronic shell from which the electrons are emitted, namely K, L, M, and so on.

It is useful to define the *internal conversion coefficient* α as:

$$\alpha = \frac{\lambda_{\text{ce}}}{\lambda_\gamma} \tag{1.24}$$

where λ_{ce} is the internal conversion decay probability for a given transition, and λ_γ is the γ-ray decay probability. Hence, the coefficient α represents the probability of decaying through electron emission relative to photon emission. It is possible to define also *partial* internal conversion coefficients, that indicate the probability of emitting an electron from a specific shell relative to γ-ray decay:

$$\alpha = \alpha_{\text{K}} + \alpha_{\text{L}} + \alpha_{\text{M}} + ... \tag{1.25}$$

It can be shown that the partial conversion coefficients, when energetically possible, decrease like $1/n^3$, with n principal quantum number of the bound electron wave function ($n = 1$ for the K-shell, $n = 2$ for the L-shell, and so on) [25]. Therefore, α will be dominated by the terms α_i associated with the most inner shells.

1.4 $E0$ Transitions

$E0$ transitions occur between states of the same spin and parity $I^\pi \rightarrow I^\pi$. In such a transition, the nucleus can be de-excited via internal conversion by transferring energy, zero units of angular momentum and no parity change to an atomic electron [31]. The internal conversion decay has been previously described in Section 1.3.2. Competing mechanisms for $E0$ transitions to occur are electron-positron internal-pair formation, if the transition energy is above $2m_ec^2 = 1.022$ MeV, and the extremely rare two-photon emission [5]. Only transitions with energy less than $2m_ec^2$ are considered in this experimental work, therefore only $E0$ transitions occurring via internal conversion decay are relevant to the discussion and will be treated in the following.

The monopole operator $m(E0)$ resulting from a multipole expansion of the Coulomb interaction hamiltonian between the atomic electrons and the nuclear protons can be written, to first order, as [29]:

$$m(E0) = \int \rho_{\text{ch}}(\boldsymbol{r}) r^2 d\boldsymbol{r} \tag{1.26}$$

where $\rho_{\text{ch}}(\boldsymbol{r})$ indicates the nuclear charge density, assumed as a continuous distribution. In the case of a point-like charge distribution, this reduces to $m(E0) = e\sum_k r_k^2$, where the sum is extended over all the nuclear protons, e is the unit of electrical charge and r_k is the position of the k^{th} proton. The matrix element of the electric monopole operator between an initial state $|i\rangle$ and a final state $|f\rangle$ is usually expressed in dimensionless units, according to the notation introduced in Ref. [32], as the *E0 transition strength* ρ:

$$\rho(E0) = \frac{\langle f|\, m(E0)\, |i\rangle}{eR^2} \tag{1.27}$$

where $R = r_0 A^{1/3}$ (r_0=1.2 fm) indicates the radius of an ideal nucleus with a sharp spherical surface [8]. The square of $\rho(E0)$ is usually reported in literature to prevent sign ambiguity. Since typical values of $\rho^2(E0)$ are of the order of $10^{-1} - 10^{-3}$, measured $E0$ transition strengths are usually reported in milliunits [$\rho^2(E0) \times 10^3$].

The measured transition probability λ for $E0$ conversion can be related to the $E0$ tran-

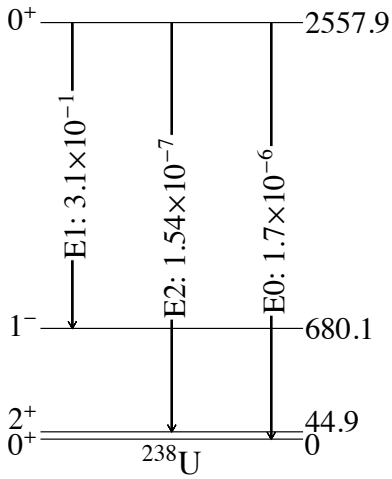

Figure 1.5: Decay scheme of the ^{238}U nucleus. Data are taken from literature [34, 35, 36]. The $E0$ strength, $\rho^2(E0)$, is reported in milliunits, while reduced transition probabilities, $B(E2)$ and $B(E1)$, are in W.u.

sition strength via:

$$\lambda(E0) = \Omega\rho^2(E0) \tag{1.28}$$

where Ω is an atomic electron factor independent of the nuclear properties which can be calculated [33].

It is possible to relate the nuclear structure information contained in $\rho^2(E0)$ values to theoretical models. Hence, a measurement of $\rho^2(E0)$ can provide information about the nuclear states involved in the transition. As such, these measurements have been indicated as a probe of shape coexistence in nuclei in the most recent review on the topic by Heyde and Wood [1]. In particular, they argue that nuclei presenting coexisting deformations will exhibit large $\rho^2(E0)$ values among such configurations when these become mixed.

To illustrate such an idea, we shall consider a simple two-state mixing model. Let $\left|0_1^+\right\rangle$ and $\left|0_2^+\right\rangle$ be two nuclear configurations with different shape. The observed initial and final $|0_i^+\rangle$ and $|0_f^+\rangle$ states can be associated with a mixing of such configurations:

$$|0_i^+\rangle = \alpha\left|0_1^+\right\rangle + \beta\left|0_2^+\right\rangle \tag{1.29}$$

$$|0_f^+\rangle = -\beta\left|0_1^+\right\rangle + \alpha\left|0_2^+\right\rangle \tag{1.30}$$

where the mixing coefficients α and β satisfy $\alpha^2 + \beta^2 = 1$. The $E0$ transition strength

among $|0_i^+\rangle$ and $|0_f^+\rangle$ can be written as:

$$\rho(E0) = \frac{\langle 0_f^+|m(E0)|0_i^+\rangle}{eR^2} = \\ = \frac{1}{eR^2}\Big[\alpha\beta\Big(\langle 0_1^+|\, m(E0)\,|0_1^+\rangle - \langle 0_2^+|\, m(E0)\,|0_2^+\rangle\Big) \\ + (\alpha^2-\beta^2)\,\langle 0_2^+|\, m(E0)\,|0_1^+\rangle\Big] \tag{1.31}$$

Suppose that the mixing among the different shape configurations is weak. The first two terms will thus be negligible, since $\alpha\beta \simeq 0$. The third term will be negligible as well, since in the case of well distinct shape configurations it will hold that $\langle 0_2^+|\, m(E0)\,|0_1^+\rangle \simeq 0$, given the different localization of the $|0_1^+\rangle$ and $|0_2^+\rangle$ wavefunctions in the deformation space. Therefore, in the case of weak mixing among configurations with different shapes $\rho^2(E0) \simeq 0$. The best example of such a case is given by the ^{238}U nucleus, which presents the slowest $E0$ transition known between the excited 0^+ state at 2558 keV and the ground state [$\rho^2(E0; 0^+_{2558} \rightarrow 0^+_{\rm gs}) \times 10^3 = 1.7 \times 10^{-6}$, see Fig. 1.5]. Here, the two 0^+ states are associated with different minima of the PES, separated by a high potential barrier.

Consider now a strong mixing scenario, where $\alpha \simeq -\beta \simeq 1/\sqrt{2}$. As before, $\langle 0_2^+|\, m(E0)\,|0_1^+\rangle \simeq 0$. Now, though, $\alpha\beta \simeq 1/2$. Therefore, in this approximation the $E0$ strength will be:

$$\rho(E0) \simeq \frac{1}{2}\frac{1}{eR^2}\Big(\langle 0_1^+|\, m(E0)\,|0_1^+\rangle - \langle 0_2^+|\, m(E0)\,|0_2^+\rangle\Big) \tag{1.32}$$

Reminding the parametrization of the nuclear surface $R = R(\theta, \phi)$ (see Eq. (1.1)), it can be shown that the $E0$ transition connecting mixed states with different axial quadrupole deformations (namely associated with different mean-square charge radii $\langle r^2\rangle$) is proportional to the difference in mean-square charge radius between the two configurations [5]:

$$\rho(E0) \simeq \alpha\beta\Delta\langle r^2\rangle \tag{1.33}$$

Therefore, this simple model illustrates how a large $\rho^2(E0)$ can be a remarkable indicator of a shape difference in the two mixing states, or a large amount of configuration mixing, or both the effects. This model has been used, for example, to effectively describe the large $\rho^2(E0)$ value measured for the $0_3^+ \rightarrow 0_2^+$ transition in ^{96}Sr [$\rho^2(E0)_{\rm exp} \times 10^3 = 185(50)$] [5].

Theoretical efforts have been recently devoted by Brown and collaborators to developing a microscopic model to predict $E0$ strength values [37]. This combines a configuration-interaction model to determine orbital occupations with an energy-density functional model with a Skyrme-type interaction, that accounts for the monopole polarization of the core protons by the valence neutrons. A shell-model description that lacks such a first-order correction would otherwise fail in the description of the $E0$ strength. The results of the model of Brown, which depend on the Skyrme parameters, predict $E0$ matrix elements for $0^+ \rightarrow 0^+$ transitions which are generally a factor of 2 smaller than the experimental values, possibly due to a second-order correction not included in the

calculations that could result in an effective charge.

This model was recently used to calculate the $E0$ matrix elements for the $2_2^+ \rightarrow 2_1^+$ transitions in ^{58,60,62}Ni isotopes. When considering such $I > 0$ transitions, the calculations significantly underestimate the experimental values, despite the success for the $0^+ \rightarrow 0^+$ cases [38].

Measurements of $E0$ strengths for $I^\pi \rightarrow I^\pi$ transitions, and in particular for $I > 0$ transitions, throughout the entire nuclear chart are still lacking. An experimental systematic study of $\rho^2(E0)$, therefore, will be crucial to benchmark theoretical models to reach an effective description of $E0$ transitions and to fully understand the structure of low-lying intrinsic excitatations in nuclei that appear as 0^+ states.

1.5 $B(E2)$ Reduced Transition Probabilities

The diagonal matrix element of the electric quadrupole operator $m(E2)$ is directly proportional to the quadrupole deformation of the state considered. This is the reason why, as mentioned in Section 1.2, $E2$ matrix elements measured via multistep Coulomb excitation experiments are the most direct spectroscopic fingerprint of shape coexistence in nuclei, since they can directly probe the nuclear deformation of a given nuclear state. Nondiagonal $E2$ matrix elements, and thus the reduced transition probabilities $B(E2)$ [see Eq. (1.19)] obtained through lifetime measurements, provide information about electric quadrupole transitions that can be effectively compared with robust theoretical calculations, to validate the description of the observed nuclear system.

$B(E2)$ values for inter-band transitions between collective states can amount to tens of W.u. One mechanism that could result in a hindrance of such transitions [$B(E2) < 1$ W.u.] is the localization of the wavefunctions of states at spin 0 in different minima of the PES which are separated by a high potential barrier, i.e., to highly non-mixed configurations. The extreme case of such a scenario is that of the ^{238}U isotope, already discussed in Section 1.4 for its slow $E0$ transition between the 0^+ state at 2558 keV and the ground state. Here, a highly hindered $E2$ transition has been observed between states belonging to the two bands which lie in different minima of the PES [35, 36]. In particular, $B(E2; 0^+_{2558} \rightarrow 2^+_{\text{gs}}) = 1.5 \times 10^{-7}$ W.u., where the subscript *gs* indicates the 2^+ state belonging to the ground state band (see Fig. 1.5). This phenomenon has been referred to as *shape isomerism*, to indicate that the retardation of the transition is due to crossing the potential energy barrier between two minima with different shape [39]. If the configurations are mixed, instead, no retardation will be observed, due to a higher overlap of the considered wavefunctions. Therefore, $B(E2)$ values provide a complementary description to the $\rho^2(E0)$ strengths and allow to make fruitful comparisons with theoretical models. In particular, large-scale shell-model calculations can effectively predict $B(E2)$ values, providing a microscopic description of the structure of nuclei.

1.6 The Germanium Isotopic Chain

Even-even germanium isotopes near and at stability are the focus of this thesis work (A = 72, 74, 76, 78). Low-lying 0^+ states are indicators of shape coexistence in such

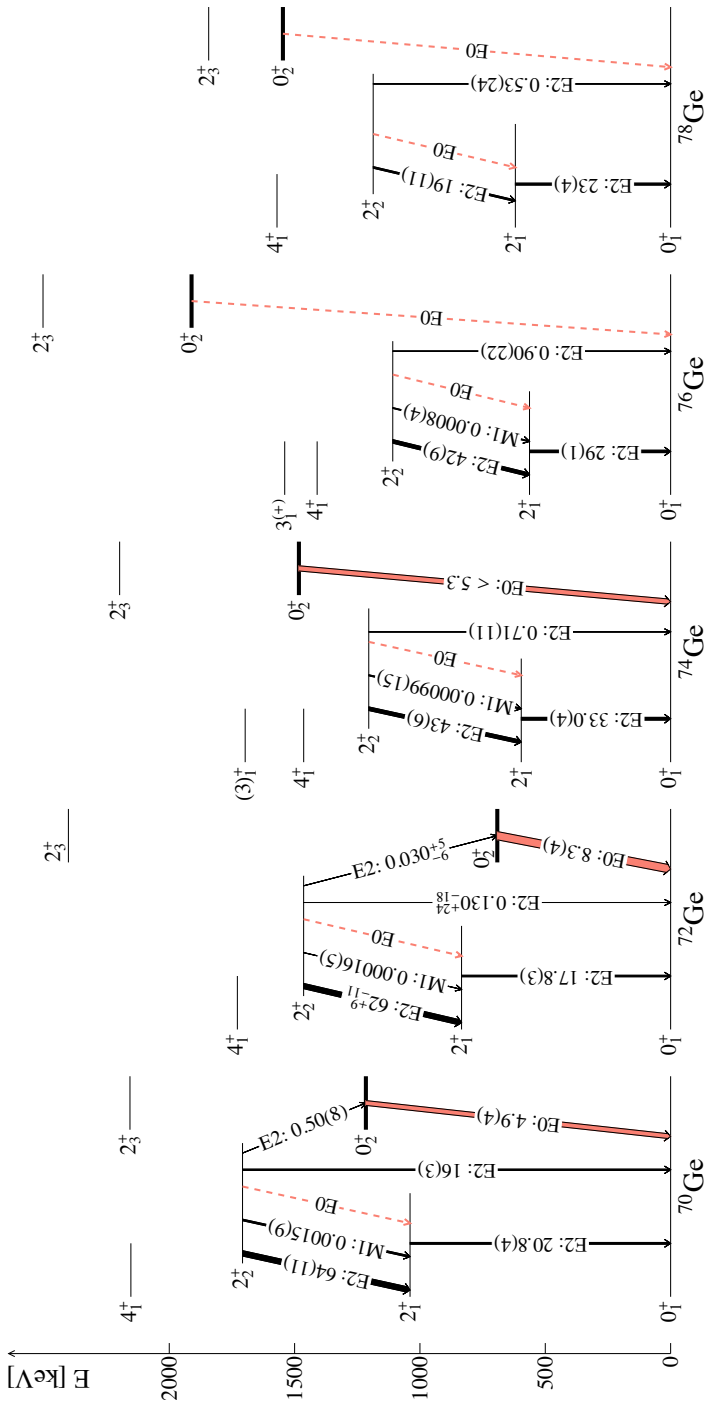

Figure 1.6: Partial level schemes for the nuclei ^{70,72,74,76,78}Ge. Data are taken from literature [40, 41, 42, 43, 44, 45]. The 0_2^+ states are highlighted in bold. Reduced transition probabilities $B(E2)$ and $B(M1)$ are reported in W.u., while $E0$ strength $\rho^2(E0)$ values are in milliunits. The dashed lines corresponding to $E0$ $I^\pi \rightarrow I^\pi$ transitions indicate that no measurements of $\rho^2(E0)$ have been performed prior to this work.

nuclei. However, details on the mixing between different configurations are still unclear. In this section, an overview of recent theoretical and experimental studies on these nuclei will be provided.

The energy of the first excited 0^+ state of even-even Ge nuclei around stability varies parabolically, coming to a minimum in ^{72}Ge, at the $N = 40$ subshell closure. In this nucleus, the 0_2^+ state becomes the first excited state, as can be observed in Fig. 1.6.

Numerous transfer reaction studies have been performed to investigate ^{72}Ge, among which one-proton stripping reactions [46], two-neutron pickup reaction [47], α-particle stripping reactions [48] and others [42]. The results of such studies is summarized in the review by Heyde and Wood on shape coexistence phenomena [1]. The interpretation of the transfer-reaction data is that the ground state and excited 0^+ states of ^{72}Ge are strongly mixed. In ^{70}Ge a weakly deformed ground state coexists with a very deformed excited configuration, while in both ^{74,76}Ge there is a deformed ground state with a close to spherical excited configuration. This picture is mostly consistent with results obtained via Coulomb excitation studies.

A detailed multi-step Coulomb excitation study of ^{72}Ge was recently performed at the Argonne National Laboratory [3]. An extensive set of $E2$ and $M1$ matrix elements has been determined (46 in total). Through the Kumar–Cline sum rule analysis, the quadrupole invariants $\langle Q^2 \rangle$ and $\langle \cos 3\delta \rangle$ have been derived for states in the ground state band and in the quasi-γ band, up to $8\hbar$ spin. The parameters Q and δ provide a description of the nuclear quadrupole deformation equivalent to the β and γ parameters introduced in Section 1.1.1, indicating the overall quadrupole deformation and deviation from axial symmetry, respectively. Results of this analysis indicate that the ground-state band presents a triaxially-deformed shape. A similar conclusion is drawn for the quasi-γ band, for which similar $\langle Q^2 \rangle$ and $\langle \cos 3\delta \rangle$ values are obtained. The 0_2^+ state is also found to present almost the same $\langle Q^2 \rangle$ value as the 0_1^+ ground state. This could be interpreted as a consequence of mixing of two different configurations. Configuration mixing calculations within a two-triaxial-rotor model – the coupled generalized triaxial rotor model (GTRM$\times$2) [49] – were performed, which manage to reproduce a number of $E2$ matrix elements. Therefore, the coexistence of two triaxial structures associated with the 0_1^+ and 0_2^+ states can describe the nature of such states. In this interpretation, maximum mixing of the wavefunctions associated with the two 0^+ states would be required. An analogous multi-step Coulomb excitation study was performed for ^{76}Ge by the same group [4]. Also in this case, data were analyzed with the Kumar–Cline sum rule analysis, strongly indicating rigid triaxial deformation both in the ground-state and in the γ-band of this nucleus. Triaxial rigidity is suggested also by the observed staggering of the γ band. In particular, the energy staggering $S(4)$ [defined in Eq. (1.5)] is positive [50]. In addition, a spectroscopic study of ^{78}Ge via multinucleon transfer recently carried out at the Argonne National Laboratory has identified an unusual decay sequence within a band of $I^\pi = 2^+, 3^+, 4^+, 5^+$ and 6^+ states [51]. In such a band, transitions of $\Delta I = 1$ are enhanced, while those of $\Delta I = 2$ are quenched, in contrast with intra-band transitions in γ bands of neighbouring Ge isotopes. These observations are consistent with predictions of the Davydov rigid-triaxial rotor model [12], assuming the maximum degree of asymmetry, namely $\gamma = 30^\circ$. Such a band has been indicated as κ band, in order to high-

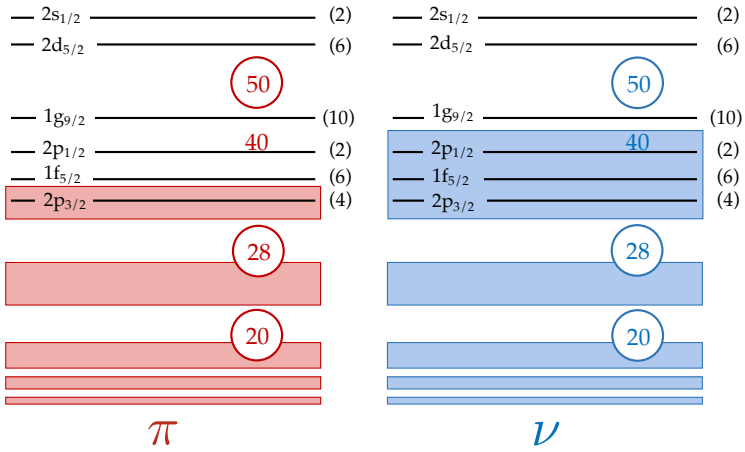

Figure 1.7: Proton (π) and neutron (ν) single particle level diagrams, relevant for the $Z = 32$, $N \sim 40$ region. The spacing between the orbitals is not to scale. Numbers of nucleons allowed in each level are written in parentheses. The coloured regions indicate occupied orbitals in the ground state configuration of ^{72}Ge ($Z = 32$, $N = 40$).

light its peculiarities relative to the so-called γ bands in neighbouring nuclei. Even in this case, the energy staggering also support the rigid triaxiality description [$S(4) > 0$]. The results of these three recent studies on ^{72,76,78}Ge are consistent with the conclusions drawn from the transfer reaction data. However, they provide evidence of triaxiality in such nuclei.

Extensive theoretical efforts have also been devoted to the study of the even-even Ge isotopes. Large-scale shell-model calculations that use the f_5pg_9-shell model space (see Fig. 1.7) predict effectively the energy systematics of the 0_2^+ states in Ge nuclei up to $N = 44$ [53]. This behaviour is thought to be associated with a reduction of the gap between the $2p_{1/2}$ and $1g_{9/2}$ orbitals, which results in a 0_2^+ state consistent with a two-neutron excitatation from the fp orbitals to the $1g_{9/2}$ orbital. Mean-field approaches have also been used to investigate the even-even Ge isotopes structure. Constrained triax-

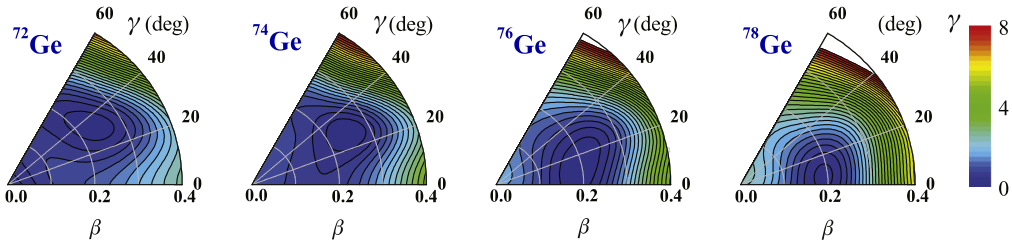

Figure 1.8: Potential energy surfaces for Ge isotopes calculated by Sun *et al.* by constrained energy density functional theory with the PC-PK1 functional. The energy scale is in MeV. Reprinted figure from Ref. [52].

ial covariant density functional (CDFT) calculations with the PC-PK1 functional predict ^{74}Ge as being triaxial in its ground state with a γ-soft potential, as can be seen in the PES shown in Fig. 1.8, both for this and for the neighbouring Ge isotopes [52]. ^{76,78}Ge show more rigid potentials, where the minimum is shifted toward prolate shapes. In the same publication, calculations within the five-dimentional collective Hamiltonian model based on the aforementioned CDFT results are also presented. These predict γ parameter values for the ground states of ^{72,74,76,78}Ge which are all consistent with a triaxial description of such configurations ($\gamma = 27.7°$, $26.7°$, $24.0°$ and $22.2°$, respectively) and are in good agreement with the available experimental results from Coulomb excitation studies for ^{72,74,76}Ge. γ softness in the potential of ^{74}Ge can be drawn also from a different study, where self-consistent relativistic Hartree–Bogoliubov theory is used to obtain PESs of even-even Ge isotopes [54]. These PESs are shown in Fig. 1.9. In these calculations there is a tendency to γ softness also in ^{76,78}Ge.

As previously discussed in Section 1.4, electric monopole transition strengths are a sensitive probe of configuration mixing, which seem to play a significant role in determining the nature of even-even Ge isotopes structure near $N = 40$. The transition between the 2_2^+ to 2_1^+ states is from the γ bandhead (nominally $K = 2$ for an axially symmetric nucleus) to the ground-state band (nominally $K = 0$). $E0$ transitions involving $\Delta K = 0$ are allowed, whereas $E0$ transitions between states with $\Delta K = 2$ are forbidden. In a completely pure configuration there would be zero $E0$ strength between the 2_2^+ and 2_1^+ states, if these states were the 2^+ γ-bandhead and the 2^+ belonging to the ground-state band, respectively. Configuration mixing, though, can occur between states of the same spin and parity, and if there are components of the wavefunctions where $\Delta K = 0$ transitions can proceed, then $E0$ strength will be generated. Therefore, a $K = 2$ component in the 2_1^+ state, or a $K = 0$ component in the 2_2^+ state, or both, could result in a finite $E0$ strength in the $2_2^+ \rightarrow 2_1^+$ transition. Moreover, K-mixing is expected for states belonging to the ground-state and the so-called γ bands of triaxial systems as the Ge isotopes under investigation. Therefore, a competition of K-mixing and configuration mixing could arise in these nuclei.

In this thesis, a ultra-high-statistics β-decay study of the ^{72,74,76,78}Ge isotopes is presented, which aims at providing experimental information on the $E0$ strengths in $2_2^+ \rightarrow 2_1^+$ and $0_2^+ \rightarrow 0_1^+$ transitions that are lacking in literature, as previously shown in Fig. 1.6. This work is focused in particular on $2_2^+ \rightarrow 2_1^+$ transitions. The $0_2^+ \rightarrow 0_1^+$ transitions of ^{74,76,78}Ge were indeed not experimentally observed. Upper limits on their intensity and, thus, on their strengths have been placed, where possible.

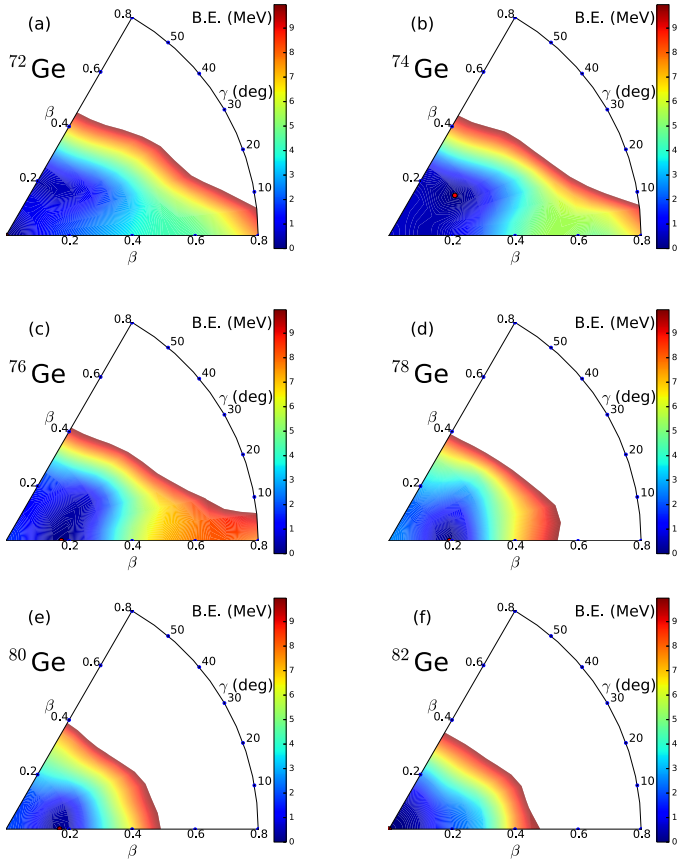

Figure 1.9: Potential energy surfaces for Ge isotopes calculated by Nikšić *et al.* within a self-consistent relativistic Hartree–Bogoliubov model, with the universal relativistic functional DD-PC1 and a finite-range pairing force. Reprinted figure with permission from Ref. [54]. Copyright (2014) by the American Physical Society.

2

EXPERIMENTAL SETUP

The experiments were performed at the Isotope Separator and Accelerator (ISAC) facility at TRIUMF (Vancouver, Canada) in 2017 and 2019. The germanium isotopes (^{72,74,76,78}Ge) under investigation were populated via the β decay of gallium isotopes, produced with the isotope separation on-line (ISOL) technique and delivered to the measurement station as radioactive-ion beams. The spectroscopic studies presented in this work were performed with the GRIFFIN spectrometer, comprised of high-purity germanium clover detectors for γ-ray spectroscopy and of ancillary detectors for internal conversion electron spectroscopy, β-particle tagging and lifetime analysis through fast-timing techniques.

In this chapter the TRIUMF-ISAC facility and GRIFFIN will be described, as well as the experimental details.

2.1 Radioactive Beam Production at TRIUMF

In the Isotope Separator and Accelerator (ISAC) facility at TRIUMF, radioactive-ion beam (RIB) production is obtained through the isotope separation on-line (ISOL) technique [55], by using the proton beam delivered by the TRIUMF 520 MeV H^- cyclotron [56]. A map of the ISAC low-energy experimental hall is shown in Fig. 2.1.

According to the ISOL method, the beam of protons impinges on a thick target, where nuclear reactions (such as proton-induced spallation, fragmentation or fission) occur. A variety of target materials are available at TRIUMF, among which SiC, TiC, Nb, Ta, ThO_2 and UCx. Depending on which target material is used, different nuclear species can be produced. The products are stopped in the bulk of the target material, diffuse to the surface of the target material grains and then effuse to an ion source, where ionization takes place so that an ion beam can be extracted. The target is held at high temperature (up to 2300°C) to favour the diffusion and effusion processes, thus speeding up the release of the short-lived radioactive species of interest [58]. ISAC targets operate with surface ionization, resonant laser ionization or plasma ion sources. The simplest

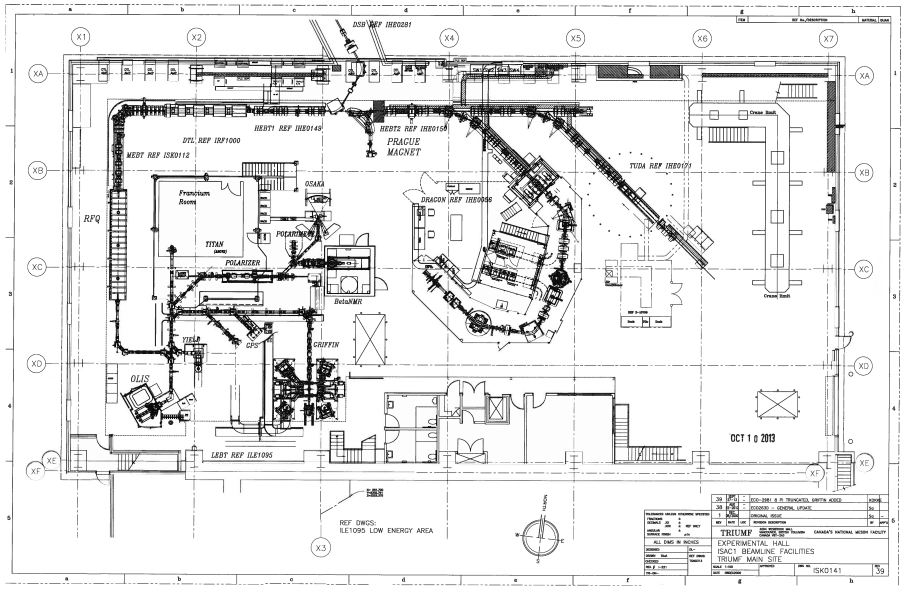

Figure 2.1: Map of the low-energy experimental area of the TRIUMF-ISAC facility [57].

ISOL ion source is a hot cavity surface ion source, which can be used to extract elements with ionization potential less than 6 eV. In this case, the atom from the target enters a transfer tube where surface ionization takes place. The surface ion source is operated at high temperature, similar to the target, and held at a high voltage, up to 60 kV. Ions are extracted by means of a ground electrode which is fixed next to the transfer tube. In a resonant ionization laser ion source, ionization is accomplished through laser beams directed inside the transfer tube (e.g. a standard surface ion source). Multiple lasers are used simultaneously, with the laser frequencies tuned to match atomic transitions of the element of interest. This resonance excites atoms of the element of interest into an ionized state in order that they are extracted as a beam. In the case of the plasma source, a plasma of fast electrons is the means to ionize the atoms. The ion beams extracted from the ion source with energies up to 60 keV are then separated with a mass separator, passing through two dipole magnets in series. A mass resolution $M/\Delta M = 2000$ is routinely achieved at ISAC [59]. After mass separation, the beam is either transported to the low-energy experimental area with a system of electrostatic bending and focusing elements, or accelerated to achieve higher RIB energies.

2.2 Overview of the GRIFFIN Spectrometer

Gamma-Ray Infrastructure For Fundamental Investigations of Nuclei, GRIFFIN, is a high-efficiency γ-ray spectrometer for use in decay spectroscopy studies with the low-energy radioactive beams produced by the TRIUMF-ISAC facility [6]. The spectrometer is composed of up to sixteen Compton-suppressed high-purity germanium (HPGe)

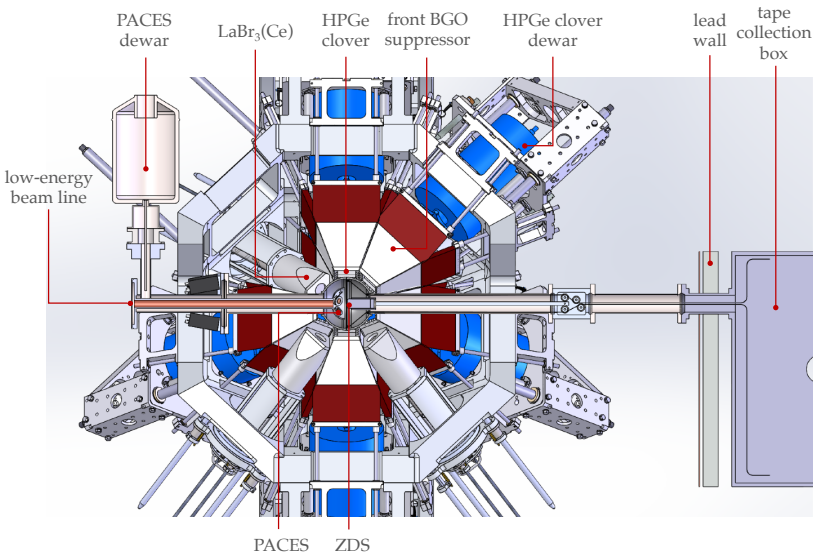

Figure 2.2: Solidworks rendering of the GRIFFIN spectrometer (courtesy of Shaun Georges, TRIUMF). Only one hemisphere of the array is shown. The beam is delivered from the left. In the upstream (left) half of the chamber the PACES array is installed, while the Zero Degree Scintillator (ZDS) is placed in the downstream (right) half of it. The HPGe clovers are set in the 'Optimized peak-to-total' mode, with their faces at 14.5 cm distance from the implantation point on the tape. In this mode, the front BGO Compton suppressors are placed at 11 cm from the implantation point and the $LaBr_3$(Ce) detectors are at 13.5 cm from it. The $LaBr_3$(Ce) detectors are also coupled with BGO shields. On the right side of the figure, the tape box and the lead wall shielding are shown.

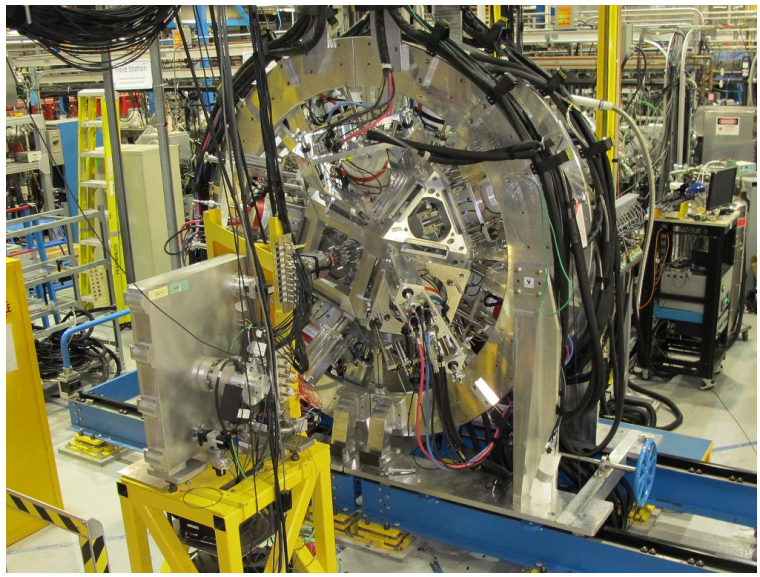

Figure 2.3: Photograph of the GRIFFIN array (view from downstream). The tape collection box can be seen in the foreground.

clover detectors, as well as a suite of ancillary detectors. One of the possible configurations of the spectrometer is presented in the technical drawing in Fig. 2.2. A detailed explanation of the various components shown is provided in the following sections. The specific spectrometer configuration used in the experiments discussed in this work will be illustrated in Section 2.5. Figure 2.3 shows a photograph of the whole spectrometer.

2.2.1 The Moving Tape Collector

The low-energy radioactive-ion beam delivered to GRIFFIN is implanted into a Mylar tape inside a vacuum chamber at the mutual centre of the spectrometer detectors. The 12.7 mm wide tape is a continuous loop of roughly 135 m length which is mounted within a moving tape collector. The tape system is entirely inside the vacuum system of the GRIFFIN chamber and of the low-energy beam transport lines.

The purpose of the moving tape system is to remove long-lived activity from the chamber, thus optimizing the ratio between the radioactive decays of interest for the experiment and contaminant decays, either from beam contaminants or daughter isotopes. The tape can be operated in a series of cycles during data collection. During a cycle the tape is first moved to remove previously implanted activity and then background data are collected; implantation of the radioactive beam in the chamber follows and finally decay data are collected while the beam is blocked. When the tape is moved, the implantation point is transported to a collection box located downstream. A wall of 5 cm thick lead bricks in front of the collection box shields the detectors from exposure to any residual activity collected there.

2.2.2 The GRIFFIN Clover Detectors

The GRIFFIN array is composed of up to sixteen HPGe clovers, each consisting of four n-type HPGe crystals with diameter of 60 mm (before shaping) and length of 90 mm, which are tapered towards the front face [60]. The four crystals of each clover are contained in the same cryostat and are operated at a temperature of $\sim$95 K, achieved with a liquid nitrogen cooling system. Each clover is equipped with a liquid nitrogen dewar which is filled every 8 hours. The operating voltages of the HPGe crystals are between 3.5 and 4 kV. The clover detectors, as well as the ancillary detectors, are inserted in a rhombicuboctahedral supporting structure. Up to sixteen of the eighteen square faces of the rhombicuboctahedron are covered by HPGe detectors. The two remaining square faces are used for the beam delivery system and the in-vacuum moving tape collector system, as can be seen in Fig. 2.2.

The HPGe array is supplied with suppression shields made of the high-efficiency bismuth germanate (BGO) scintillator material. The purpose of the shields is to detect Compton-scattered γ rays which scatter out of the HPGe crystal, as well as to shield the crystal from background radiation originating from outside of the spectrometer. Signals from the suppression shields are used as a veto to discard the Compton-scattered events produced in the HPGe detectors, enhancing the overall sensitivity of the spectrometer. The suppressors are made of three components; a front plate, a side shield and a back catcher.

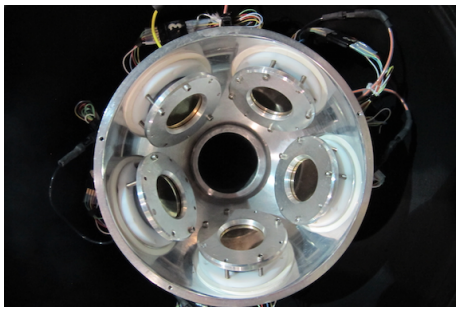

Figure 2.4: Si(Li) crystals of PACES array placed in the upstream hemisphere of the vacuum chamber (view from downstream).

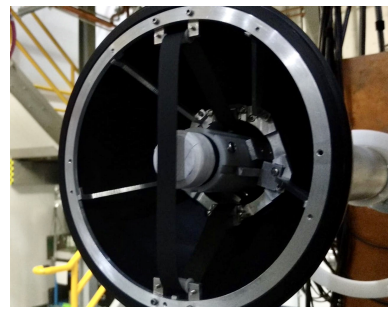

Figure 2.5: Zero Degree Scintillator detector mounted in the downstream hemisphere of the vacuum chamber. The detector is placed behind the tape where the beam is implanted.

The HPGe array and the surrounding BGO shields can be operated in two different modes: the 'High-efficiency' mode and the 'Optimized peak-to-total' mode. In the 'High-efficiency' mode, the HPGe clovers are close-packed around the target location with their faces at 11 cm from the implantation point on the tape and the front suppressors are retracted, as in Fig. 2.2. In the 'Optimized peak-to-total' mode, the faces of the HPGe clovers are withdrawn to 14.5 cm and the front suppressors are inserted at 11 cm to form a complete suppression shield around each HPGe detector.

2.2.3 The PACES Array

One of the ancillary detectors that can complement the HPGe array is the Pentagonal Array of Conversion Electron Spectrometers (PACES). It is an array of five lithium-drifted silicon [Si(Li)] detectors used for conversion electron spectroscopy. Figure 2.4 shows a photograph of the silicon array. The five crystals have a cylindrical shape of 16 mm diameter and 5 mm thickness and are coated with a thin layer of gold. PACES is placed inside the vacuum chamber, in the upstream hemisphere. The five crystals are arranged at $\sim$72° intervals around the beam axis. Each crystal is at a distance of 31.5 mm from the implantation point on the tape and is tilted 24° relative to the implantation point. A bias voltage of -500 V is applied to each crystal. The crystals are cooled down to a temperature of $\sim$148 K during experiments. Their cooling is achieved through a cold finger which connects the array to an external dewar of liquid nitrogen. To accomodate the PACES dewar, one of the sixteen HPGe clovers must be removed. Thus, when using PACES, only 15 clovers are operated. The position of the dewar with respect to the spectrometer can be observed in Fig. 2.2, which shows the dewar on the left side of the image.

2.2.4 Zero Degree Scintillator

A scintillator detector can be mounted in the downstream hemisphere of the vacuum chamber at zero degree with respect to the beam axis. It allows β tagging of the ob-

served events in GRIFFIN and PACES, as well as fast-timing lifetime measurements. The detector is referred to as Zero Degree Scintillator (ZDS). It is a disk made of BC422Q plastic of 25 mm diameter and 1 mm thickness. It can be placed at a few millimeters distance behind the implantation point on the tape. In the experiments discussed in this thesis, its angle coverage was ≈25% of 4π, yielding a detection efficiency of ≈25%. Figure 2.5 shows a picture of the ZDS detector mounted behind the tape in the downstream hemisphere of the chamber.

2.2.5 Lanthanum Bromide Detectors

A set of 8 cerium-doped lanthanum bromide scintillators [$LaBr_3$(Ce)] can be installed in the 8 triangular faces of the rhombicuboctahedral structure of GRIFFIN, as can be seen in Fig. 2.2. These detectors are used to perform lifetime measurements of excited nuclear states through fast-timing techniques. The crystals have cylindrical shape, with diameter and length of 5.1 cm, and are cerium-doped at a level of 5%. They are provided by the manufacturer in a hermetically-sealed aluminium case, together with their photomultiplier tube (model number R2083). They are coupled with BGO suppressors of annular shape (20 mm thick and 110 mm long), to surround the $LaBr_3$(Ce) case. Similarly to the HPGe clovers, the $LaBr_3$(Ce) detectors are placed at a different distance depending on which experimental mode is used. They are installed at 12.5 cm from the implantation point in the 'High-efficiency' mode, while in the 'Optimized peak-to-total' mode they are withdrawn to 13.5 cm to accomodate the BGO suppression shields. The $LaBr_3$(Ce) detectors have not been used for the analysis described in the following chapters of this thesis.

2.3 Data Acquisition

The data acquisition (DAQ) system of GRIFFIN is comprised of custom-designed digital electronics modules [61]. These modules were developed and built with the purpose of handling high-rate data collection, with each HPGe crystal counting at a rate of up to 50 kHz. They treat the signals both of the GRIFFIN HPGe detectors and of the ancillary detectors, although the signal of the $LaBr_3$(Ce) detectors used for fast-timing analysis purposes is processed first with analogue electronics, as described in the following.

The DAQ consists of three levels of electronics modules. The lower level is constituted from GRIF-16 analogue-to-digital converters, with sampling rate of 100 MHz, that digitize the detector signals. At the mid level are the GRIF-C Secondary collector modules, which collect the signals from the GRIF-16s. Finally, the top level consists of a GRIF-C Primary collector module, which filters the data from all the lower levels modules, in order to accept or reject the signals to read out. A reference clock signal is provided to all the DAQ modules by a GRIF-Clk Primary clock module through a set of GRIF-Clk Secondary clock modules.

Regarding the $LaBr_3$(Ce) detectors, the PMT provides an anode and a dynode output signal. The dynode signal, which is used for an energy measurement, goes through a preamplifier and then is directly digitized via a GRIF-16 module. On the other side, the

anode signal, which is used for a timing measurement, is treated with analogue electronics, before being digitized through GRIF-16s [6]. In particular, a Constant Fraction Discriminator (CFD) module, fan-in/fan-out logic modules and a Time-to-Amplitude Converter (TAC) module are used. Analogue electronics is preferred to a completely digital treatment to read out the $LaBr_3$(Ce) timing signals, because it has a faster response than digital electronics. Thus, it provides the best timing resolution in order to perform a fast-timing analysis [62].

The writing to disk stage is achieved through the Maximum Integrated Data Acquisition System (MIDAS) frontend [63], developed at the Paul Scherrer Institute (Switzerland) and TRIUMF. As per the rest of the elements of the GRIFFIN DAQ system, MIDAS is capable of writing data to disk storage at high data rate. Data are written to disk according to the GRIFFIN event format, under the general MIDAS file format [64].

In terms of performance of the DAQ system, note that operating the system at high data rate affects the resolving power of the array. In particular, the energy resolution of the HPGe clovers at 1 MeV of energy degrades from around 2 keV at a count rate of 1 kHz per crystal to >4 keV above 50 kHz [61]. The count rate for the beam times discussed in this thesis can be found in Section 2.5. This degradation in resolution is due to the occurrance of pile-up events at high count rate, which affect the energy evaluation of each recorded hit. The pile-up events can be discarded during the offline analysis and this procedure allows to partially recover the low-rate HPGe resolution. All the data analysis described in the following has been performed discarding the pile-up events.

2.4 Detector Calibrations and Performances

Before the data analysis could be performed, the data had to be calibrated and the efficiency of the detectors had to be studied. In this section, a description of the calibration procedure will be provided, as well as addback procedure, cross-talk corrections and summing corrections, needed for the GRIFFIN data. The detection efficiency of the different elements of the spectrometer will also be presented.

2.4.1 GRIFFIN Energy Calibration

Data from GRIFFIN crystals are summed together during the analysis to increase the statistics and take full advantage of the high-efficiency of the HPGe clover array. A proper gain matching of the energy registered by the crystals of the GRIFFIN array is therefore crucial to be able to maintain the excellent resolution capabilities of HPGe detectors when summing spectra together. Source data have been used to calibrate the energy spectra for the crystals of the 15 clovers used in this work (the sixteenth clover has been removed to accommodate PACES dewar, as discussed in Section 2.2.3). Pile-up rejection was applied to the source data, as well as to both datasets.

The experiments performed in 2017 and 2019 used two different hardware revisions of the GRIF-16 digitizers: Rev. 1 and Rev. 2, respectively. Rev. 2 significantly improved the performance of the digitizers, eliminating a gain drift over time present in data acquired with rev 1 GRIF-16 modules. The two datasets have been thus calibrated in a

different way; an explanation of these procedures is given in the following paragraphs.

October 2017 Beam Time. The HPGe crystal energy spectra of this dataset have been calibrated with a quadratic energy calibration. During this beam time, the Rev. 1 of the GRIF-16 digitizers has been used. Data collected with those digitizer modules presented a noticeable gain drift over time (actually dependent on the temperature in the electronics shack which oscillated as the AC unit switched on and off with a period of roughly 5 minutes). In order to correct the drift, a run-by-run calibration was performed, using as a reference six transitions of ^{72}Ge with energies well known in literature. This procedure guaranteed to exploit the high resolution of the GRIFFIN array, giving an energy resolution of 2.5 keV at 1 MeV when summing 80 hours of acquired data (see Section 2.5.1 for further details on the acquisition time). Despite these corrections, a number of HPGe crystals (number 10, 28, 57 and 59) presented a poorer resolution ($\approx$5 keV at 1 MeV), thus, they were excluded from the analysis.

September 2019 Beam Time. For the experiment performed in September 2019, the Rev. 2 of the GRIF-16 digitizers was used. This solved the gain drift present in the 2017 experiment; therefore, a unique calibration for all the dataset runs could be used. Initially, a quadratic calibration has been performed using the sources of ^{152}Eu and ^{56}Co (with energies in the range 121 keV-1.4 MeV and 1.7-3.2 MeV, respectively). This procedure, though, was not working satisfactorily. At energies higher than 1.5 MeV a significant mismatch in gain for different GRIFFIN crystals was observed, as can be seen in Fig. 2.6. The channels 61 and 63 are missing from the plot, since they showed a poor resolution; thus, they were excluded from the analysis. To tackle the non-homogenous linear response of the ADC over the whole enery range of interest, the energy calibration has been split in two different energy ranges, below and above 1.6 MeV. For all energies lower than 1.6 MeV ^{152}Eu source lines have been used, while for higher energies lines from a ^{56}Co source have been used in combination with lines observed from the neutron capture reaction ^{27}Al(n,γ)^{28}Al. An overlap region of $\pm$100 keV has been identified around the cut-off point at 1.6 MeV, where a randomized procedure assigned one calibration or the other, to assure a smooth passage between the two calibration ranges. Such procedure improved noticeably the gain matching as shown in Fig. 2.7. The crystal 44 showed stronger non-linearities than the other channels, which could not be easily corrected with a two-energy-range calibration. Therefore, it was excluded from the analysis and it is not shown in the plot.

2.4.2 GRIFFIN Addback and Cross-Talk Corrections

The composite nature of the clover detectors allows to apply an addback procedure to the data, which increases the peak-to-total ratio and the full-energy peak efficiency of the array [66]. This procedure sums the energy deposited in two different crystals of the same clover if the two crystals were hit within a fixed time window. In this work, the time window was set to 300 ns length (see Section 3.2). This process aims to reconstruct the full energy of a γ ray that deposited its energy in more than one crystal, because of

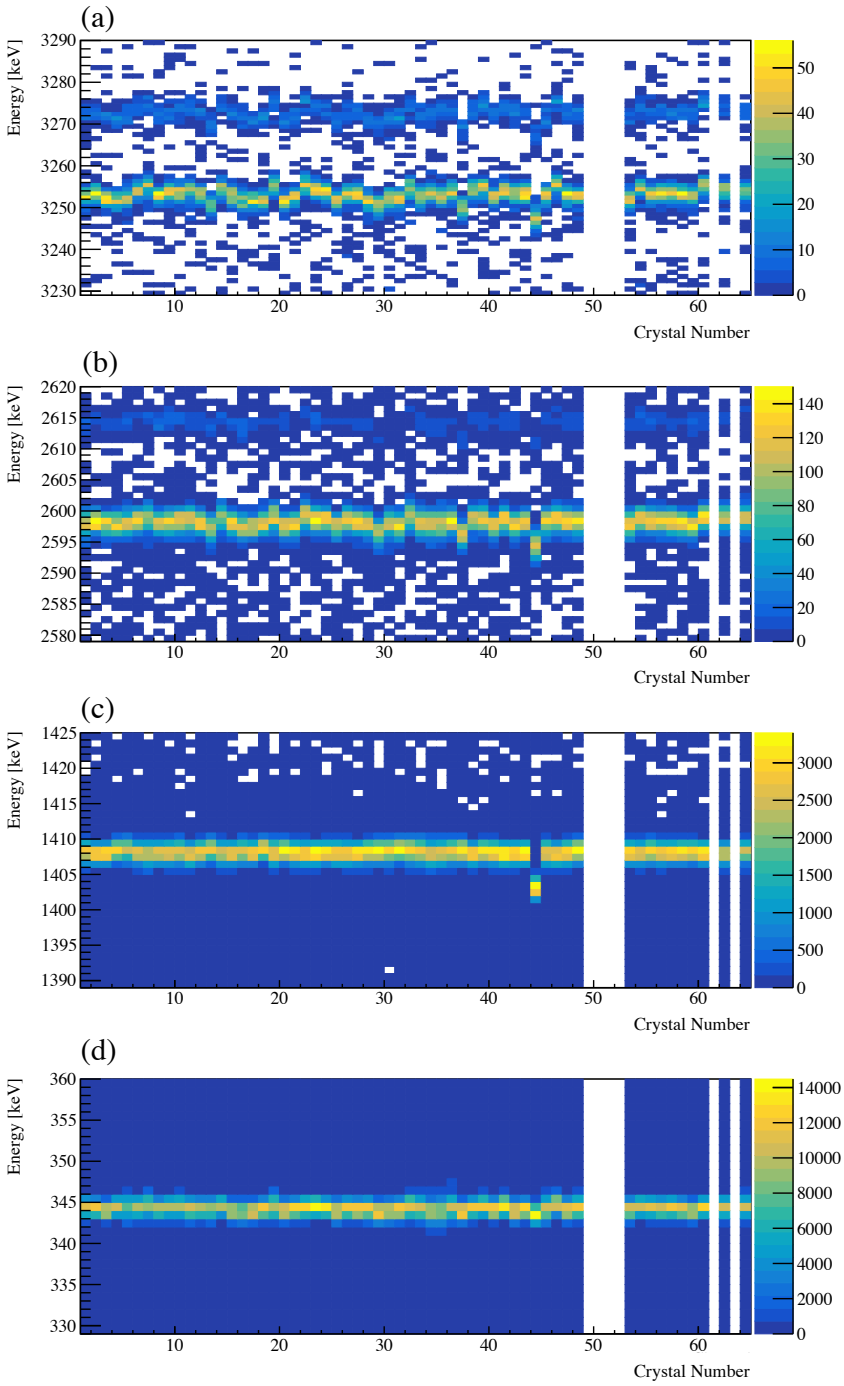

Figure 2.6: GRIFFIN crystal energy versus GRIFFIN crystal number using the same quadratic calibration on the whole energy range. Panels (a) and (b) show ^{56}Co data, while panels (c) and (d) show ^{152}Eu data. Crystals 49 to 53 are missing since they correspond to the clover not installed in this experiment. Crystals 61 and 63 are not present due to their poor resolution.

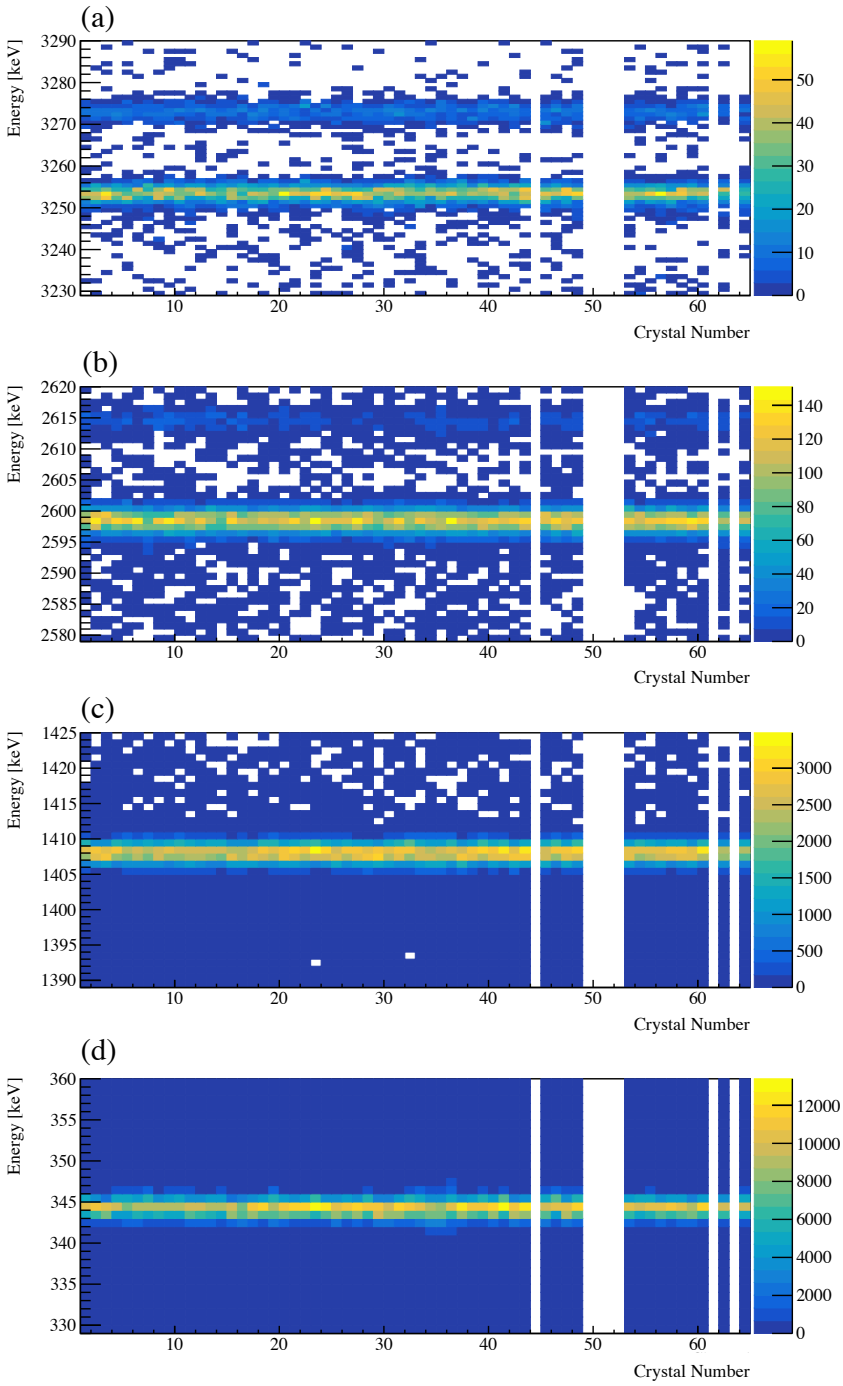

Figure 2.7: GRIFFIN crystal energy versus GRIFFIN crystal number using two different quadratic calibration below and above 1.6 MeV. Panels (a) and (b) show ^{56}Co data, while panels (c) and (d) show ^{152}Eu data. Crystal 44 is missing due to its strong non-linearities, which prevented to obtain a proper gain matching with the other channels.

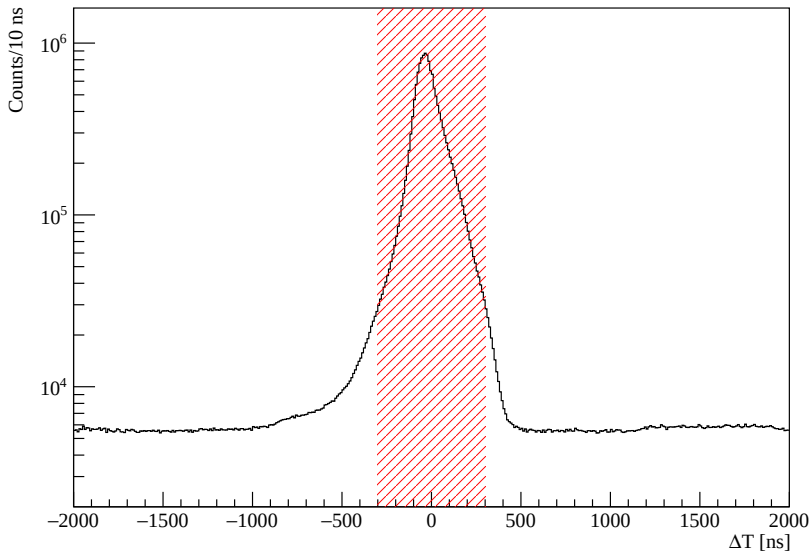

Figure 2.8: Time difference spectrum for γ-γ hits recorded in the same event by GRIFFIN crystals and BGO shields, respectively, with a ^{152}Eu source. The time difference ΔT is calculated as $T_{\text{GRIFFIN}} - T_{\text{BGO}}$. The red area indicates the time window used to perform the suppression.

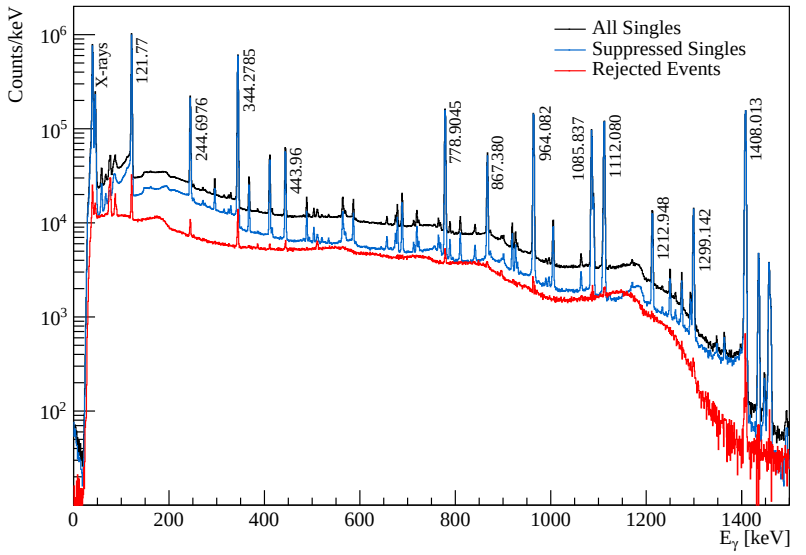

Figure 2.9: Comparison of a ^{152}Eu source GRIFFIN spectrum in all singles (black), in suppressed singles (blue) and of events rejected by Compton suppression (red). Data were acquired during the experiment in September 2019. Energy values of the most intense peaks are indicated on the plot in keV units [65].

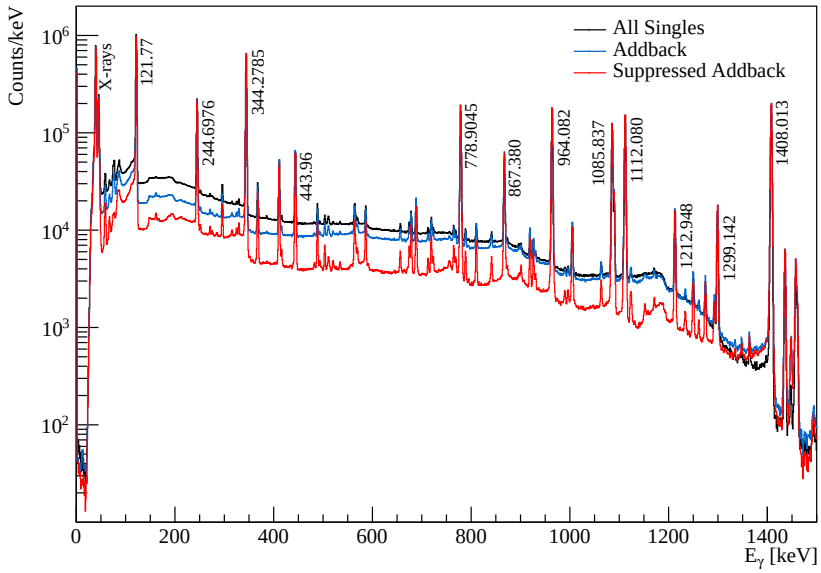

Figure 2.10: Comparison of a ^{152}Eu source GRIFFIN spectrum in singles (black), in addback mode (blue) and in addback mode with Compton suppression (red). Data were acquired during the experiment in September 2019. Energy values of the most intense peaks are indicated on the plot in keV units [65].

Compton scattering or pair production. In this work, both adjacent and diagonal crystal pairs were used for addback purposes, which is the standard procedure in GRIFFIN data analyses.

The 2019 array was operated with BGO shields. Data could thus be Compton suppressed, further increasing the peak-to-total ratio. Figure 2.8 shows a time difference spectrum between GRIFFIN and BGO shields hits. A time window of 300 ns was set to perform the Compton suppression. Any BGO crystal surrounding the clover has been used as veto to suppress signals from any of the four HPGe crystals. The spectrum in Fig. 2.9 shows the result of suppression in the case of ^{152}Eu source data, together with the spectrum of counts rejected by the suppression algorithm. To highlight the results of combining addback and Compton suppression, a comparison between singles, addback and suppressed-addback data is shown in Fig. 2.10.

Electronic coupling between the channels of a HPGe clover detector, known as cross-talk, results in a shift in the measured γ-ray energy of a crystal when another one is hit in coincidence with it. Thus, when applying addback – that considers specifically coincidence events mainly due to Compton scattering of the same γ ray – it is necessary to account for cross-talk among the two crystals fired, to prevent inaccuracy in centroid determination and degradation in energy resolution. Otherwise, when summing the measured energies $E'_{i,j}$ of two crystals fired in coincidence, one will find $E'_i + E'_j \neq E_\gamma$, with E_γ full deposited energy from the Compton-scattered γ ray. This discrepancy for

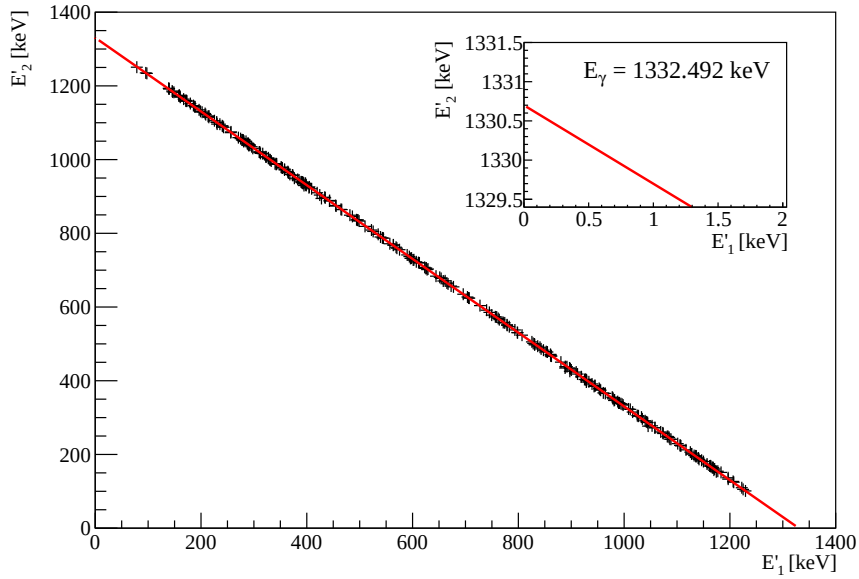

Figure 2.11: Fit of coincident events due to the Compton scattering of a 1332.492 keV γ-ray from a ^{60}Co source in two crystals within the same clover. The inset shows a zoom in the region of the fit where one of the crystals registers a null energy ($E_1' = 0$ keV) and the other one is supposed to register the full energy of 1332.492 keV. As described in the text, cross-talk among crystals results in a shift of such recorded γ-ray energy, therefore a correction of this effect is needed.

the GRIFFIN clovers is ≈0.1%. The magnitude of the cross-talk correction for a given crystal is independent of the energy deposited in that crystal itself and is linearly proportional to the energy deposited in the other crystals of that clover [6]. It is then possible to write:

$$E_1' = E_1 + \alpha_{12} E_2 \tag{2.1}$$

$$E_2' = E_2 + \alpha_{21} E_1 \tag{2.2}$$

where E_i is the real γ-ray energy deposited in the crystal and E_i' is the measured one. The coefficients α_{ij} must be determined experimentally. In order to do so, coincidence data of a ^{60}Co source were used. The coincidence events used were required to satisfy this condition:

$$1322\,\text{keV} < E_1' + E_2' < 1342\,\text{keV} \tag{2.3}$$

Figure 2.11 shows an example of data points satisfying such condition for one crystal pair. Considering the case $E_1 + E_2 = E_\gamma$ of full-energy deposition inside the clover

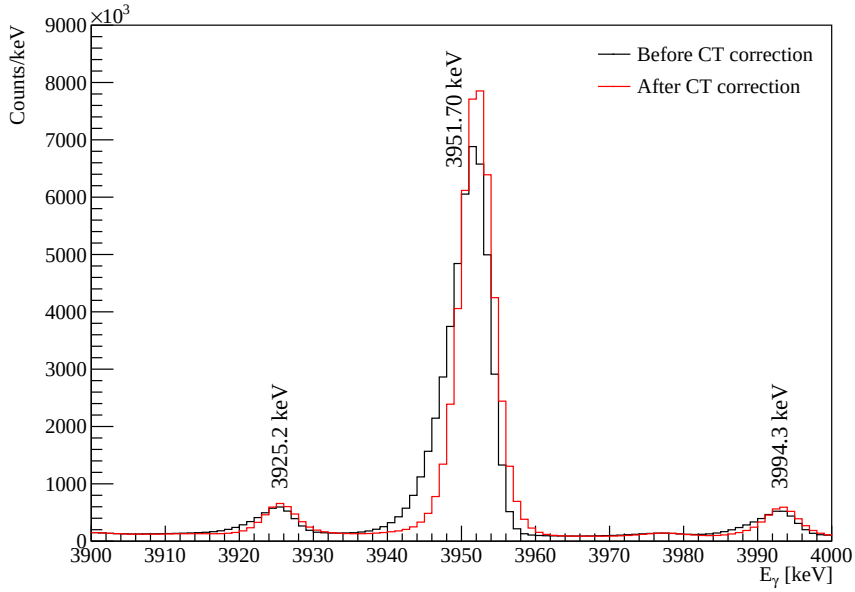

Figure 2.12: GRIFFIN energy spectrum of ^{76}Ge (populated via the β-decay of ^{76}Ga) in addback mode, before and after crosstalk corrections (black and red, respectively). The full width at half maximum is equal to 7.1 keV before the crosstalk correction, and it is reduced down to 5.3 keV after applying the correction. The spectra shown here are not Compton suppressed. All the peaks correspond to γ-ray transitions previously observed in ^{76}Ga β-decay experiments [40]. The data were acquired during the September 2019 beam time.

detector, the Eqs. (2.1) and (2.2) give:

$$E_2' = E_\gamma \frac{1-\alpha_{12}\alpha_{21}}{1-\alpha_{12}} - E_1' \frac{1-\alpha_{21}}{1-\alpha_{12}} \tag{2.4}$$

The full energy value E_γ used here is 1332.492 keV. With this function, it is possible to fit the data points to determine the α_{ij} coefficients. The fit of the data is also shown in Fig. 2.11. The cross-talk effect can be easily observed when zooming into the plot region where the energy deposition happens only into one crystal, and the other one register a null energy signal: the full-energy value is shifted from the reference one E_γ, as shown in the plot inset. Correcting the addback energies with this procedure improves significantly the energy resolution of the addback data, as can be seen in Fig. 2.12, where a reduction of the 25% of the width of the peaks at $\sim$4 MeV is observed. A further quadratic calibration had to be performed on cross-talk corrected data to guarantee the proper centroid placement of source lines in the γ-ray spectrum.

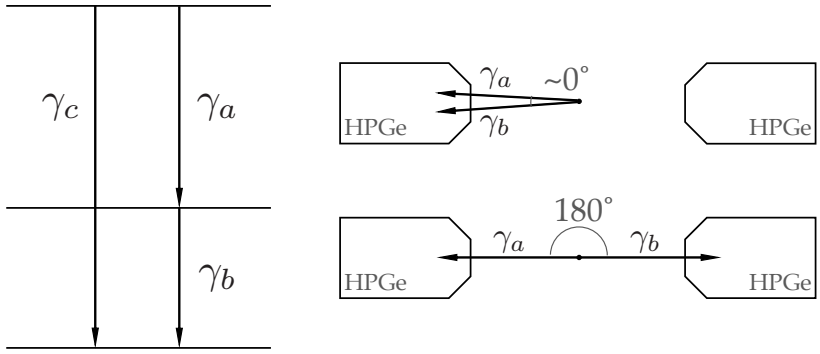

Figure 2.13: On the left side, example of a γ-ray cascade where coincidence summing can play a significant role in a γ-ray spectroscopy analysis. On the right side, sketch of two γ rays detected by the same HPGe crystal (coincidence summing) or by a HPGe crystal pair at 180°. Due to the symmetry of $\gamma\gamma$ angular correlations around 90°, the summing events within the same crystal are the same as the number of coincidence counts in 180° crystal pairs.

2.4.3 GRIFFIN Summing Corrections

Given the large volume of the GRIFFIN HPGe crystals and, hence, the large angle subtended by their faces, it is possible that γ rays emitted in the same decay cascade interact with the same HPGe crystal. This effect is referred to as coincidence summing and must be taken into account when analysing GRIFFIN data, since it affects the γ-ray intensity measurements [6]. It is important to note that true-coincidence summing is a purely geometric effect and is independent of the counting rate, in contrast to random-coincidence summing which is rate dependent. Consider the simple level scheme shown on the left side of Fig. 2.13 and the case when the photons γ_a and γ_b interact with the same crystal, as sketched on the right side of the figure. If both of them deposit all of their energy, there will be an increase of counts in the γ-ray spectrum peak at the energy of γ_c, thus incorrectly increasing the measured efficiency of detecting γ_c. This effect is called *summing in*. Then, suppose that γ_a deposits all its energy in a crystal and that γ_b deposits a fraction or the totality of its energy within the same crystal. In this case, a decrease in the measured detection efficiency for γ_a will be observed. Here, one talks of *summing out*. The probability of summing out is usually larger than that of summing in.

It is possible to apply an empirical correction method to establish the correct intensity of the γ rays of interest. Since the angular correlation of two γ rays emitted in a cascade is symmetrical around 90°, the summing events in a certain crystal (γ rays emitted at 0°) are as many as the coincidence interactions of the same two γ rays in a 180° crystal pair (see sketch in Fig. 2.13). Studying the coincidence matrix of events detected in the 180° crystal pairs can, therefore, give a measure of the summing effect. In particular, to correct summing in, it is necessary to count the γ_a-γ_b coincidence events present in the 180° coincidence matrix, gating on one γ ray and measuring the area of the full-energy

peak of the other one. This number of counts needs to be subtracted from the number of counts of γ_c measured in singles. To correct summing out, one measures the area of γ_a in the total projection of the $180°$ coincidence matrix. This estimates how many γ_a events are in coincidence with Compton scattered events and full-energy detections; this number of counts needs to be added to the singles full-energy peak area of γ_a. In both cases, the number of counts obtained with the $180°$ coincidence matrix must be normalized dividing it by a factor F that takes into account that not all the crystals have a partner at 180°, when not all the 64 crystals of GRIFFIN are in use. This factor F is given by the ratio of the number N_{180} of crystal pairs at $180°$ and the total number N of crystals used in the analysis. When this correction is performed on addback data, clover pairs at $180°$ are considered to build the $180°$ coincidence matrix, instead of crystal pairs.

This correction method has been applied to both the calibration data, to obtain the efficiency curve (discussed in the next section), and the in-beam data (see Table 2.2 in Section 2.4.6).

2.4.4 GRIFFIN Detection Efficiency

The detection efficiency of GRIFFIN was studied using activity-calibrated sources. Given a source γ-ray spectrum, the absolute efficiency of a γ-ray spectrometer can be calculated as

$$\epsilon_\gamma = \frac{A_\gamma}{I_\gamma D(t) \Delta t} \tag{2.5}$$

where A_γ is the area of the peak at the considered energy, I_γ the intensity of the transition, $D(t)$ denotes the decays per second (activity) of the source at the time t of the measurement and Δt the measurement duration. Table 2.1 lists the sources used for this purpose and summarizes their activity at the date of data collection. To obtain the efficiency curve $\epsilon_\gamma(E)$ for GRIFFIN, the data points so obtained were fitted with the

Table 2.1: Activity of the sources used to determine the GRIFFIN efficiency curve. The Table is separated for the two datasets and reports both the NIST-certified activity and the activity at the date of measurement.

	Source	NIST-certified Activity	Date of Certification	Activity at Time of Measurement	Date of Measurement
Oct. 2017	^{152}Eu	39.41 kBq	1/05/2016	36.59 kBq	11/10/2017
	^{56}Co	144 kBq	29/06/2016	2.14 kBq	11/10/2017
	^{133}Ba	38.78 kBq	1/06/2007	19.62 kBq	11/10/2017
Sept. 2019	^{152}Eu	39.41 kBq	1/05/2016	33.12 kBq	20/09/2019
	^{60}Co	35.35 kBq	15/09/2008	8.31 kBq	20/09/2019
	^{56}Co	185 kBq	9/03/2018	1.21 kBq	20/09/2019
	^{133}Ba	38.78 kBq	1/06/2007	17.27 kBq	20/09/2019

function [67]:

$$\epsilon_\gamma(E) = H \cdot \exp\left\{\left[\left(A + B\ln\left(\frac{E}{100}\right) + C\ln\left(\frac{E}{100}\right)^2\right)^{-G} + \left(D + E\ln\left(\frac{E}{1000}\right) + F\ln\left(\frac{E}{1000}\right)^2\right)^{-G}\right]^{-1/G}\right\} \tag{2.6}$$

where E is the γ-ray energy (in keV). The parameter B has been set to 0 in this work.

Figure 2.14 shows the efficiency curve resulting from the fit in singles and addback mode for both the 2017 and 2019 datasets. In the 2017 experiment, the absolute efficiency of GRIFFIN at 1 MeV was 9.7% in singles and 13.4% in addback mode, while in the 2019 experiment, it was 6.3% in singles and 8.5% in addback mode. Such variation in efficiency in the two experiments is due to the different configuration of the detectors, which will be explained in detail in Section 2.5.

2.4.5 PACES Energy Calibration

In order to calibrate the energy spectrum of the crystals of the electron spectrometer PACES, an open ^{207}Bi source was used. The three most intense K-shell electron peaks in the ^{207}Bi spectrum, at 481.7, 975.7, 1682.2 keV respectively, were used to perform a linear calibration. The nominal energy of the electrons was used to calibrate the PACES energy spectra, despite the electrons detected by PACES lose 0.5 keV of their energy, due to the -500 V voltage applied to the PACES crystals. This results in a 0.5 keV discrepancy between the electron- and γ-ray-peak energy in the PACES spectra.

Despite the energy gain matching of PACES spectra, the spectra of different crystals have been treated separately during the analysis, to better account for the different resolution of each detector when fitting electron peaks.

2.4.6 PACES Detection Efficiency

The efficiency of PACES was characterized both for the detection of conversion electrons and for that of photons. The following paragraphs describe the results of this characterization.

Conversion Electron Efficiency

The conversion electron detection efficiency of PACES has been measured taking advantage of the well-known γ-ray efficiency ϵ_γ of GRIFFIN and of the internal conversion coefficients α obtained through the BrIcc conversion coefficient calculator [68]. Remembering the definition of internal conversion coefficient α in Eq. (1.24), it follows that the internal conversion coefficient can be measured experimentally as:

$$\alpha_{\text{exp}} = \frac{A_{\text{ce}}/\epsilon_{\text{ce}}}{A_\gamma/\epsilon_\gamma} \tag{2.7}$$

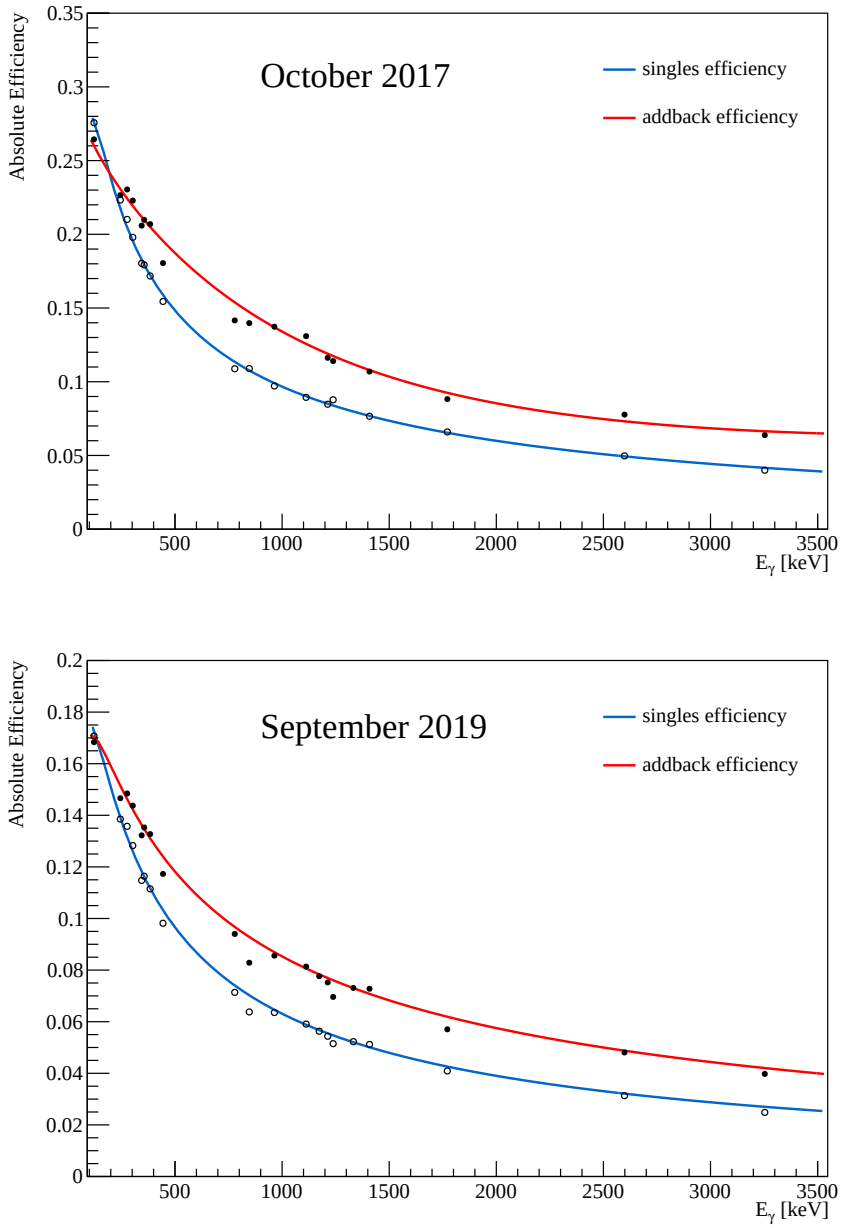

Figure 2.14: Efficiency of GRIFFIN obtained with ^{152}Eu, ^{56}Co and ^{133}Ba sources for October 2017 data (top panel) and with ^{152}Eu, ^{60}Co, ^{56}Co and ^{133}Ba sources for September 2019 data (bottom panel). Summing corrections have been applied to the data points. Error bars are not visible, since they are smaller than the marker size.

where A_{ce} and A_γ are the areas of the conversion electron and γ-ray peaks of interest and ϵ_{ce} and ϵ_γ are the efficiency of PACES for conversion electrons and of GRIFFIN for γ rays. If the conversion coefficient can be calculated through BrIcc, as in the case of a pure $E2$ transition (where no competing $E0$-decay branch is allowed, and there is no experimental uncertainty for a $E2/M1$ mixing ratio), the equation can be inverted to determine the value of the conversion electron efficiency ϵ_{ce} at a given energy E:

$$\epsilon_{ce}(E) = \frac{1}{\alpha_{\text{BrIcc}}} \frac{A_{ce}}{A_\gamma/\epsilon_\gamma} \tag{2.8}$$

In-beam data were used to measure the electron detection efficiency of PACES. The efficiency of PACES can vary during the experiment due to a number of factors, including the beam implantation location and size, the crystal counting rate, as well as the specifics of the decay scheme. Hence, to obtain the most accurate efficiency for each Ge isotope at the energy of the $2_2^+ \rightarrow 2_1^+$ transition, the pure $E2$ $2_1^+ \rightarrow 0_1^+$ transition of that isotope was used. Indeed, in the energy region of the $2_2^+ \rightarrow 2_1^+$ and $2_1^+ \rightarrow 0_1^+$ transitions the behaviour of PACES efficiency is expected to be constant, according to GEANT4 simulations [6]. The area A_{ce} of the K-shell conversion peak of the $2_1^+ \rightarrow 0_1^+$ transition was measured for determining the efficiency $\epsilon_{ce}(E)$.

For the 2017 dataset, only the crystals 2 and 5 of PACES were used in the analysis, due to a poor behaviour of the other crystals in terms of energy resolution and peak shape in the energy spectrum. Figure 2.15 shows as an example the fit of the $2_1^+ \rightarrow 0_1^+$ transition peak in the singles spectrum of the PACES 2 crystal used for this measurement. The fit region has been cut close to the photo-peak on the high-energy side to avoid including the Compton edge of the $3_1^- \rightarrow 2_2^+$ 1051-keV transition in ^{72}Ge, which lies at ≈845 keV. The area A_γ of the corresponding γ-ray peak in the GRIFFIN spectrum was corrected for the summing out effect (note that no summing in occurs in this case, since there are no parallel cascades to the $2_1^+ \rightarrow 0_1^+$ transition). Table 2.2 shows the contribution of summing out to the photo-peak area measured in the GRIFFIN spectrum. The final efficiency values $\epsilon_{ce}(E)$ are reported in Table 2.3.

To confirm the robustness of this measurement, PACES-GRIFFIN coincidence data were also considered. A GRIFFIN-gate on the $3_1^- \rightarrow 2_2^+$ 1051-keV transition in ^{72}Ge allowed to remove the contribution of the Compton background for this transition to the PACES spectrum. The PACES-GRIFFIN coincidence matrix was sorted to include events from both PACES 2 and 5, so in this case the total PACES efficiency was extracted. The obtained value of 0.008(3) from coincidence data is consistent with the sum of 0.0085(2) of the efficiency values measured separately for PACES 2 and 5 with singles data and reported in Table 2.3, thus validating the result.

For the 2019 dataset, PACES crystals 2 and 4 were used in the analysis, since the other ones showed an inconsistent behaviour throughout the experiment, including a degradation of the energy resolution over time and a lack of stability of the detection efficiency for data acquired with the same beam. Data in singles were used to determine the area of the $2_1^+ \rightarrow 0_1^+$ K-shell peak in the cases of ^{72,74,78}Ge. Figures 2.16, 2.17 and 2.20 show examples of the fits performed with the spectra of PACES 2 for these isotopes. In the case of mass 76, it was not possible to use data in singles to confidently fit the K-shell

Table 2.2: Contribution of summing out to the photo-peak area A_γ measured in GRIFFIN spectrum for the $2_1^+ \rightarrow 0_1^+$ transitions used to measure the conversion electron efficiency of PACES. The number of counts in the 180° matrix is already corrected for the F factor proper of each dataset (equal to $48/56$ for 2017 data and to $50/57$ for 2019 data). Note that for the 2017 data the source-to-detector distance was 110 mm, whereas for the 2019 data it was 145 mm.

	Mass	Energy (keV)	Area $\times 10^8$	180° counts $\times 10^6$	Sum out %
Oct. 2017	72	834.01(2)	12.59(5)	20.49(14)	1.395(12)
Sept. 2019	72	834.01(2)	1.957(11)	1.36(2)	0.695(9)
	74	595.847(6)	21.9(2)	25.69(9)	1.174(9)
	76	562.93(3)	15.46(4)	18.47(10)	1.195(7)
	78	619.40(16)	30.3(2)	44.2(2)	1.456(11)

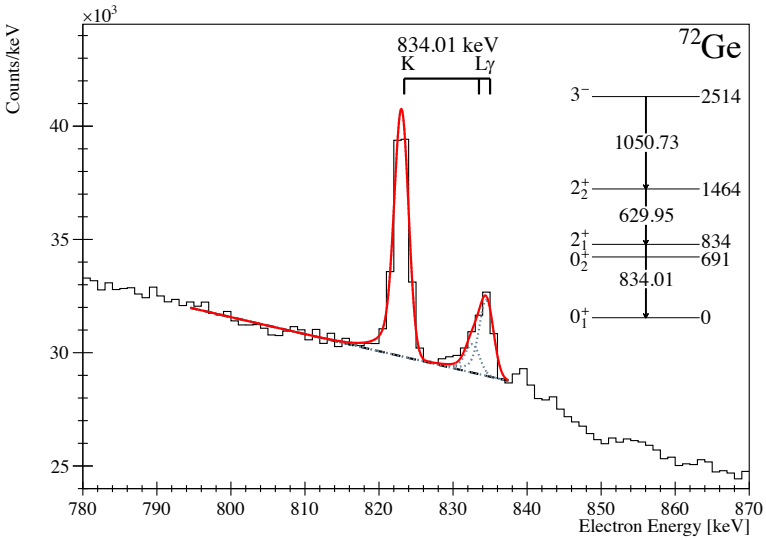

Figure 2.15: Spectrum in singles of PACES 2 for ^{72}Ge data in the 2017 dataset. A fit of the 834-keV, $2_1^+ \rightarrow 0_1^+$ transition of ^{72}Ge is shown. The fit includes the K-, L-shell and photo-peak of this transition and is on purpose cut after the photo-peak, to exclude from the fitting region the Compton edge of the 1051-keV, $3_1^- \rightarrow 2_2^+$ γ-ray transition of ^{72}Ge at ≈845 keV. A partial level scheme of ^{72}Ge shows the relevant transitions.

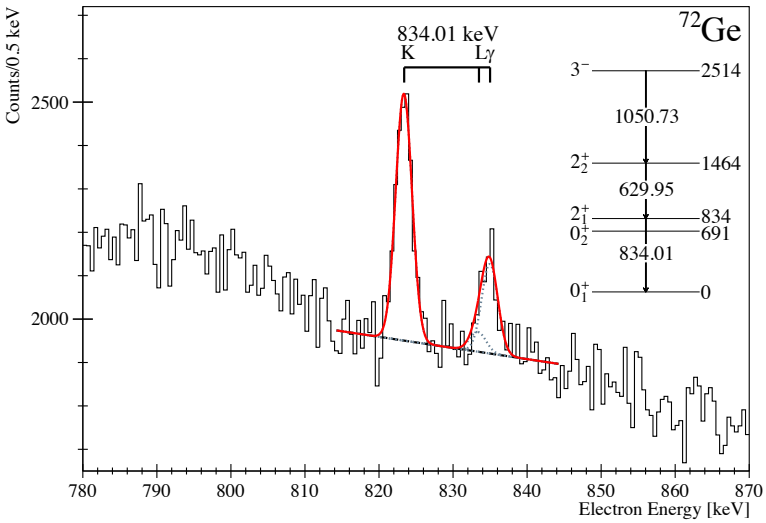

Figure 2.16: Spectrum in singles of PACES 2 for ^{72}Ge data in the 2019 dataset. A fit of the 834-keV, $2_1^+ \rightarrow 0_1^+$ transition of ^{72}Ge is shown. The fit includes the K-, L-shell and photo-peak of this transition. A partial level scheme of ^{72}Ge is also shown in the figure.

Table 2.3: Conversion electron efficiency ϵ_i of the i-th PACES crystal for each of the β-decay experiments discussed in this thesis. The energies of the $2_1^+ \rightarrow 0_1^+$ transitions of $^{72-78}$Ge used for the measurements are indicated. The values ϵ_i^β obtained with β-tagged measurements are also reported, where available.

	Mass	Energy (keV)	ϵ_2	ϵ_5		
Oct. 2017	72	834.01(2)	0.0049(2)	0.003 59(11)		
	Mass	Energy (keV)	ϵ_2	ϵ_4	ϵ_2^β	ϵ_4^β
Sept. 2019	72	834.01(2)	0.0030(2)	0.0060(3)	0.0031(3)	0.0061(5)
	74	595.847(6)	0.005 67(15)	0.007 09(15)	0.005 54(13)	0.006 59(14)
	76	562.93(3)	0.0073(14)	0.0064(3)	–	–
	78	619.40(16)	0.004 77(14)	0.006 70(14)	0.004 85(12)	0.0069(2)

of the $2_1^+ \rightarrow 0_1^+$ 563-keV transition, because this overlaps with the L-shell and photo-peak of the $2_2^+ \rightarrow 2_1^+$ 546-keV transition (see Fig. 2.18). Thus, γ-coincidence data were used for this purpose, in order to isolate the $2_1^+ \rightarrow 0_1^+$ K-shell peak by setting a gate on a transition that populates directly the 2_1^+ state (see Fig. 2.19). The two transitions of 847 keV ($4_1^+ \rightarrow 2_1^+$) and 546 keV ($2_2^+ \rightarrow 2_1^+$) were used as a gate on PACES 2 and PACES 4 crystals, respectively. It was not possible to use the 546-keV transition as a gate for the PACES 2 spectrum, despite this likely providing a higher statistics, because in this case the fit was too sensitive to the choice of fitting region due to the irregular shape of the background. This choice yields a higher uncertainty on the PACES 2 efficiency for ^{76}Ge relative to the one of PACES 4, due to the higher statistical uncertainty of the electron spectrum in γ-coincidence with the low-intensity 847-keV transition. Similarly to what was done for the 2017 dataset, summing out corrections were applied to the GRIFFIN data; Table 2.2 shows the magnitude of this correction mass by mass. Table 2.3 summarizes the values of the electron detection efficiency $\epsilon_{\text{ce}}(E)$ for each PACES crystal considered in this work. The table includes also the efficiency measurements obtained with β-tagged data of ^{72,74,78}Ge. This measurement was performed as a consistency check. These results were in agreement with the ones obtained through data in singles, but since β-tagged data didn't provide great advantage on the background shape, they were not used further in the analysis to preserve the statistics.

As a further check on the conversion electron efficiency values obtained for the 2019 dataset, the efficiency was measured with another method. Consider again Eq. (2.8), but this time let A_γ and ϵ_γ be the area and the efficiency for photo-peaks detected in the PACES detector, instead of GRIFFIN. The photo-efficiency of the PACES crystals at 569.7 keV was measured with a ^{207}Bi source (see the following paragraph for details). Let $R_{\gamma/\text{K}}$ be the ratio of counts of a photo-peak and K-shell peak for a given transition:

$$R_{\gamma/\text{K}} = \frac{A_\gamma}{A_{\text{ce}}} \tag{2.9}$$

This ratio has been measured for the $2_1^+ \rightarrow 0_1^+$ transition of the considered Ge isotope

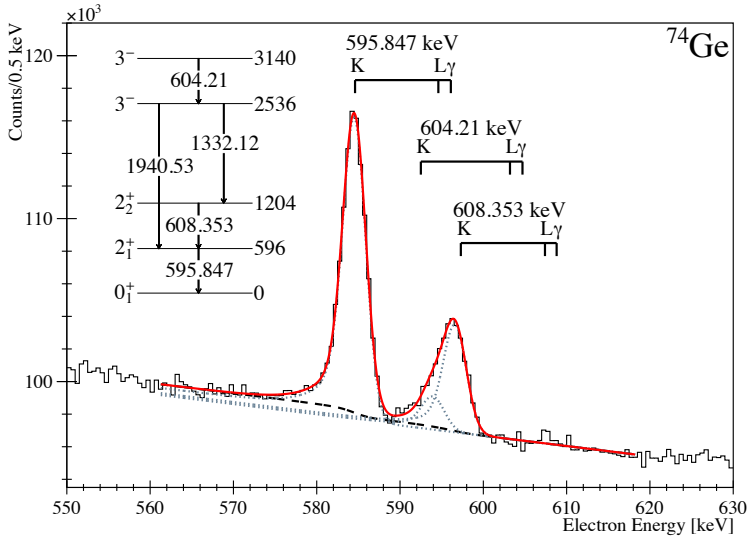

Figure 2.17: Spectrum in singles of PACES 2 for ^{74}Ge data in the 2019 dataset. A fit of the 596-keV, $2_1^+ \rightarrow 0_1^+$, 604-keV, $3^- \rightarrow 3^-$ and 608-keV, $2_2^+ \rightarrow 2_1^+$ transitions of ^{74}Ge is shown. Three peaks have been fitted: the K-shell peak of the 596-keV transition, a peak that comprises the L-shell and photo-peak of the 596-keV transition and the K-shell peak of the 604-keV one, and the K-shell of the 608-keV transition. The 604-keV, $3^- \rightarrow 3^-$ transition is expected to provide a negligible contribution to the second peak, since its γ-ray intensity in β-decay is 3.1(2)% of the 596-keV one [41]. Nevertheless, only the area of the first peak fitted is necessary for the detection efficiency measurement. A partial level scheme of ^{74}Ge shows the relevant transitions.

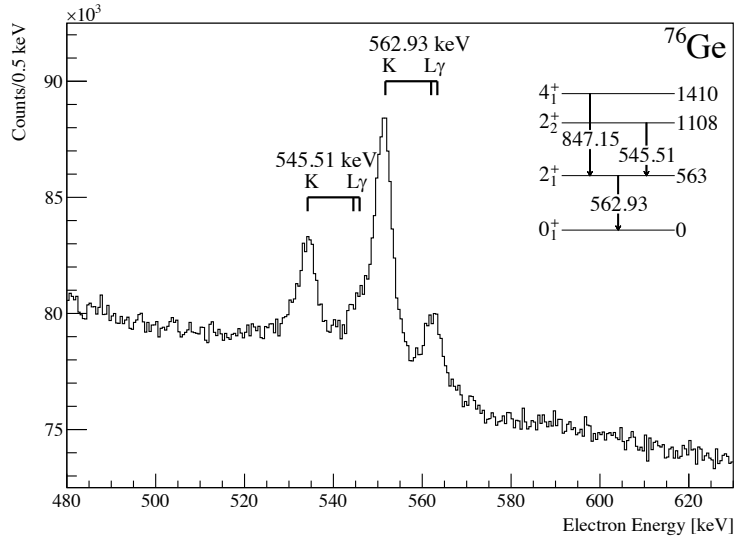

Figure 2.18: Spectrum in singles of PACES 2 for ^{76}Ge data collected in 2019. The K-shell peak of the 563-keV, $2_1^+ \rightarrow 0_1^+$ transition overlaps with the L-shell and photo-peak of the 546-keV, $2_2^+ \rightarrow 2_1^+$ transition. A partial level scheme of ^{76}Ge shows the relevant transitions.

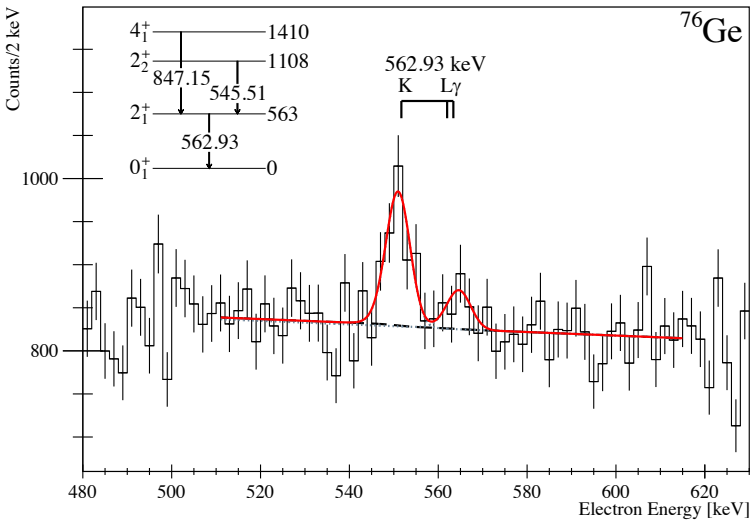

Figure 2.19: Spectrum of PACES 2 for ^{76}Ge data in the 2019 dataset in coincidence with the 847-keV, $4_1^+ \rightarrow 2_1^+$ transition of ^{76}Ge detected in GRIFFIN. A fit of the 563-keV, $2_1^+ \rightarrow 0_1^+$ transition of ^{76}Ge is shown. The fit includes the K-shell peak and the sum of the L-shell and photo-peak of the 563-keV transition. A partial level scheme of ^{76}Ge shows the relevant transitions.

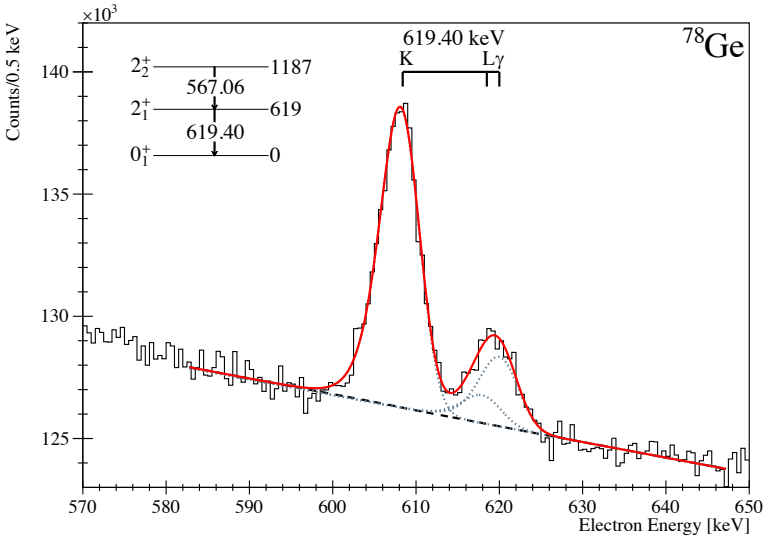

Figure 2.20: Spectrum in singles of PACES 2 for ^{78}Ge data in the 2019 dataset. A fit of the 619-keV, $2_1^+ \rightarrow 0_1^+$ transition of ^{78}Ge is shown. The fit includes the K-shell, L-shell and photo-peak of this transition. A partial level scheme of ^{78}Ge is also shown in the figure.

by fitting two peaks in the PACES spectra: the K-shell peak and a peak that comprises both the L-shell and photon contributions. Using the K-shell peak area and the α_K/α_L value from BrIcc [68], it was possible to calculate the number of expected counts in the L-shell peak (since only pure $E2$ transitions were considered). Subtracting this number of counts from the area of the second fitted peak, the number of photo-peak counts was obtained and the ratio $R_{\gamma/\mathrm{K}}$ calculated for each PACES crystal. From Eq. (2.8) and Eq. (2.9), the conversion electron efficiency ϵ_{ce} at a given energy E can be written as:

$$\begin{aligned}\epsilon_{\mathrm{ce}}(E) &= \frac{A_{\mathrm{ce}}/\alpha_{\mathrm{BrIcc}}}{A_\gamma/\epsilon_\gamma^{\mathrm{PACES}}} = \\ &= \frac{A_{\mathrm{ce}}/\alpha_{\mathrm{BrIcc}}}{R_{\gamma/\mathrm{K}}A_{\mathrm{ce}}/\epsilon_\gamma^{\mathrm{PACES}}} = \\ &= \frac{\epsilon_\gamma^{\mathrm{PACES}}}{\alpha_{\mathrm{BrIcc}}R_{\gamma/\mathrm{K}}}\end{aligned} \tag{2.10}$$

thus providing a measurement of $\epsilon_{\mathrm{ce}}(E)$ where only fits of peaks in the PACES spectra are considered. This measurement method was applied to the ^{74,76,78}Ge data and provided results consistent with the previous measurements using PACES and GRIFFIN. In the case of ^{74}Ge, this measurement was performed with PACES data in coincidence with the the 2353-keV transition detected in GRIFFIN, which populates directly the 2_1^+ state decaying from the (3^-) state at 2949.5 keV, in order to isolate the $2_1^+ \rightarrow 0_1^+$ peak from the $2_2^+ \rightarrow 2_1^+$ and $3^- \rightarrow 3^-$ present in the singles spectrum (see Fig. 2.17). PACES spectra in singles were considered for ^{78}Ge. Regarding ^{76}Ge, as explained before and similarly to the ^{74}Ge case, coincidence data are needed to isolate the $2_1^+ \rightarrow 0_1^+$ transition peak in the spectrum. As already discussed, in the case of PACES 2 this greatly reduces the statistics, leading to a large uncertainty on the $R_{\gamma/\mathrm{K}}$ ratio and thus on the efficiency value measured here. In the case of PACES 4, the background shape on the high energy side of the transition peaks prevented a satisfactory fit of the L-shell and photo-peak, so no measurement was performed for this crystal. The obtained values of $\epsilon_{\mathrm{ce}}(E)$ for ^{74,76,78}Ge are listed in Table 2.4. In the case of ^{72}Ge, this procedure was not applied because of the $\approx$270 keV difference between the photo-peak energy of the $2_1^+ \rightarrow 0_1^+$ transition of ^{72}Ge relative to that of ^{207}Bi. Indeed, the photo-efficiency of PACES cannot be considered constant over such a range of energy.

Table 2.4: Conversion electron efficiency ϵ_i of the i-th PACES crystal for the 2019 dataset measured using Eq. (2.10), where ϵ_γ is the photo-efficiency of PACES and $R_{\gamma/\mathrm{K}}$ is the photo/K-shell ratio for the $2_1^+ \rightarrow 0_1^+$ transition of the considered Ge isotope. The ratio $R_{\gamma/\mathrm{K}}$ was measured with data in singles for mass 78 and in coincidence for mass 74 and 76. The $2_1^+ \rightarrow 0_1^+$ transition energies are also reported.

Mass	Energy (keV)	ϵ_2	ϵ_4
74	595.847(6)	0.006(2)	0.0058(15)
76	562.93(3)	0.006(5)	–
78	619.40(16)	0.007(4)	0.008(2)

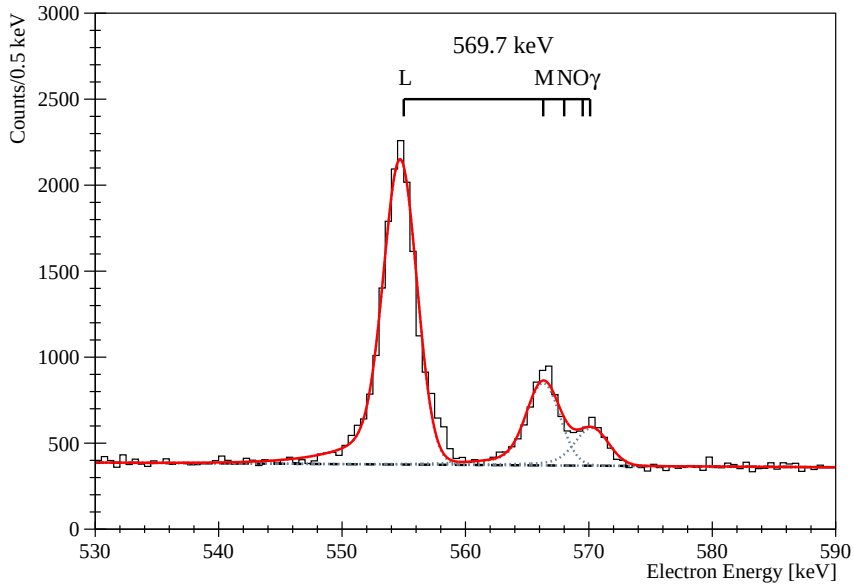

Figure 2.21: PACES 4 electron spectrum for the 569.7 keV transition from a ^{207}Bi source. The L- to O-shell peaks and the photon peak are labelled. The red line shows the total fit, while the dashed black lines indicate the single peak contributions to the total fit function. Data were collected in the 2019 experiment.

Photopeak Efficiency

The conversion electron peaks of interest for this work are close to the γ-ray peaks detected by PACES, because the electron binding energy of Ge is at maximum 11 keV (K-shell electrons). Hence, the electron peaks will be separated from the γ-ray peak by 11 keV, with the L-shell peak at only 1.3 keV of separation. Given the detector finite resolution, this implies that the L-shell peak and the photon peak are not resolved in the PACES spectra. This had to be considered while performing the electron analysis, in order to decouple all the different contributions to the observed peaks. The photo-peak efficiency of the PACES crystals was estimated using data from a ^{207}Bi source, which decays to ^{207}Pb through electron capture. Source data were chosen to perform this measurement, independently from the conversion electron efficiency one, because they offered the cleanest spectrum possible. Moreover, the ^{207}Pb spectrum has a photo-peak at the energy of 569.7 keV, which is conveniently close to the energy range of interest for the analysis described in the following. The activity of this source has been measured to be 24519(982) Bq on the 19$^{\text{th}}$ April 2017 using the GRIFFIN array.

To estimate the photo-peak efficiency of PACES, it was necessary to measure the area of the photon peak of the 569.7 keV transition. In the case of ^{207}Pb, conversion electrons from the K- up to O-shell give a non-negligible contribution to the spectrum. Both the N- and O-shell peaks are very close in energy to the photon peak (0.8 and 0.1 keV, respec-

tively), resulting in a unique peak around 569.7 keV of energy (see spectrum in Fig. 2.21). For this reason, only one peak was fitted that comprised N-, O-shell and photon peak. The L- and M-shell peaks were fitted as well. Such a fit is shown in Fig. 2.21. To recover the photon peak area, the following formula was used:

$$\begin{aligned} A_\gamma &= A_{\mathrm{NO}\gamma} - A_\mathrm{N} - A_\mathrm{O} = \\ &= A_{\mathrm{NO}\gamma} - \frac{\alpha_\mathrm{N}}{\alpha_\mathrm{L}} A_\mathrm{L} - \frac{\alpha_\mathrm{O}}{\alpha_\mathrm{L}} A_\mathrm{L} \end{aligned} \tag{2.11}$$

where A_γ is the area of the photon peak to be recovered, $A_{\mathrm{NO}\gamma}$ is the area of the fitted peak that includes the N-, O-shell and photon contributions, A_i and α_i are the area and the internal conversion coefficient for the i^{th}-shell conversion electron, respectively. The areas of the N- and O-shell peaks were determined from A_L, properly scaled for the conversion coefficient ratios. The efficiency values obtained at 569.7 keV are reported in Table 2.5.

Table 2.5: Photo-efficiency of PACES crystals at 569.7 keV, obtained with a ^{207}Bi source (data collected in September 2019).

PACES crystal	Photo-Efficiency at 569.7 keV
2	$1.7(3) \times 10^{-6}$
4	$2.0(4) \times 10^{-6}$

2.5 Experimental Details of S1716 Beam Time

In this section, the details of the TRIUMF experiments S1716 analysed in this thesis will be described. The experiment was completed in two beam times, that were performed in October 2017 and September 2019, respectively. In both cases, the Ge isotopes were populated through the β^- decay of Ga isotopes. The Ga isotopes were delivered as beams by the TRIUMF-ISAC facility to the GRIFFIN implantation point. In the 2017 experiment, a ^{72}Ga beam was delivered, while in 2019 beams of ^{72,74,76,78}Ga were used. Table 2.6 summarizes the halflives and Q-values of the Ga isotope of interest for this work.

Table 2.6: Halflives, ground state spin and parity I^π_gs and Q-values for β^- decay of the Ga isotopes used in the S1716 experiments to populate the Ge nuclei of interest [40, 41, 42, 43].

Beam	Halflife	I^π_gs	Q-value (keV)
^{72}Ga	14.10(2) h	3^-	3997.5(10)
^{74}Ga	8.12(12) m	(3^-)	5373(4)
^{76}Ga	32.6(6) s	$(2^+, 3^+)$	7010(90)
^{78}Ga	5.09(5) s	(3^+)	8156(4)

Table 2.7: Summary of data collection details for the ^{72}Ga beam delivered in the 2017 experiment and for each of the four Ga beams delivered in the 2019 experiment. The tape cycle phases (column 3) are given in the following order: tape move, background data collection, data collection with beam on, data collection with beam off. When no tape cycle phases are indicated, the beam was either implanted continuously or the previously accumulated Ga nuclei were let decay at the implantation point. Superscripts (a, b, c) label the different tape cycles used with the ^{78}Ga beam.

	Beam	Ion Source	Tape Cycle	Hours of Data Collected	Average Beam Intensity (pps)
Oct. 2017	^{72}Ga	Laser	Implantation	2.5	1.5×10^5
			Decay	202	–
Sept. 2019	^{72}Ga	Laser	Implantation	0.5	4.0×10^4
			Decay	9.5	–
	^{74}Ga	Surface	Implantation	21	2.8×10^5
	^{76}Ga	Surface	1.5 s – 1 s – 12 m – 1 m	34	1.9×10^5
	^{78}Ga	Laser	1.5 s – 0.5 s – 3 s – 5 s^a	10	
			1.5 s – 0.5 s – 6 s – 5 s^b	18.5	1.1×10^6
			1.5 s – 0.5 s – 12 s – 5 s^c	20	

2.5.1 October 2017 Beam Time

The ^{72}Ga ion beam delivered by TRIUMF-ISAC was produced with a proton beam current of 25 μA impinging on a Ta target (23.60 g/cm^2 thick). Ions were extracted from the target with the laser ion source. The beam was implanted on the tape at the center of the GRIFFIN chamber for 2.5 hours, in order to build a hot source. The data acquisition lasted for the following 8.5 days. The intensity of the ^{72}Ga beam was 1.5×10^5 pps and no contaminant ions were identified in the beam. Such information is summarized in Table 2.7.

Immediately after the hot source implantation, the count rate of GRIFFIN was of 25 kHz per crystal, while that of PACES was of 13 kHz per crystal. Only data at a GRIFFIN rate lower than 5 kHz (PACES rate lower than 4 kHz) were used to perform the analysis described in this thesis. In particular, for the electron analysis data collected after 2.6 halflives of the parent Ga were used (80 hours in total). Only this subset of the entire dataset was used, since, as discussed in Section 2.3, the higher rate spectra were affected in terms of energy resolution. This dataset collected very high statistics, thus, the superior energy resolution of the low-rate part was preferable and still provided excellent statistics.

The configuration of detectors for this experiment was as following:

- 15 HPGe clovers without BGO suppressors placed at 11 cm from the implantation point (crystals 10, 28, 57 and 59 have not been used in this analysis, as previously described in Section 2.4.1);
- PACES array, in the upstream half of the chamber (only the crystals 2 and 5 have been used in the analysis, as described in Section 2.4.6);

- ZDS detector, in the downstream half of the chamber;
- 8 $LaBr_3$(Ce) detectors without BGO suppressors placed at 12.5 cm from the implantation point.

During this experiment, the Rev. 1 of the GRIF-16 digitizers was used.

2.5.2 September 2019 Beam Time

The ^{72,74,76,78}Ga beams were produced with a proton beam current of 10 μA and a UCx target (10.42 g/cm^2 thick). For masses 74 and 76 (first half of the experiment), the beam was extracted using surface ionization only because of a technical issue with the laser ion source. For masses 72 and 78 (second half of the experiment), the technical issues were resolved so the laser ionization source was utilized for the production of the Ga beam. The laser ionization source gives higher yields for Ga isotopes. The achieved beam intensity is reported in Table 2.7 for each mass, together with information about data collection, such as tape cycle modes and duration of measurements. For a detailed explanation of how the beam intensity of the Ga ion beams has been calculated, see Appendix A. The beams used were pure, except for in the case of ^{76}Ga which contained a small fraction (0.02%) of ^{76}Rb.

The configuration of the GRIFFIN spectrometer and ancillary detectors was as following (as shown in Fig. 2.2):

- 15 HPGe clovers fully suppressed placed at 14.5 cm from the implantation point (crystals 44, 61 and 63 have not been used in this analysis, as previously described in Section 2.4.1);
- PACES array, in the upstream half of the chamber (only the crystals 2 and 4 have been used in the analysis, as described in Section 2.4.6);
- ZDS detector, in the downstream half of the chamber;
- 8 $LaBr_3$(Ce) detectors supplied with BGO suppressors placed at 13.5 cm from the implantation point.

The Rev. 2 of the GRIF-16 digitizers was used in this experiment. Table 2.8 summarizes the recorded count rates values for each detector type.

Table 2.8: Count rates for each detector type in the 2019 experiment. Each column corresponds to an ion beam delivered during the experiment. Count rates for the ^{72}Ga beam were measured at the start of decay time after implantation; for ^{76,78}Ga, the highest rate reached over the tape cycle is given. The superscripts to the ^{78}Ga beam refer to the three different tape cycles already listed in Table 2.7. Reported rates of GRIFFIN, PACES and $LaBr_3$(Ce) are per crystal.

	^{72}Ga	^{74}Ga	^{76}Ga	^{78}Ga^a	^{78}Ga^b	^{78}Ga^c
GRIFFIN Rate (kHz)	1.2	5	5	10	8	10
ZDS Rate (kHz)	20	100	120	180	150	170
PACES Rate (kHz)	0.9	4	5	8	7	8
$LaBr_3$(Ce) Rate (kHz)	0.9	4	3	7	6	7

3

ANALYSIS TECHNIQUES

This chapter gives an overview of the techniques used to perform the analysis presented in this thesis. The main goal of determining $E0$ strengths was achieved measuring independently different observables (electromagnetic mixing ratios and internal conversion coefficients). Branching ratio measurements of the γ-ray branches depopulating the first excited 0^+ states of ^{74,76,78}Ge have also been performed in this study.

In the following, details about the data sorting are given, followed by a brief description of each technique relevant for such measurements.

3.1 Data Sorting

The data files collected with the GRIFFIN DAQ are written to disk according to the GRIFFIN event file format, under the general MIDAS file format (see Section 2.3). They are subsequently sorted via the analysis package GRSISort [69], which is based on ROOT [70]. GRSISort converts the raw MIDAS files into ROOT files in two different stages. Firstly, it produces a fragment tree, which is a ROOT file containing a collection of time-ordered hits. Secondly, it applies an event-building process, namely it groups together hits whose timestamps are in a given coincidence window, and stores these so-called events into an analysis tree. In this work, a building window of 2 μs was used for this purpose. The analysis trees are then sorted into histograms via GRSISort to perform the intended analysis.

3.2 Coincidence Timing Conditions

For the electron analysis and for the angular correlation analysis, coincidence γ-γ and γ-electron matrices were built. The time coincidence window between prompt events was set on the main peak appearing in the time difference spectra of the different detector types. Figure 3.1 shows the time difference spectrum for GRIFFIN hits, while Fig. 3.2

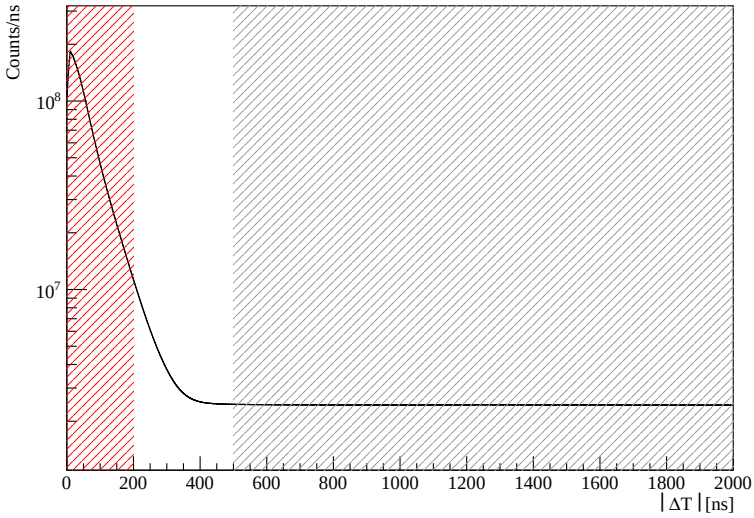

Figure 3.1: Absolute time difference spectrum for γ-γ hits recorded by GRIFFIN in the same event. The red area indicates the time window used to build the γ-γ coincidence matrix. The grey area covers the region of the spectrum used to perform the time random background subtraction. Data were collected in the 2017 experiment.

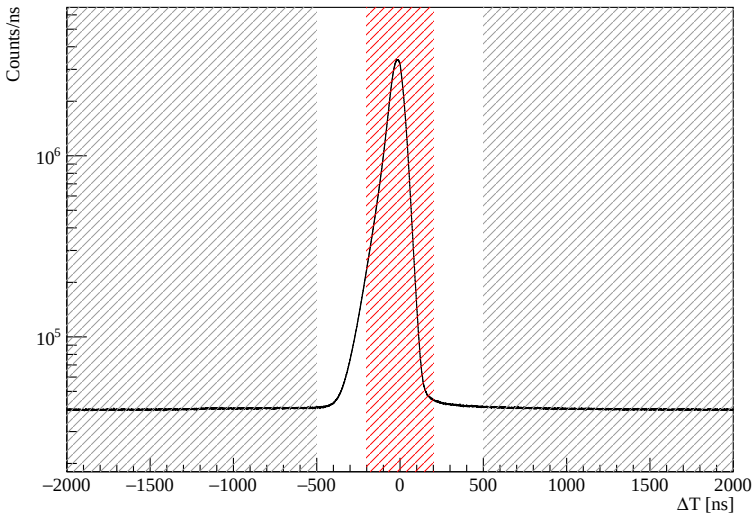

Figure 3.2: Time difference spectrum for γ-electron hits recorded in the same event by GRIFFIN and PACES, respectively. The time difference ΔT is calculated as $T_{\text{ce}} - T_{\gamma}$. The red area indicates the time window used to build the γ-electron coincidence matrix. The grey area covers the region of the spectrum used to perform the time random background subtraction. Data were collected in the 2017 experiment.

shows the time difference spectrum between GRIFFIN and PACES recorded hits. In the latter, the coincidence peak at the center of the spectrum is not symmetric, because of the different time response of the GRIFFIN and PACES detectors. The prompt coincidence windows used in the analysis of the 2017 data set are marked in the figures with red shaded areas. When establishing the time coincidences to fill in a coincidence matrix, a time random subtraction procedure was also performed, to remove the time random component present in the main peak in the time spectrum. The time random window is also shown in Figs. 3.1 and 3.2, with gray shaded areas. In order to apply this subtraction, a time random matrix was built using such window and was subtracted (properly scaled for its width) from the prompt coincidence matrix of interest.

In order to perform the addback procedure on GRIFFIN signals, a time window of 300 ns was used.

3.3 Peak Fitting

A crucial part of this work was reliably establishing the areas of the peaks of interest in the γ-ray and conversion electron spectra. In order to do so, the peaks were fitted through the package jRootTool based on ROOT [71]. This package allows the user to select the most appropriate function to fit peaks, including a Radware-like function (Gaussian with a low-energy tail and a step-like background [72]), a Gaussian function and a superposition of two Gaussians with same centroid. It also allows to fit the background with constant or linear shapes and with or without a step function below each peak, to best describe the low-energy increase of counts due to Compton scattered events.

In the analysis presented here, the γ-ray peaks were fitted with a superposition of two Gaussians, while the electron peaks, that present a more prominent low energy tail (due to partial collection of the charge deposited in the detector), were fitted with the Radware-like function.

3.4 Determining Electromagnetic Mixing Ratios through Angular Correlations

This section summarizes how to determine the mixing ratio δ of a γ-ray transition through the study of an angular correlation. For a definition of the mixing ratio δ, see Eq. (1.18). The sign convention for the mixing ratio adopted in this work is the one introduced by Krane and Steffen [28].

In the first part (Section 3.4.1), an overview of the angular correlation technique is given. Section 3.4.2 describes the details of how the technique is implemented when treating data collected with the GRIFFIN spectrometer.

3.4.1 Angular Correlation of γ rays in cascade

An angular correlation is the study of the emission probability of a certain γ ray as a function of the emission angle θ with respect to the direction of emission of a previously

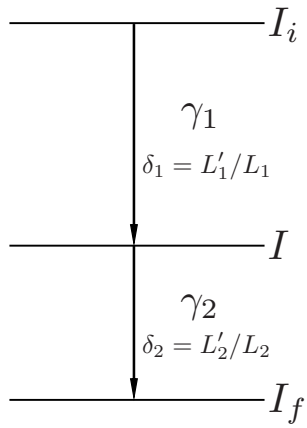

Figure 3.3: Cascade of γ rays that have different multipolarities L_i and $L_i' = L_i + 1$.

emitted γ ray. The angular correlation is described by the function $W(\theta)$:

$$W(\theta) = \sum_{k,\,\text{even}} a_k P_k(\cos\theta) \tag{3.1}$$

where P_k are Legendre polynomials and the coefficients a_k depend on the spins and multipolarities involved in the γ-ray cascade of interest [27]. Consider the cascade shown in Fig. 3.3 with $I_i \xrightarrow{\gamma_1} I \xrightarrow{\gamma_2} I_f$, where the γ rays have multipolarities L and $L' = L + 1$ and mixing ratio δ. For this cascade, the *normalized* coefficients a_k are defined as [27, 28]:

$$a_k = B_k(\gamma_1) A_k(\gamma_2) \tag{3.2}$$

where

$$B_k(\gamma_1) = \frac{F_k(L_1 L_1 I_i I) - 2\delta_1 F_k(L_1 L_1' I_i I) + \delta_1^2 F_k(L_1' L_1' I_i I)}{1 + \delta_1^2} \tag{3.3}$$

$$A_k(\gamma_2) = \frac{F_k(L_2 L_2 I_f I) + 2\delta_2 F_k(L_2 L_2' I_f I) + \delta_2^2 F_k(L_2' L_2' I_f I)}{1 + \delta_2^2} \tag{3.4}$$

The $F_k(LL'I'I)$ coefficients are defined and tabulated in Ref. [27]. Note the different sign appearing in the second term of the definition of $B_k(\gamma_1)$ and $A_k(\gamma_2)$, respectively. Figure 3.4 shows the calculated angular correlation $W(\theta)$ for different combinations of spins, multipolarities and mixing ratios.

The summation over k values in Eq. (3.1) is restricted up to k values that satisfy the following rule [73]:

$$0 \leq k \leq \text{Min}(2I, 2(L_1)_{\text{max}}, 2(L_2)_{\text{max}}) \tag{3.5}$$

where $(L_i)_{\text{max}}$ is the maximum value between L_i and L_i', in the case of transitions with mixed multipolarity. If pure transitions are considered, $(L_i)_{\text{max}}$ corresponds to L_i. For k values not satisfying this rule, the F_k coefficients vanish, and thus the a_k coefficient

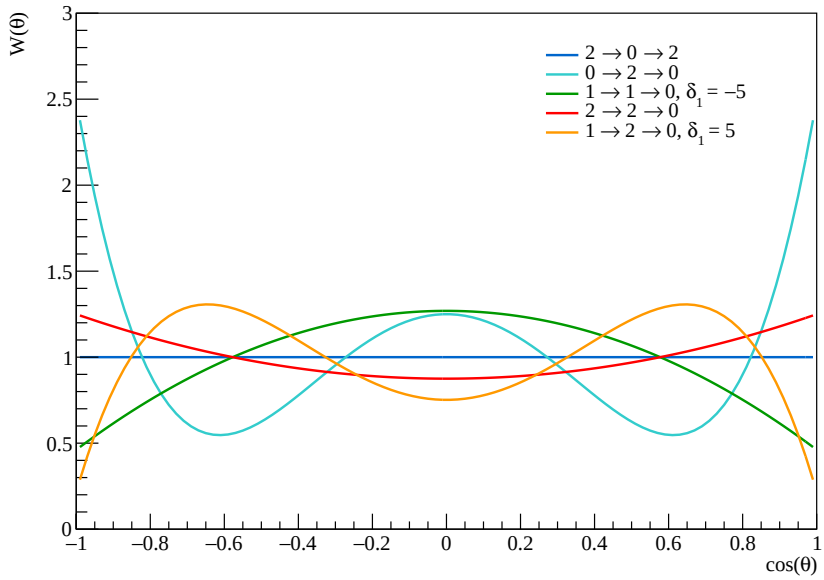

Figure 3.4: Examples of theoretical angular correlations $W(\theta)$ for different cascades $I_i \xrightarrow{\gamma_1} I \xrightarrow{\gamma_2} I_f$. Spins are reported in the legend. In such examples, the mixing ratios δ_1 and δ_2 of the γ rays γ_1 and γ_2 have been assumed as equal to zero, unless otherwise indicated.

as well. One can conclude that in the case of $I = 0$ (or $I = \frac{1}{2}$, if considering odd-mass nuclei) it holds that $k \leq 0$, namely the angular correlation is isotropic. As an example, this can be observed in Fig. 3.4 for the cascade $2 \xrightarrow{\gamma_1} 0 \xrightarrow{\gamma_2} 2$ (dark blue line). If the multipolarities involved are up to quadrupolar, the sum arrests at most at $k = 4$. For the cascades studied in this thesis and discussed in Section 4.1 this condition always applies, hence the relevant terms in the sum are a_2 and a_4 and Eq. (3.1) can be rewritten as:

$$W(\theta) = 1 + a_2 P_2(\cos\theta) + a_4 P_4(\cos\theta) \tag{3.6}$$

The study of an experimental angular correlation can provide a measurement of δ, given the relationship between the coefficients a_k and the mixing ratio δ of the considered γ rays [Eqs. (3.2) to (3.4)]. Constraints on the level spins can also be set by such studies. In this work, experimental angular correlations will be used to measure mixing ratio δ values.

The angular correlation $W(\theta)$ can be measured experimentally using a multi-detector system, so that the intensity of γ-γ coincidences can be measured at different relative emission angles. Due to the finite size of the detectors, the observed correlation will present a weaker anisotropy relative to the theoretical one, namely the experimental a_i coefficients will be attenuated. This attenuation needs to be accounted for during the analysis. In the following, it will be assumed that such an effect is well determined.

Moreover, it will be assumed that corrections have been made for the different detector efficiencies of the considered detector-pairs. Details on the implementation of such corrections will be provided in the next subsection. The experimental curve can thus be written as:

$$W(\theta_i)_{\text{exp}} = a_0[1 + a_2 P_2(\cos\theta_i) + a_4 P_4(\cos\theta_i)] \tag{3.7}$$

where a scaling factor a_0 has been introduced, since the observed angular correlation is *a priori* non-normalized, and where the angles θ have been indexed to remind that the set of available angles in the experimental setup is discrete.

To measure the mixing ratio δ of one of the γ rays (considering the other one to be known, as well as the spins), a non-linear fit of Eq. (3.7) can be performed, where the overall scaling factor a_0 and the mixing ratio δ are free parameters [74]. In order to simplify the non-linear fit procedure, it can be useful to set one of the unknown parameters to a fixed value so to have effectively only one free parameter when running a fitting routine. In this case, this procedure is applied by sampling possible values of the parameter δ. For convenience, samples of $\arctan(\delta)$ are considered, since the $\arctan$ function maps the δ values that range from $-\infty$ to $+\infty$ into the finite interval $(-\pi/2, \pi/2)$. For each $\arctan(\delta)$ sample, the coefficients a_2 and a_4 are calculated through Eq. (3.2) and the experimental curve is fitted only for the scaling factor a_0. In order to determine what is the optimum δ value, the χ^2 of the fit is then plotted as a function of the considered $\arctan(\delta)$ values. The χ^2 curve is approximated and fitted with a parabolic function in the minimum region, to determine the χ^2_{min} value that corresponds to the δ value that best fits the data. This yields the δ measurement. The uncertainty on the mixing ratio is extracted considering the δ values corresponing to $\chi^2_{\text{min}} + 1$ in the parabolic fit. In this work, such a technique has been used to measure mixing ratio δ values.

Angular correlations can be used also to constrain (and at times assign) the level spins. For this purpose, the same procedure as above is applied, making different hypotheses on one spin of the cascade $I_i \xrightarrow{\gamma_1} I \xrightarrow{\gamma_2} I_f$, so that different χ^2 curves are obtained. Such χ^2 distributions have $N-2$ degrees of freedom (ν), where N is the number of experimental data points and 2 is the number of parameters of the non-linear fit, namely δ and a_0. According to the recommendation of Ref. [74], any spin hypothesis that provides a χ^2/ν curve which falls below a 99% confidence limit can be accepted. Note that in the case where the spin hypothesis implies that the considered γ ray has pure multipolarity (e.g., when considering the spin $I = 0$), the mixing ratio δ is not anymore a free parameter of the fit, since it is required to be null. Hence, in this case the number of degrees of freedom ν is modified to $N-1$, with a_0 as the only free parameter. Moreover, also the value of the χ^2 corresponding to the 99% confidence limit will vary accordingly, because a different ν is used.

A different approach to the analysis of an experimental angular correlation consists in doing a linear fit of Eq. (3.7) with parameters a_0, $a_0 \cdot a_2$ and $a_0 \cdot a_4$. After division by a_0, the parameters a_2 and a_4 are obtained. From such a_2 and a_4 values it is then also possible to determine the mixing ratio δ, using the definition of a_2 and a_4 as functions of δ in Eq. (3.2). There are critical aspects, though, in this approach to extract δ values. The first one is the need of taking into account properly the joint probability distribution of

the pair (a_2, a_4), since the two parameters can be correlated. Details on how to properly implement this method are provided in Ref. [74]. The second one is that such a linear fitting does not set any requirements on the a_2 and a_4 solutions. Therefore, the best-fit values could not correspond to any physically meaningful solution for δ. Given these considerations, the values of δ determined in this work have been obtained minimizing the fit of the experimental angular correlations directly by δ, as described in the previous paragraphs. Nonetheless, the linear fit has been also performed and the resulting (a_2, a_4) pairs will be presented in Section 4.1, together with the values of δ.

3.4.2 Angular Correlation Analysis with the GRIFFIN Spectrometer

The implementation of the angular correlation analysis with data collected with the GRIFFIN spectrometer is discussed in the following section. A thorough explanation of the algorithms described here can be found in Ref. [75].

Angular bins at GRIFFIN

A set of 51 angular bins θ_i is available at GRIFFIN, ranging from $15.4°$ to $180°$ in the 14.5 cm source-to-detector distance configuration. In particular, the angular difference between two adjacent HPGe crystals in the same clover detector is $15.4°$, while the angle between diagonal crystals within the same clover is $21.9°$. Hence, experimental angular correlations with up to 51 data points can be produced, providing great sensitivity to mixing ratio δ measurements. In some specific cases it is necessary to exclude some of the smallest angular bins, because they are contaminated with Compton-scattering of a γ ray with equal energy to the sum of the two γ rays in the cascade of interest.

Event-mixing technique

Each angular bin θ_i is associated with a certain number of HPGe crystal pairs that are installed at an angular difference θ relative to the center of the GRIFFIN array. This number can vary from 48 to 128. When measuring the experimental angular correlation $W(\theta_i)$ as the number of $\gamma\gamma$ coincidences $N_i^{\gamma\gamma}$ at each angular bin θ_i, a correction is needed to take into account the different number of crystal pairs for each θ_i. The simplest approach in correcting for this is weighting the values $N_i^{\gamma\gamma}$ by the number of crystal pairs associated with the i^{th} bin. This, though, does not account for differences in the efficiency of the HPGe crystals. In order to correct for this too, the so called *event-mixing technique* has been introduced in Ref. [75]. According to this technique, a set of matrices is produced using uncorrelated γ rays, one for each angular bin θ_i, analogously to the set of coincidence matrices built to determine $N_i^{\gamma\gamma}$. To guarantee the uncorrelation of the γ-ray hits, a time difference larger than 2 μs is required, namely pairs of γ-ray hits recorded in different physical events are used. The number N_i^{em} of false coincidences at a given angular bin θ_i obtained from the event-mixed matrices is used to weight the number $N_i^{\gamma\gamma}$ of true coincidences. The experimental data points are thus obtained as:

$$W(\theta_i) = \frac{N_i^{\gamma\gamma}}{F N_i^{\text{em}}} \tag{3.8}$$

An F factor has been introduced here to normalize the experimental curve to unity. It is defined as:

$$F = \frac{\sum_i N_i^{\gamma\gamma}}{\sum_i N_i^{\mathrm{em}}} \tag{3.9}$$

where the sums are extended to all the considered angular bins θ_i. In order to avoid the weight N_i^{em} from increasing the overall uncertainty on the points $W(\theta_i)$, a very long time window (in this work, from 2 μs to 200 μs) is used to build the event-mixed matrices. This allows to maximise the number N_i^{em}, hence significantly reducing its statistical uncertainty and the impact of the correction on the overall error on $W(\theta_i)$.

Accounting for finite size detector effects through GEANT4 simulations

The finite size detector effects that attenuate the observed angular correlation relative to the calculated one need to be properly corrected for in the analysis. In order to quantify their impact, GEANT4 simulations have been run to reproduce the geometry of the setup and the experimental angular correlation of each considered γ-ray cascade, following the procedure introduced in Ref. [75], where the simulations for the 11 cm source-to-detector distance GRIFFIN configuration are described in detail. The simulations used in this work for the 14.5 cm source-to-detector distance setup have been performed by C. Natzke and are presently unpublished [76]. In the following paragraph, a description is given of how extracting the relevant information by comparing the experimental curves $W(\theta_i)$ with the simulations.

Determining the mixing ratio δ from an experimental angular correlation

In this work, the algorithm defined as *Method 2* in Ref. [75] has been used to extract the mixing ratio δ values from the data. According to this method, a GEANT4 simulation of the following distributions has been produced:

$$Z_0(\theta) = 1 \tag{3.10}$$
$$Z_2(\theta) = 1 + P_2(\cos\theta) \tag{3.11}$$
$$Z_4(\theta) = 1 + P_4(\cos\theta) \tag{3.12}$$

namely three angular correlations of the form Z_0, Z_2 and Z_4 have been simulated for a γ-ray cascade of set energy. Recalling the expression of Eq. (3.7), it follows that a linear combination of such distributions can be used to reproduce any angular correlations with coefficients a_2 and a_4:

$$\begin{aligned} Z_{\mathrm{sum}} = {} & xZ_0 + yZ_2 + zZ_4 \quad = \\ = {} & A_{00}[(1 - a_2 - a_4)Z_0 + a_2Z_2 + a_4Z_4] \end{aligned} \tag{3.13}$$

Note that the scaling factor A_{00} introduced here is different from the a_0 appearing in Eq. (3.7). This A_{00} is necessary to scale the Z_i simulated distributions to the data. The experimental curve $W(\theta_i)$, as previously explained, is normalized to unity through the normalization factor F introduced in Eq. (3.8). This linear combination of the simu-

lated Z_i distributions is then used to fit the observed angular correlation $W(\theta_i)$ with a non-linear fit and extract the mixing ratio value, as discussed in Section 3.4.1. The two parameters of the non-linear fit are A_{00} and the mixing ratio δ of one of the two γ rays of the cascade, which appears in the coefficients a_2 and a_4 according to Eq. (3.2). Considerations discussed in the previous sections are applied when determining the best-fit δ value and its 1σ uncertainty.

As previously discussed in Section 3.4.1, the experimental angular correlations were alternatively fitted with a linear fit of Eq. (3.13), which then yielded a_2 and a_4 values. Results of such fits will also be presented in the following chapter.

3.5 Determining Internal Conversion Coefficients

The conversion electron spectra observed with PACES and the γ-ray spectra recorded with GRIFFIN were used to determine the internal conversion coefficient α of the transitions of interest. As previosly mentioned in Eq. (2.7), the experimental value α_{exp} for a certain i^{th}-shell transition can be obtained through the following formula:

$$\alpha_{\text{exp}} = \frac{A_{\text{ce}}/\epsilon_{\text{ce}}}{A_\gamma/\epsilon_\gamma} \tag{3.14}$$

where A_{ce} is the area of the conversion electron peak and A_γ is the area of corresponding γ-ray peak; ϵ_{ce} and ϵ_γ are the efficiency of PACES and of GRIFFIN at the proper transition energy. In this analysis, the K-shell conversion electron peaks were used to determine the α_{exp} value with such formula.

The procedure was applied both to singles and coincidence spectra. When spectra in coincidence were considered, the same γ-ray gate was set both on the γ-electron and γ-γ matrices. The contribution of the efficiency of GRIFFIN at the gating transition energy $\epsilon_\gamma^{\text{gate}}$ does not modify Eq. (3.14), since it appears in both the numerator and denominator:

$$\alpha_{\text{exp}} = \frac{A_{\text{ce}}/\epsilon_{\text{ce}}\epsilon_\gamma^{\text{gate}}}{A_\gamma/\epsilon_\gamma\epsilon_\gamma^{\text{gate}}} = \frac{A_{\text{ce}}/\epsilon_{\text{ce}}}{A_\gamma/\epsilon_\gamma} \tag{3.15}$$

Each PACES detector was analysed and fitted separately, in order to better take into account the different detector responses in term of resolution and peak shape.

3.6 Determining Electric Monopole Transition Strengths

The electric monopole strength for a given $I_i^\pi \rightarrow I_f^\pi$ transition, where $I_i^\pi = I_f^\pi$, can be obtained from the measured observables, such as internal conversion coefficients, mixing ratios and lifetimes. Reminding Eq. (1.28) and the fact that the lifetime τ is defined as the inverse of the transition probability λ, it is possible to write the relation that yields $\rho^2(E0)$ [77]:

$$\rho^2(E0) = \frac{1}{\Omega \times \tau(E0)} \tag{3.16}$$

Here, Ω is an atomic electron factor of the form:

$$\Omega = \Omega_{\mathrm{K}} + \Omega_{\mathrm{L}} + ... + \Omega_{\pi} \tag{3.17}$$

where each term can be calculated for the internal conversion decay process of a certain atomic shell (K, L, and so forth) or for the internal pair formation process (π) [33]. The other term appearing in Eq. (3.16), $\tau(E0)$, is the partial lifetime for $E0$ decay of the state I_i^{π}. This is defined as $\tau(E0) \equiv 1/\lambda(E0)$, with $\lambda(E0)$ decay constant of the $E0$ decay mode, and can be related to the total lifetime τ of the state I_i^{π} by:

$$\tau(E0) = \frac{\sum_j \lambda_j}{\lambda(E0)}\,\tau \tag{3.18}$$

where λ_j is the relative decay constant of the j^{th} decay mode of the state I_i^{π}. In the following, $\lambda(E0)$ will be referred to as $\lambda_{\mathrm{ce}}(E0)$, where the subscript reminds that the $E0$ decay can occur only via the emission of conversion electrons (ce) for the low-energy transitions considered in this work, for which the internal pair formation decay mode is not energetically possible. In the rest of this section, it will be explained how the measured internal conversion coefficients $\alpha_{\mathrm{K,exp}}$ and mixing ratio values δ are used to determine $\lambda_{\mathrm{ce}}(E0)$.

For a mixed $I_i^{\pi} \rightarrow I_f^{\pi}$ transition ($I_i^{\pi} = I_f^{\pi}$, $I > 0$), the experimental conversion coefficient includes not only the $M1$ and $E2$ contributions, but also the $E0$ one, if there is any. It can be written as [78]:

$$\alpha_{\mathrm{exp}} = \frac{\lambda_{\mathrm{ce}}(E0) + \lambda_{\mathrm{ce}}(M1) + \lambda_{\mathrm{ce}}(E2)}{\lambda_{\gamma}(M1) + \lambda_{\gamma}(E2)} \tag{3.19}$$

where each λ indicates the decay constant for a certain decay mode, either internal conversion (ce) or γ-ray decay (γ).

Reminding the definitions of multipolarity mixing ratio and internal conversion coefficient in Eq. (1.18) and Eq. (1.24), one can write:

$$\delta^2(E2/M1) = \frac{\lambda_{\gamma}(E2)}{\lambda_{\gamma}(M1)}, \quad \alpha(M1) = \frac{\lambda_{\mathrm{ce}}(M1)}{\lambda_{\gamma}(M1)}, \quad \alpha(E2) = \frac{\lambda_{\mathrm{ce}}(E2)}{\lambda_{\gamma}(E2)} \tag{3.20}$$

It is possible to define also the mixing ratio $q^2(E0/E2)$ between the $E0$ and $E2$ components of the internal conversion decay, which was firstly introduced by Church and Weneser [32]:

$$q^2(E0/E2) \equiv \frac{\lambda_{\mathrm{ce}}(E0)}{\lambda_{\mathrm{ce}}(E2)} \tag{3.21}$$

Using Eqs. (3.20) and (3.21), it follows that the experimental internal conversion co-

efficient in Eq. (3.19) can be rewritten, in particular for the K-shell, as [79]:

$$\begin{aligned}\alpha_{\mathrm{K,exp}} &= \frac{q_{\mathrm{K}}^2\lambda_\gamma(E2)\alpha_{\mathrm{K}}(E2) + \frac{\lambda_\gamma(E2)}{\delta^2}\alpha_{\mathrm{K}}(M1) + \lambda_\gamma(E2)\alpha_{\mathrm{K}}(E2)}{\frac{\lambda_\gamma(E2)}{\delta^2} + \lambda_\gamma(E2)} = \\ &= \frac{\delta^2(1+q_{\mathrm{K}}^2)\,\alpha_{\mathrm{K}}(E2) + \alpha_{\mathrm{K}}(M1)}{1+\delta^2} \end{aligned} \tag{3.22}$$

where q_{K}^2 and δ^2 have been used to shorten the notation $q_{\mathrm{K}}^2(E0/E2)$ and $\delta^2(E2/M1)$. The coefficients $\alpha_{\mathrm{K}}(M1)$ and $\alpha_{\mathrm{K}}(E2)$ are calculated through the BrIcc calculator [68] for a transition of the considered energy which is either pure $M1$ or pure $E2$. Therefore, inverting this relationship, one can write q_{K}^2 in terms of quantities that can be either measured [$\alpha_{\mathrm{K,exp}}$ and δ^2] or calculated [$\alpha(M1)$ and $\alpha(E2)$]:

$$q_{\mathrm{K}}^2(E0/E2) = \frac{\alpha_{\mathrm{K,exp}}(1+\delta^2) - \alpha_{\mathrm{K}}(M1)}{\delta^2\,\alpha_{\mathrm{K}}(E2)} - 1 \tag{3.23}$$

Once q_{K}^2 is known, it becomes possible to calculate the decay constant $\lambda_{\mathrm{K}}(E0)$ relative to, for example, $\lambda_\gamma(E2)$:

$$\lambda_{\mathrm{K}}(E0) = q_{\mathrm{K}}^2\,\lambda_{\mathrm{K}}(E2) = q_{\mathrm{K}}^2\,\alpha_{\mathrm{K}}(E2)\,\lambda_\gamma(E2) \tag{3.24}$$

The subscript K indicates that q^2 and λ are determined for the K-shell component of the internal conversion decay. Only the K-shell contribution to α_{exp} and $\lambda_{\mathrm{ce}}(E0)$ is considered in this work. Indeed, it is possible to re-write Eq. (3.16) only in terms of the K-shell component as [80]:

$$\rho^2(E0) = \frac{1}{\Omega_{\mathrm{K}} \times \tau_{\mathrm{K}}(E0)} \tag{3.25}$$

Here, the partial lifetime $\tau_{\mathrm{K}}(E0) = 1/\lambda_{\mathrm{K}}(E0)$ can be derived using the expression in Eq. (3.24), supposing that the γ-ray transition probability $\lambda_\gamma(E2)$ is known, either from lifetimes or $B(E2)$ measurements, therefore yielding the value of $\rho^2(E0)$. Equation (3.25) follows from the fact that the transition probability for the j^{th} shell, λ_j, is related to the total $E0$ one, $\lambda_{\mathrm{ce}}(E0)$, by:

$$\lambda_j = \frac{\Omega_j}{\sum_j \Omega_j}\lambda_{\mathrm{ce}}(E0) \tag{3.26}$$

In the case of $0^+ \rightarrow 0^+$ transitions, which occur only via the $E0$ mode, the mixing ratio $q^2(E0/E2)$ is defined taking as reference the $E2$ decay mode of a competing $0^+ \rightarrow 2^+$ branch. Typically, the decay to the first excited 2^+ state is considered. In the very special case that the first excited 0^+ state is also the very first excited state, as it happens in the nucleus ^{72}Ge, the total lifetime of the state coincides with the partial lifetime $\tau(E0)$. Thus, a direct application of Eq. (3.16) yields the measurement of $\rho^2(E0)$ for such $0^+ \rightarrow 0^+$ transitions.

Once all the necessary observables – such as internal conversion coefficients and multipolarity mixing ratios – have been measured for the transitions of interest, the UNCtool software has been used to determine the value of $\rho^2(E0)$ through Eq. (3.16). UNCtool

has been developed by the Nuclear Physics group of the Australian National University [81]. It is used to calculate electric monopole strengths by modeling the experimental quantities as random variables distributed with a Gaussian probability. The mean and standard deviation of the Gaussian distributions are set to the measured values and their uncertainties. The functionality of UNCtool is similar to that one of the NIST Uncertainty Machine web application, developed by the National Institute of Standards and Technology [82]. UNCtool, though, is specifically designed for nuclear structure studies: it uses as input a ENSDF-format datafile [83] and it is integrated with BrIcc [68], to allow the calculation of the proper theoretical internal conversion coefficients α and electronic factors Ω needed to determine the $\rho^2(E0)$ values.

3.7 Determining γ-ray Decay Branching Ratios

In this section, the techniques used to determine the γ-ray branching ratios for the 0_2^+ states of the nuclei of interest are briefly summarized. In this work, coincidence data were used for such a measurement, to achieve the cleanest spectrum possible and to enhance the weak transitions of interest relative to their more intense neighbouring peaks. Energy gates were set either on transitions which lie above the 0_2^+ state and that populates it, or on transitions that are below the γ-ray decay branches from the 0_2^+ state. These two methods are referred to as gating from above and gating from below, respectively. In the case an expected transition from the 0_2^+ state to a lower energy one was not observed, an upper limit on its area, and therefore on its branching ratio, was set.

Branching ratio measurements have been used in this work to determine the partial lifetime τ_γ of each γ-ray decay branch, defined in Eq. (1.20). In this way, reduced transition probabilities $B(E2)$ could be determined for each branch, as will be discussed in Section 4.5.

3.7.1 Gating from Above

Let γ_f be a γ-ray feeding the level of interest, as sketched in Fig. 3.5. To determine the branching ratio B.R.$_{\gamma_d}$ of each γ-ray decay branch of this level, it will be sufficient to set an energy gate on the transition γ_f and measure the areas of all the γ-ray branches in coincidence with it. To obtain the branching ratio measurement for the i^{th} transition, one will use the following expression:

$$\text{B.R.}^i_{\gamma_d} = \frac{A^i_{\gamma_d}/\epsilon^i_{\gamma_d}}{\sum_j A^j_{\gamma_d}/\epsilon^j_{\gamma_d}} \tag{3.27}$$

where $A^i_{\gamma_d}$ is the measured peak area for the i^{th} transition, $\epsilon^i_{\gamma_d}$ is the detection efficiency at the i^{th} transition energy, and the sum over j is extended to all the γ-ray decay branches from the level of interest. The peak area corrected by the efficiency, A/ϵ, represents the relative intensity I of each transition.

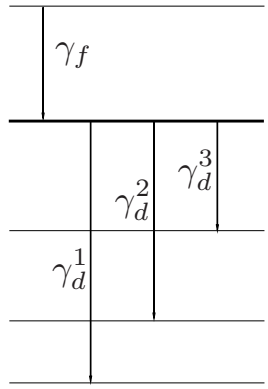

Figure 3.5: Example of level scheme where it is possible to gate from above on the transition γ_f to measure the branching ratios from the level of interest (highlighted in bold) for the γ_d^i transitions.

3.7.2 Gating from Below

Whenever it is not possible to use the gating from above method, for example for lack of statistics, it is useful to employ the gating from below method, where coincidences between the γ-ray decay branches from the level of interest, γ_f^i, and γ-ray transitions below them, γ_d^i, are considered (see the sketch in Fig. 3.6). In this case, the number of coincidences N_{fd} for each pair of γ rays, γ_f and γ_d, can be written as [84]:

$$N_{fd} = N I_{\gamma_f} \epsilon_{\gamma_f} \text{B.R.}_{\gamma_d} \epsilon_{\gamma_d} \epsilon_{fd} \eta(\theta_{fd}) \tag{3.28}$$

where N is a normalization factor, ϵ_{γ_f} and ϵ_{γ_d} are the detection efficiencies at the energy of γ_f and γ_d, respectively, B.R.$_{\gamma_d}$ is the branching ratio of the transition γ_d, ϵ_{fd} is the coincidence detection efficiency and $\eta(\theta_{fd})$ is an angular correlation attenuation factor. Given the properties of the level schemes under investigation and the time coincidence windows used, the coincidence efficiency ϵ_{fd} can be taken as equal to 1. Since the GRIFFIN array is symmetric, also the attenuation factor $\eta(\theta_{fd})$ can be set to 1. Therefore the intensity of each branch can be written as:

$$I_{\gamma_f} = \frac{N_{fd}}{N \epsilon_{\gamma_f} \text{B.R.}_{\gamma_d} \epsilon_{\gamma_d}} \tag{3.29}$$

It is then possible to calculate the branching ratio for each transition depopulating the level of interest using:

$$\text{B.R.}^i_{\gamma_f} = \frac{I^i_{\gamma_f}}{\sum_j I^j_{\gamma_f}} \tag{3.30}$$

where the sum over j is extended to all the γ-ray decay branches. Note that the normalization factor N will cancel out, therefore it is not necessary to determine it for a branching ratio measurement.

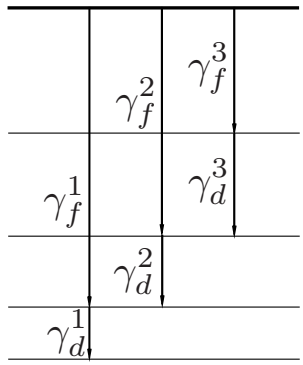

Figure 3.6: Example of level scheme where it is possible to gate from below to measure the branching ratios of the γ-ray branches from the level of interest (highlighted in bold). For each transition γ_f^i from the level of interest, a gate is set on the transition γ_d^i.

3.7.3 Setting Upper Limits

When an expected transition was not observed, an upper limit on its area was established with a 95% confidence limit, defined by Currie [85], according to the method described in Ref. [86].

A critical limit L_{C} can be defined, which is the number of counts below which a peak can be affirmed not to be statistically significant.

Suppose that the energy spectrum shows only background counts in a given region, because no γ-ray transition is present at such an energy. In this case, the mean net count or area A above the background will be zero, but distributed with a Gaussian probability above and below zero (see Fig. 3.7). The spread or standard deviation of this distribution will be indicated as σ_0. In the case one measures an area A and wants to discriminate if it is statistically significant or not, they can affirm it is significant if it exceeds a certain number of standard deviations σ_0, namely if $A > k_\alpha \cdot \sigma_0$. The factor k_α will be selected to provide a certain degree of confidence in the conclusion. For a confidence level of 95%, which in statistical probability terms corresponds to $\alpha = 0.05$, k_α would be 1.645. This is in contrast with the typical 2σ limit for a confidence level of 95%, because here one-tailed probability distributions are considered to determine the critical limit, instead of two-tailed probability distributions, as shown in Fig. 3.7. Indeed, it is of interest to determine only if the critical limit is exceeded. Therefore the critical limit would be $L_{\mathrm{C}} = 1.645\sigma_0$.

In practice, σ_0 needs to be determined by the sample and background estimates. Reminding that for a Poisson-distributed variable σ^2(count) = count, and that the net number of counts in a peak is calculated as the difference between the number of counts

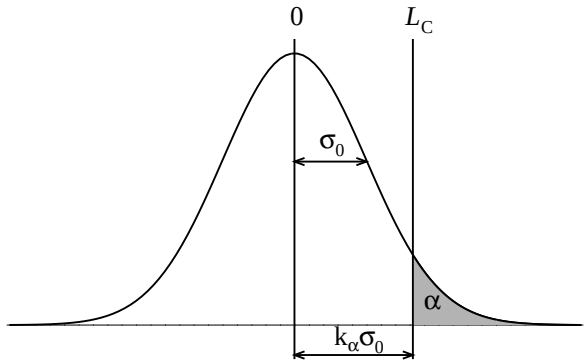

Figure 3.7: Probability distribution of the background counts, centered at 0 and with a spread equal to σ_0. For a given α value (or confidence limit), the critical limit L_C is $k_\alpha\sigma_0$, with k_α so that the area subtended by the probability distribution function below the L_C is $1-\alpha$.

in the peak region and the background counts, it follows that:

$$\sigma^2(\text{net counts}) = \text{net counts} + \text{background} + \sigma^2(\text{background}) \tag{3.31}$$

Let A be the net peak area and B the estimate of the background counts below it. The variance of the background estimate will be [86]:

$$\sigma^2(B) = nB/2m \tag{3.32}$$

where n is the width of the peak in number of channels and m is the width in channels of the lower and upper background regions considered to estimate the background B below the peak. In the case when $n = 2m$, the variance of B reduces to B, as for the case of a single channel count. Equation (3.31) can therefore be written as:

$$\sigma^2(A) = A + B + nB/2m \tag{3.33}$$

Taking the net peak area A equal to zero, the variance will read:

$$\sigma^2(A=0) = B + nB/2m = B(1 + n/2m) \equiv \sigma_0^2 \tag{3.34}$$

After estimating the spread σ_0, it is possbile to determine the critical limit L_C as:

$$L_C = 1.645\sqrt{B(1+n/2m)} \tag{3.35}$$

If the observed net area A is below the critical limit L_C, it can be affirmed that no activity has been detected and an upper limit L_U on the area can be quoted, which does for sure exceed the peak area, if there were any. This is defined as [86]:

$$L_U = A + k_\alpha\sigma_A \tag{3.36}$$

where σ_A is the uncertainty of the measured net area A [see Eq. (3.33)]. For the 95% confidence limit, this becomes:

$$L_{\mathrm{U}} = A + 1.645\sqrt{A + B(1 + n/2m)} \tag{3.37}$$

In the case the net area A were zero, this would reduce to the critical limit L_{C} definition. If the measured net number of counts in the area results less than zero, when calculating it as:

$$A = G - B \tag{3.38}$$

with G gross area in the peak region and B background estimate, according to the Covell method described in Ref. [86], A should not be included in the calculation of L_{U}, because including it would yield an underestimate of the upper limit. The aforementioned Covell method has been used in this work when determining upper limits to areas, since a peak fit as described in Section 3.3 would obviously be not possible in a situation where no peak can be distinguished above the background level.

4

RESULTS AND DISCUSSION

In order to investigate mixed configurations of low-lying states of ^{72,74,76,78}Ge, the $E0$ strength $\rho^2(E0)$ of their $2_2^+ \rightarrow 2_1^+$ transition has been measured in this work. Upper limits on the $\rho^2(E0; 0_2^+ \rightarrow 0_1^+)$ value could also be established for ^{74,78}Ge. Lastly, weak γ-ray decay branches from the 0^+ states of ^{74,76,78}Ge have been investigated and branching ratio measurements have been performed.

This chapter presents the obtained results. Firstly, the measurements of electromagnetic mixing ratio δ and internal conversion coefficient α needed to calculate $\rho^2(E0)$ are described. Afterwards, the branching ratio measurements are presented. Finally, the calculated $E0$ strengths and reduced transition probabilities $B(E2)$ are discussed.

4.1 Electromagnetic Mixing Ratios

In this section, the $\gamma\gamma$ angular correlation analysis performed to determine the $E2/M1$ mixing ratio of the $2_2^+ \rightarrow 2_1^+$ transitions of ^{72,74,76,78}Ge will be presented. The analysis has been carried out following the procedure previously described in Section 3.4. The 2019 dataset has been used to perform this analysis, with the HPGe clovers installed at a distance of 14.5 cm from the implantation point at the centre of the array (see Section 2.5.2).

Previous results from literature on the mixing ratio values will be firstly presented. Afterwards, a discussion of the analysis performed in this work will follow.

4.1.1 Previous Results from Literature

Measurements of the $E2/M1$ mixing ratio of the $2_2^+ \rightarrow 2_1^+$ transitions of ^{72,74,76}Ge performed prior to this work are summarized in Table 4.1. These were obtained either through $\gamma\gamma$ angular correlations or γ angular distributions. No measurement was previously reported for the mixing ratio of such a transition in ^{78}Ge.

Table 4.1: Mixing ratio values δ of the $2_2^+ \rightarrow 2_1^+$ transitions of ^{72,74,76}Ge reported in literature, with references. For each measurement, it is indicated if the result was obtained through $\gamma\gamma$ angular correlations [$\gamma\gamma(\theta)$] or γ angular distributions [$\gamma(\theta)$]. The reaction or decay process used to populate the isotope of interest is also reported. Results are presented using the sign convention introduced by Krane and Steffen [28].

Nucleus	Technique	Production Process	$\delta(2_2^+ \rightarrow 2_1^+)$	Reference
^{72}Ge	$\gamma\gamma(\theta)$	^{72}Ga β-decay	$-10.3(13)$	[42]
	$\gamma(\theta)$	^{70}Zn(α,2nγ)^{72}Ge	$-0.35\ ^{-0.20}_{+0.10}$	[87]
^{74}Ge	$\gamma\gamma(\theta)$	^{74}As ϵ-decay	$+3.4(4)$	[41]
^{76}Ge	$\gamma(\theta)$	^{76}Ge(n,n'γ)	$+3.5(15)$	[40]
	$\gamma\gamma(\theta)$	Coulex	$+2.1(4)$	[50]
	$\gamma(\theta)$	^{76}Ge(n,n'γ)	$+2.5(2)$	[88]

4.1.2 Angular Correlation Analysis

The aim of the $\gamma\gamma$ angular correlation analysis presented in this work is to determine the $E2/M1$ mixing ratio value, δ, of the $2_2^+ \rightarrow 2_1^+$ transitions in the ^{72,74,76,78}Ge isotopes. In the following, the procedure used to assess the proper functioning of the analysis is presented, for which stretched $E2$-$E2$ γ-ray cascades have been used. Afterwards, the analysis performed to obtain the mixing ratio measurements is discussed. A set of 1000 GEANT4 simulations of 10^6 events was run for each γ-ray cascade considered [76]; these have been used in the analysis to take into account the finite size detector effects, as described in Section 3.4.2.

Validation of the method with pure $E2$-$E2$ cascades

The proper functioning of the analysis method with the current dataset and simulations has been tested using cascades with well known spins and stretched $E2$ transitions.

The cascades $0_2^+ \xrightarrow{\gamma_1} 2_1^+ \xrightarrow{\gamma_2} 0_1^+$ and $4_1^+ \xrightarrow{\gamma_1} 2_1^+ \xrightarrow{\gamma_2} 0_1^+$ in ^{72,74,76,78}Ge were considered. For the case of ^{72}Ge, only the $4_1^+ \rightarrow 2_1^+ \rightarrow 0_1^+$ cascade was used, since the 0_2^+ state decays directly to the 0_1^+ ground state via an $E0$ transition, therefore no $0_2^+ \rightarrow 2_1^+$ γ-ray branch is present. Since in such cascades the δ values are required to be null for both the transitions γ_1 and γ_2, the fit of the simulated distributions $Z_i(\theta)$ to the experimental data points was carried out with only one free parameter, namely the scaling factor A_{00} [see Eq. (3.13)]. According to the recommendation of Robinson [74], any spin assignments that yielded a reduced χ^2 which falls below the 99% confidence limit should be accepted. In the cases considered here, since the spin assignments are known, the fit of the experimental angular correlations is used to confirm that a reduced χ^2 below the 99% confidence limit would be obtained. In this way, the experimental procedure can be validated. 49 data points have been used for each experimental cascade. The two datapoints corresponding to the smallest angular bins available at GRIFFIN, that represent the angular difference between crystal pairs within the same clover detector, have been discarded in the analysis, since they were highly affected by the Compton background. Hence, the number of degrees of freedom of the fits is $\nu = N - 1 = 48$, which then yields

$\chi^2/\nu_{\mathrm{CL}} = 1.535$ for the 99% confidence limit.

The results of the fits for the stretched $E2$-$E2$ test cascades are summarized in Table 4.2. Figures 4.1 and 4.2 show the fitted experimental angular correlations of the cascades of ^{78}Ge, as an example of the obtained results. In the plots, the experimental angular correlation points and uncertainties are presented in the top panel, with black dots and error bars. The best fit curve $Z_{\mathrm{sum}}(\theta)$ of the simulated distributions to the data is represented by the red curve, whose thickness indicates the statistical uncertainty on the simulations. Note that the top panel plots in Fig. 4.1 and Fig. 4.2 have different y-axis ranges. Therefore, the fitted curve thickness is different, despite the statistical uncertainties on the simulated distributions are comparable. The bottom panel shows the residuals of the data points relative to the fitted curve; here, the uncertainty includes both the experiment and simulations contributions. The same considerations apply to all the angular correlation plots shown in this chapter. Plots of the correlations of the remaining cascades considered for this test and listed in Table 4.2 can be found in Appendix B.

Table 4.2: Angular correlation results for stretched $E2$-$E2$ $I_i^\pi \xrightarrow{\gamma_1} I^\pi \xrightarrow{\gamma_2} I_f^\pi$ cascades of the ^{72,74,76,78}Ge nuclei. The γ-ray energies, E_{γ_1} and E_{γ_2}, are reported in the third column (in keV). The number of coincidence counts are also indicated. The χ^2/ν values obtained by fitting the angular correlations by the scaling factor A_{00} and requiring $\delta_1 = \delta_2 = 0$ are listed in the last column. The number of degrees of freedom ν is equal to $49 - 1 = 48$, since 49 experimental points have been used and only one free parameter, A_{00}, is considered for the fit.

Nucleus	$I_i^\pi \to I^\pi \to I_f^\pi$	E_{γ_1}-E_{γ_2}	Counts	χ^2/ν
^{72}Ge	$4_1^+ \to 2_1^+ \to 0_1^+$	894-834	7.66×10^5	1.298
^{74}Ge		868-596	6.83×10^6	1.515
^{76}Ge		847-563	2.79×10^6	1.390
^{78}Ge		951-619	9.40×10^6	1.005
^{74}Ge	$0_2^+ \to 2_1^+ \to 0_1^+$	887-596	2.76×10^5	1.112
^{76}Ge		1348-563	4.87×10^5	1.325
^{78}Ge		927-619	1.22×10^6	1.067

Study of $2_2^+ \to 2_1^+ \to 0_1^+$ cascades

Experimental angular correlations of the $2_2^+ \xrightarrow{\gamma_1} 2_1^+ \xrightarrow{\gamma_2} 0_1^+$ γ-ray cascades of ^{72,74,76,78}Ge have been fitted to the simulated distributions, considering the scaling factor A_{00} and the mixing ratio δ_1 as free parameters. The results of such analyses are presented in Table 4.3 and in Figs. 4.3 to 4.6. Also in these cases, 49 data points have been used, since the two datapoints corresponding to the smallest angular bins have been discarded. Therefore, the number of degrees of freedom is $\nu = N - 2 = 47$, which corresponds to a reduced χ^2 value of $\chi^2/\nu_{\mathrm{CL}} = 1.5413$ for the 99% confidence limit. Note that for the cascades of ^{74,78}Ge the reduced χ^2 exceeds this limit. The spin assignment of the 2_2^+ state, though, is firmly established. Therefore, one must conclude that by analysing this ultra-high-stratistics dataset ($\sim 10^7$ coincidence counts per cascade, see Table 4.3), the limitations of

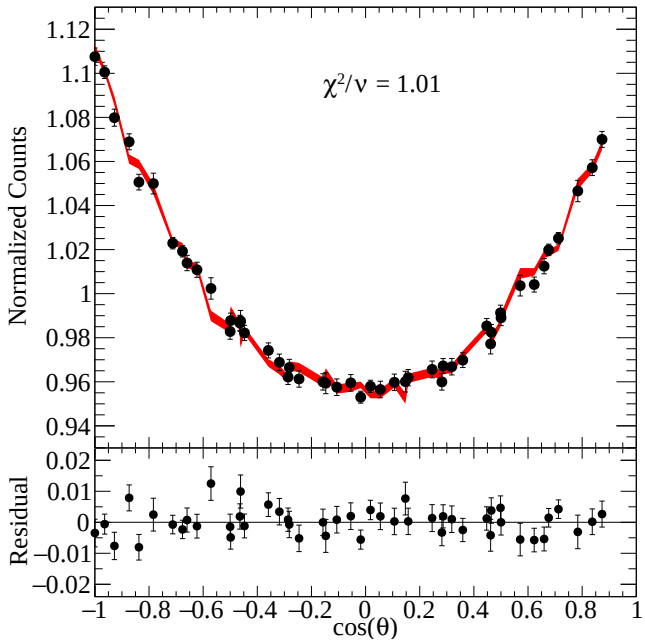

Figure 4.1: Experimental angular correlation of the $4_1^+ \xrightarrow{\gamma_1} 2_1^+ \xrightarrow{\gamma_2} 0_1^+$ 951-619 keV γ-ray cascade of ^{78}Ge. Data are fitted to the simulated $Z_i(\theta)$ distributions using A_{00} as the only free parameter, fixing $\delta_1 = \delta_2 = 0$.

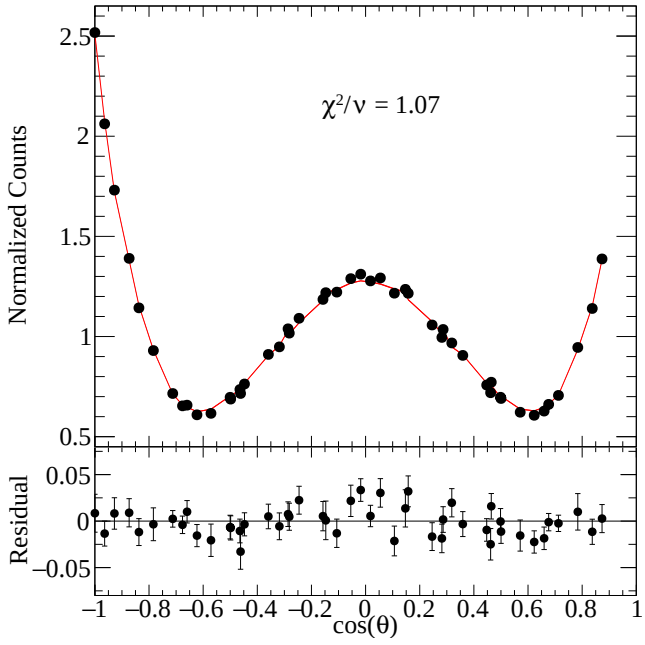

Figure 4.2: Experimental angular correlation of the $0_2^+ \xrightarrow{\gamma_1} 2_1^+ \xrightarrow{\gamma_2} 0_1^+$ 927-619 keV γ-ray cascade of ^{78}Ge. Data are fitted to the simulated $Z_i(\theta)$ distributions using A_{00} as the only free parameter, fixing $\delta_1 = \delta_2 = 0$.

the GEANT4 simulations approach to take account of the finite size of the detectors have been met. This can include, but is not limited to, the fact that the simulated geometry does not take into account a possible misplacement (of few mm) of the detectors from their nominal position at 14.5 cm of distance from the implantation point, due for example to an incomplete closure of the GRIFFIN array. To avoid an underestimate of the uncertainty on the measured δ value, this has been inflated by $\sqrt{\chi^2/\nu}$.

For all the isotopes, the $2_2^+ \rightarrow 2_1^+$ transition is dominated by its $E2$ component relative to the $M1$ one. Note that for ^{72}Ge the δ value obtained with this analysis is inconsistent with both the previous measurements reported in Table 4.1. These last ones, though, are also inconsistent between each other.

The experimental correlations have been fitted also using the a_2 and a_4 coefficients as free parameters, together with the scaling factor A_{00}, instead of minimizing by δ_1. The best-fit values for a_2 and a_4 are also presented in Table 4.3. The covariance matrices of such fits are reported in Appendix C.

Table 4.3: Angular correlation results for the $2_2^+ \xrightarrow{\gamma_1} 2_1^+ \xrightarrow{\gamma_2} 0_1^+$ γ-ray cascades of the ^{72,74,76,78}Ge nuclei. The γ-ray energies, E_{γ_1} and E_{γ_2}, are reported in the second column (in keV), while in the third column the number of coincidence counts is listed for each cascade. The mixing ratio values determined for the $2_2^+ \xrightarrow{\gamma_1} 2_1^+$ transitions (δ_1^{exp}) by fitting the simulated distributions to the datapoints using the A_{00} and δ_1 parameters are presented, together with the reduced χ^2 values of such fits. The mixing ratio δ_2 has been set as equal to zero, since the $2_1^+ \xrightarrow{\gamma_2} 0_1^+$ transition is stretched. The uncertainty on the δ_1^{exp} values is already properly inflated to take into account the excess above unity of the reduced χ^2. The experimental correlations were fitted also using the a_2 and a_4 coefficients as free parameters, together with the A_{00} scaling factor. The best fit a_2 and a_4 parameters are listed in the sixth and seventh column.

Nucleus	E_{γ_1}-E_{γ_2}	Counts	δ_1^{exp}	χ^2/ν	a_2^{exp}	a_4^{exp}
^{72}Ge	630-834	2.44×10^6	$+26(2)$	1.443	$-0.104(2)$	0.327(3)
^{74}Ge	608-596	1.48×10^7	$+2.87(3)$	1.750	$-0.2691(14)$	0.294(2)
^{76}Ge	546-563	2.81×10^7	$+1.85(2)$	1.502	$-0.3096(12)$	0.2539(15)
^{78}Ge	567-619	3.10×10^7	$+2.46(3)$	1.837	$-0.2847(12)$	0.178(2)

4.2 Internal Conversion Coefficients

In this section, results of the internal conversion coefficient measurements are presented for the $2_2^+ \rightarrow 2_1^+$ transitions of the Ge isotopes of interest. The measurements have been performed using PACES and GRIFFIN spectra, with the technique described in Section 3.5. Details on both the 2017 and 2019 dataset analyses are provided. At the end of the section, the averaged results of the two experiments and of different PACES crystals are presented.

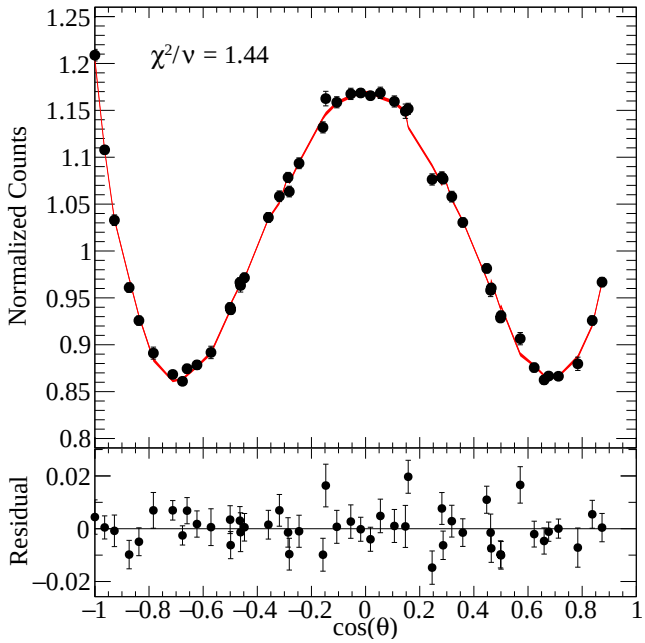

Figure 4.3: Experimental angular correlation of the $2_2^+ \xrightarrow{\gamma_1} 2_1^+ \xrightarrow{\gamma_2} 0_1^+$ 630-834 keV γ-ray cascade of ^{72}Ge. Data are fitted to the simulated $Z_i(\theta)$ distributions using A_{00} and δ_1 as free parameters.

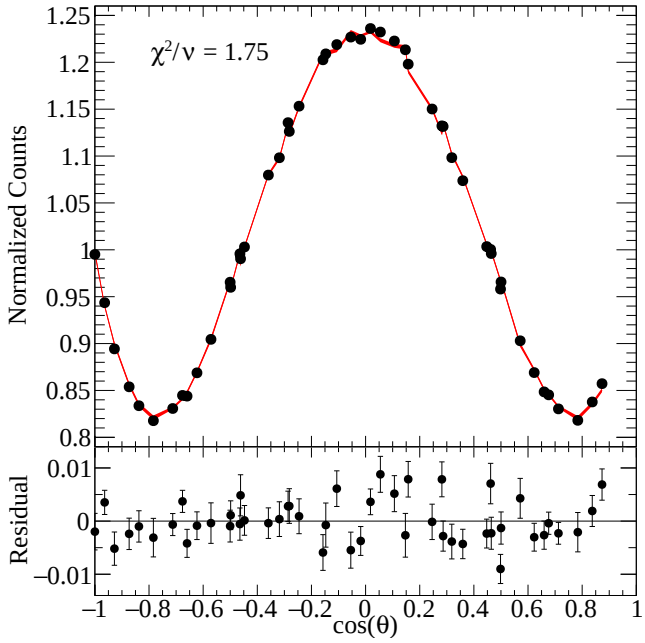

Figure 4.4: Experimental angular correlation of the $2_2^+ \xrightarrow{\gamma_1} 2_1^+ \xrightarrow{\gamma_2} 0_1^+$ 608-596 keV γ-ray cascade of ^{74}Ge. Data are fitted to the simulated $Z_i(\theta)$ distributions using A_{00} and δ_1 as free parameters.

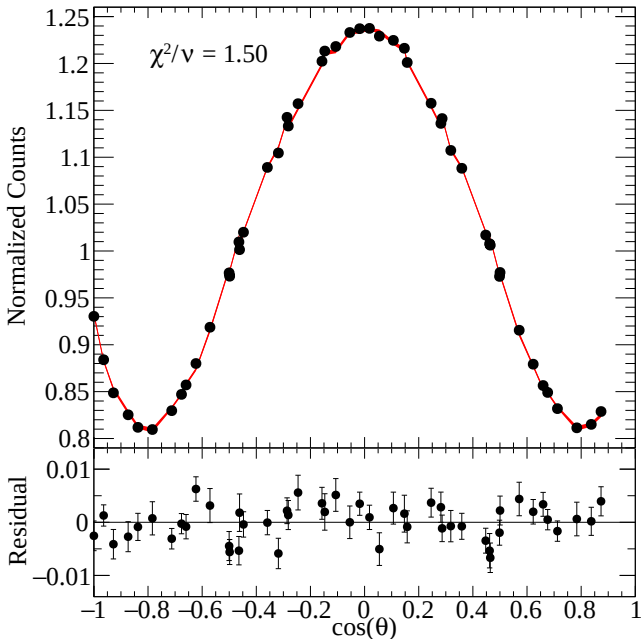

Figure 4.5: Experimental angular correlation of the $2_2^+ \xrightarrow{\gamma_1} 2_1^+ \xrightarrow{\gamma_2} 0_1^+$ 546-563 keV γ-ray cascade of ^{76}Ge. Data are fitted to the simulated $Z_i(\theta)$ distributions using A_{00} and δ_1 as free parameters.

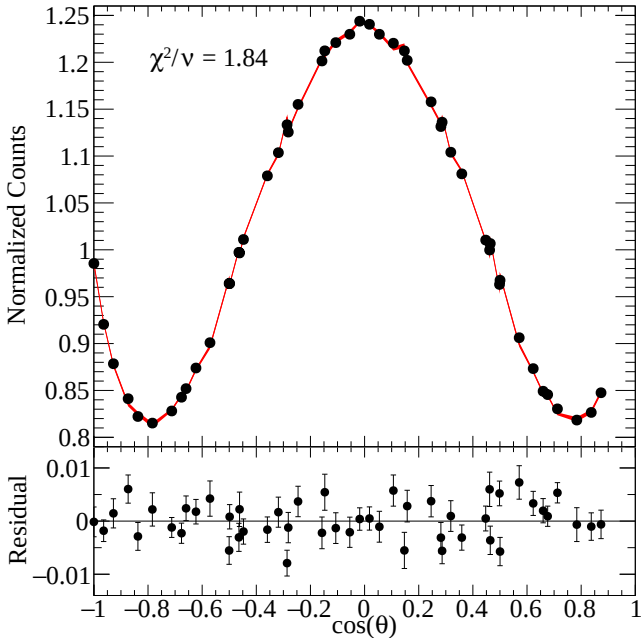

Figure 4.6: Experimental angular correlation of the $2_2^+ \xrightarrow{\gamma_1} 2_1^+ \xrightarrow{\gamma_2} 0_1^+$ 567-619 keV γ-ray cascade of ^{78}Ge. Data are fitted to the simulated $Z_i(\theta)$ distributions using A_{00} and δ_1 as free parameters.

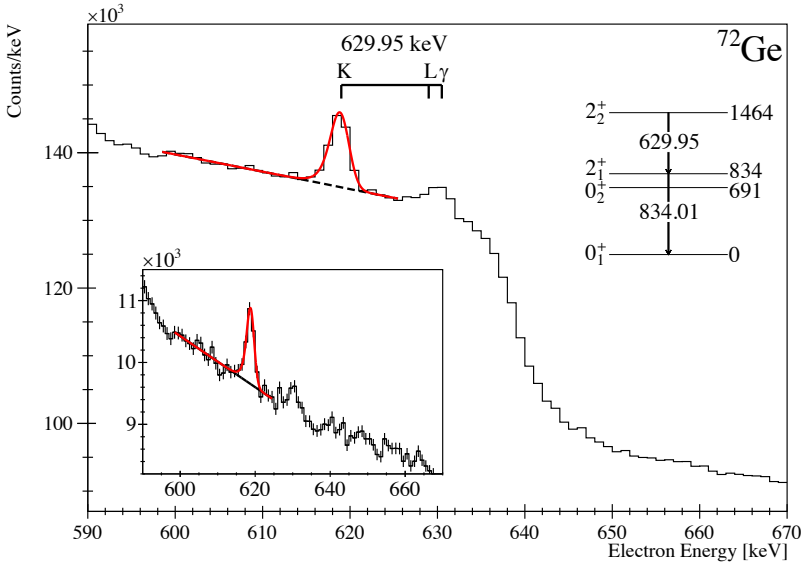

Figure 4.7: Spectrum in singles of PACES 2 and 5 for ^{72}Ge data from the 2017 beam time. A fit of the K-shell peak of the 630-keV, $2_2^+ \rightarrow 2_1^+$ transition of ^{72}Ge is shown. A partial level scheme of ^{72}Ge indicates the relevant transitions. The inset shows the PACES spectrum GRIFFIN-gated on the 834-keV transition. Such gate suppresses the Compton edge at ≈638 keV in PACES spectrum.

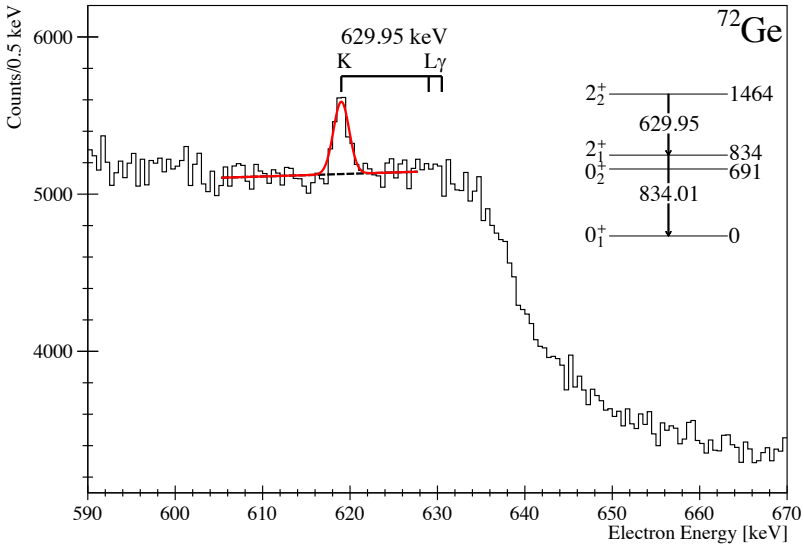

Figure 4.8: Spectrum in singles of PACES 2 for ^{72}Ge data from the 2019 beam time. A fit of the K-shell peak of the 630-keV, $2_2^+ \rightarrow 2_1^+$ transition of ^{72}Ge is shown. A partial level scheme of ^{72}Ge indicates the relevant transitions. With this level of statistics, the L-shell and photo-peaks are not visible in the spectrum.

4.2.1 Dataset of 2017

The sum of the spectra from the PACES 2 and 5 crystals was used for the analysis of the 2017 dataset, instead of treating the spectra separately, because this approach facilitated the fitting procedure. Only the K-shell peak of the 630-keV, $2_2^+ \rightarrow 2_1^+$ transition of ^{72}Ge was fitted in the PACES spectrum (see Fig. 4.7). In this case, the L-shell and photo-peak of this transition lie close to the sharp Compton edge of the 834-keV, $2_1^+ \rightarrow 0_1^+$ transition (at ≈638 keV), such that including them in the fit prevents fit convergence, due to a lack of a satisfactory definition of the background shape. The measured $\alpha_{\mathrm{K,exp}}$ value is reported in Table 4.4.

To validate the result obtained with the PACES spectrum in singles, data in γ-coincidence were considered too for the measurement. In particular, a gate was set on the 834-keV γ-ray transition observed with GRIFFIN to remove its Compton edge from the PACES electron spectrum. The result of such gating is shown in the inset of Fig. 4.7. Even in this case, only the K-shell peak was fitted to ensure fit convergence. The $\alpha_{\mathrm{K,exp}}$ value measured with coincidence data is consistent with the value measured in singles, as can be seen in Table 4.4. Hence, this confirms the robustness of the fit in the singles spectrum, despite the proximity to the complex region of the Compton edge, and allows us to confidently accept that result, which has a lower statistical uncertainty relative to the coincidence one.

Table 4.4: Values of the internal conversion coefficient $\alpha_{\mathrm{K,exp}}$ for the $2_2^+ \rightarrow 2_1^+$ transition of ^{72}Ge measured with the 2017 dataset. The results were obtained using the sum of the spectra recorded by PACES 2 and PACES 5 in singles ($^{\mathrm{s}}$) and γ-coincidence ($^{\mathrm{c}}$), respectively. The internal conversion coefficient value $\alpha_{\mathrm{K,BrIcc}}$ calculated with BrIcc is also reported.

Nucleus	$\alpha_{\mathrm{K,BrIcc}}$	PACES #	$\alpha_{\mathrm{K,exp}}$
^{72}Ge	0.001053(15)	2+5	$0.001\,15(7)^{\mathrm{s}}$ $0.001\,17(14)^{\mathrm{c}}$

4.2.2 Dataset of 2019

Table 4.5 summarizes the internal conversion coefficient values measured with the 2019 dataset. The following paragraphs contain a detailed description of how the spectra were treated, mass by mass, to obtain these results.

Mass 72

Data in singles were used for measuring the $\alpha_{\mathrm{K,exp}}$ value for the $2_2^+ \rightarrow 2_1^+$ transition of ^{72}Ge. The PACES spectrum recorded with crystal 2 is shown as an example in Fig. 4.8. Here, it is possible to observe the lack of L-shell and photo-peak, relative to the 2017 dataset case (see Fig. 4.7), due to a lower statistics collected in the 2019 beam time. The fit of the peaks of the $2_2^+ \rightarrow 2_1^+$ transition in PACES spectra were constrained so that the width and tail of the fitted functions were consistent with the result of the more intense $2_1^+ \rightarrow 0_1^+$ transition peak.

Table 4.5: Values of internal conversion coefficients $\alpha_{K,exp}$ for the $2_2^+ \rightarrow 2_1^+$ transitions of ^{72,74,76,78}Ge measured with the 2019 dataset. Results obtained with PACES 2 and PACES 4 spectra are listed separately. Internal conversion coefficient values $\alpha_{K,BrIcc}$ calculated with BrIcc are also reported.

Nucleus	$\alpha_{K,BrIcc}$	PACES #	$\alpha_{K,exp}$
^{72}Ge	0.001053(15)	2	0.001 22(14)
		4	0.001 16(15)
^{74}Ge	0.001125(16)	2	0.0009(4) [1]
		2	0.0012(6) [2]
		4	0.0012(4)
^{76}Ge	0.001475(21)	2	0.0018(4)
		4	0.001 58(15)
^{78}Ge	0.001361(20)	2	0.001 29(9)
		4	0.001 31(5)

[1] GRIFFIN gate on the 493- and 498-keV transitions.
[2] GRIFFIN gate on the 1745-keV transition.

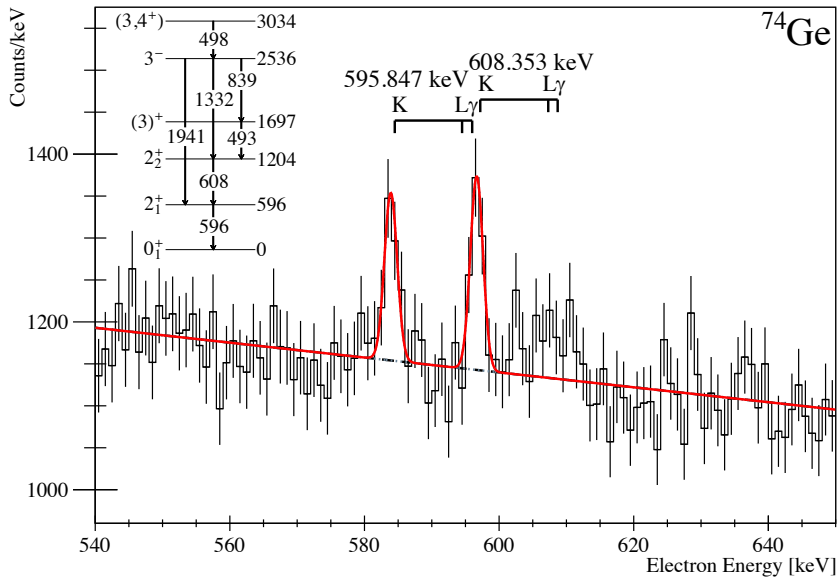

Figure 4.9: Spectrum of PACES 2 for ^{74}Ge data, in coincidence with the 493- and 498-keV transitions of ^{74}Ge detected with GRIFFIN. Data are from the 2019 beam time. A fit of the 596-keV, $2_1^+ \rightarrow 0_1^+$ and 608-keV, $2_2^+ \rightarrow 2_1^+$ transitions of ^{74}Ge is shown. A partial level scheme of ^{74}Ge indicates the relevant transitions. Only two peaks have been fitted here: the K-shell peak of the 596-keV transition and a peak that comprises the L-shell and photo-peak of the 596-keV transition and the K-shell of the 608-keV transition. It was not possible to isolate the L-shell and photo-peak of the 608-keV transition from the background.

Mass 74

The electron spectrum of ^{74}Ge poses some challenges when trying to measure the $\alpha_{\mathrm{K,exp}}$ value of the 608-keV, $2_2^+ \rightarrow 2_1^+$ transition. Indeed, as previously shown in Fig. 2.17, the 608-keV transition K-shell peak overlaps with those of the 596- and 604-keV transitions. It is not possible to successfully decouple the various peak contributions to the spectra in singles, despite constraining the peak areas in the fit on the basis of BrIcc information about α and of the ratio $R_{\gamma/\mathrm{K}}$ of the $2_1^+ \rightarrow 0_1^+$ defined in Eq. (2.9). For this reason, data in γ-coincidence were used to perform the $\alpha_{\mathrm{K,exp}}$ measurement for the $2_2^+ \rightarrow 2_1^+$ transition in ^{74}Ge.

The most intense 596-keV, $2_1^+ \rightarrow 0_1^+$ transition could not be used for this purpose, because the 608-keV transition is suppressed in this gated projection. This occurs since the β-decay population of the 2_1^+ state is significantly higher than the 2_2^+ one ($I_\beta(2_1^+) = 4.7(17)\%$, $I_\beta(2_2^+) < 1.2\%$) [41]. Hence, when gating on the 596-keV γ ray, the 608-keV transition in the electron spectrum is suppressed by the Compton background in coincidence with the 596-keV transition.

Thus, the GRIFFIN gates were set on transitions lying higher than the 2_2^+ state in the energy spectrum. In particular, the transitions of 493, 498 and 1745 keV were chosen (the gate on the 493- and 498-keV ones was set jointly). Figure 4.9 shows the spectrum of PACES 2 gated on the γ rays of 493 and 498 keV. For the spectrum of PACES 4, the 1745-keV gate did not provide a clean enough projection, so only the gate on the 493- and 498-keV transitions was used for this crystal. These gate choices suppress the 604-keV contribution from the electron spectrum. Indeed, the 498- and 1745-keV transitions are not in coincidence with it. The 493-keV transition, on the other hand, is reportedly in coincidence with the 604-keV transition. Nevertheless, when gating on it in a $\gamma\gamma$ matrix no coincidence with the 604-keV γ ray is observed. Hence, its detection in γ-coincidence is below the sensitivity of both the GRIFFIN and PACES detectors. In the gated electron projections, one peak that comprises the L-shell and photo-peak of the 596-keV transition and the K-shell of the 608-keV transition was fitted. The area, $A_{\mathrm{K},2\rightarrow2}$, of the K-shell peak of the 608-keV transition was determined by subtracting the proper number of counts associated with the L-shell and photo-peak of the 596-keV transition, $A_{\mathrm{L},2\rightarrow0}$ and $A_{\gamma,2\rightarrow0}$, based on the BrIcc α values and the previously measured $R_{\gamma/\mathrm{K}}$. This equation was used:

$$\begin{aligned} A_{\mathrm{K},2\rightarrow2} &= A - A_{\mathrm{L},2\rightarrow0} - A_{\gamma,2\rightarrow0} \\ &= A - \frac{\alpha_{\mathrm{L}}}{\alpha_{\mathrm{K}}} A_{\mathrm{K},2\rightarrow0} - R_{\gamma/\mathrm{K}} A_{\mathrm{K},2\rightarrow0} \end{aligned} \tag{4.1}$$

where A is the area of the fitted peak consisting of the three contibutions and $A_{\mathrm{K},2\rightarrow0}$ is the area of the K-shell peak of the 596-keV transition, that was also fitted.

Mass 76

Similarly to the ^{74}Ge case, even the electron spectrum of ^{76}Ge presents overlapping peaks in singles (see Fig. 2.18). Hence, data in γ-coincidence were used to clean the spectrum of PACES. In this case, a gate was set on the most intense γ-ray transition, namely the 563-keV, $2_1^+ \rightarrow 0_1^+$ one, to isolate the $2_2^+ \rightarrow 2_1^+$ electron peak. Here, a clean

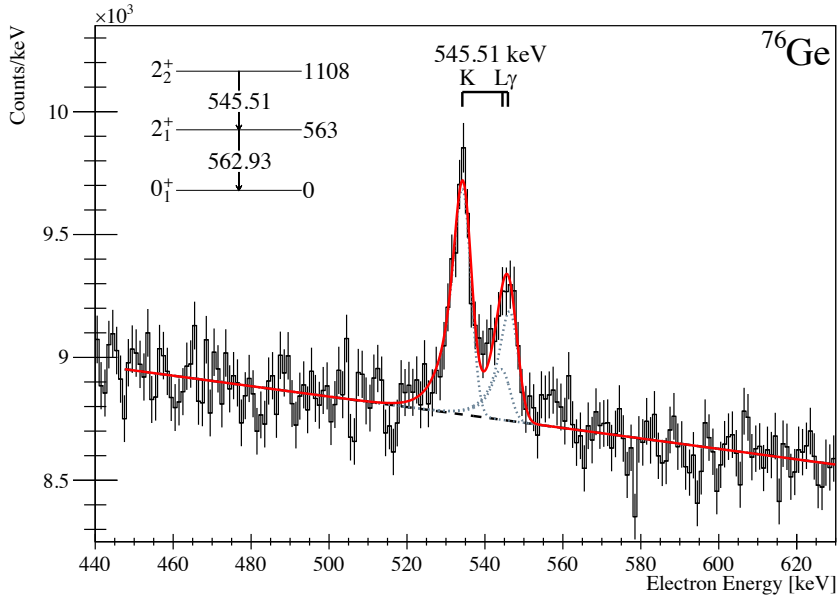

Figure 4.10: Spectrum of PACES 2 for ^{76}Ge data, in coincidence with the 563-keV, $2_1^+ \rightarrow 0_1^+$ transition of ^{76}Ge detected with GRIFFIN. Data are from the 2019 beam time. A fit of the 546-keV, $2_2^+ \rightarrow 2_1^+$ transition of ^{76}Ge is shown. A partial level scheme of ^{76}Ge indicates the relevant transitions. The fit includes the K-, L-shell and photo-peak of the 546-keV transition.

projection is obtained due to a more favourable ratio between the β-decay population of the 2_1^+ and 2_2^+ states ($I_\beta(2_1^+) = 14.2(15)\%$, $I_\beta(2_2^+) = 10.1(6)\%$ [40]), in comparison to the ^{74}Ge case. The resulting gated spectrum of PACES 2 can be observed in Fig. 4.10.

Mass 78

The electron spectrum of ^{78}Ge was analysed in singles, since here peaks associated with different transitions are well separated. An example of the fits performed for the peaks of the $2_2^+ \rightarrow 2_1^+$ transition are shown in Fig. 4.11. The fit was constrained so that the width and tail of the peaks were consistent with the width and tail of the peaks associated to the most intense 619-keV, $2_1^+ \rightarrow 0_1^+$ transition (also shown in Fig. 4.11).

4.2.3 Internal Conversion Coefficient Results

The $\alpha_{\text{K,exp}}$ results obtained with the 2017 and 2019 datasets and with different PACES detectors, previously listed in Tables 4.4 and 4.5, have been averaged in order to get a final result for the $2_2^+ \rightarrow 2_1^+$ transition of each of the considered germanium isotopes. The final results are presented in Table 4.6. The table also shows the ratio of the measured $\alpha_{\text{K,exp}}$ value to the $\alpha_{\text{K,BrIcc}}$ value calculated through BrIcc, considering the $E2/M1$ mixing ratio δ values presented in Section 4.1. Here, any excess above unity would point to the

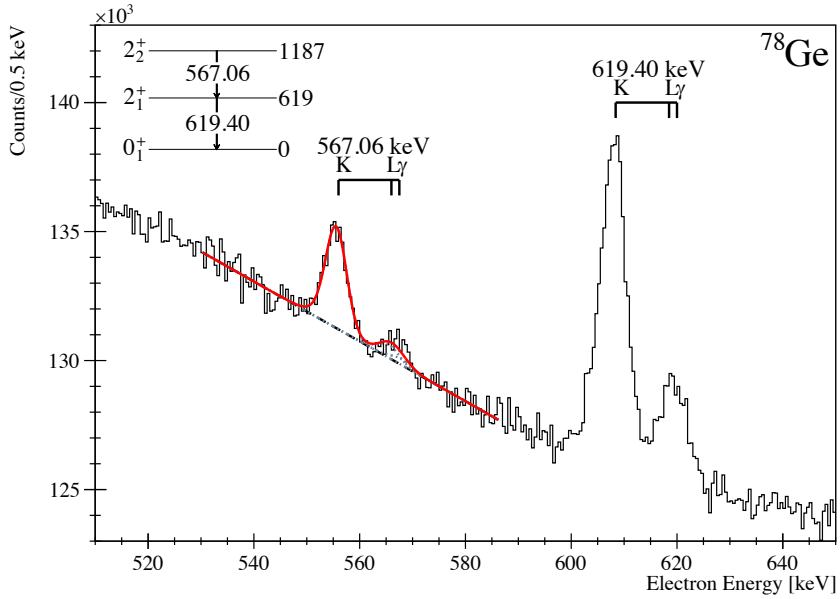

Figure 4.11: Spectrum in singles of PACES 2 for ^{78}Ge data. Data were acquired in 2019. A fit of the 567-keV, $2_2^+ \rightarrow 2_1^+$ transition of ^{78}Ge is shown. A partial level scheme of ^{78}Ge indicates the relevant transitions. The fit includes the K-, L-shell and photo-peak of the 567-keV transition.

presence of a finite $E0$ strength for the associated $2_2^+ \rightarrow 2_1^+$ transition.

Table 4.6: Final results for the internal conversion coefficients $\alpha_{\mathrm{K,exp}}$ of the $2_2^+ \rightarrow 2_1^+$ transitions of ^{72,74,76,78}Ge. They are obtained from the average of 2017 and 2019 datasets results. The values $\alpha_{\mathrm{K,BrIcc}}$ calculated with BrIcc and the ratio of the experimental results relative to them are also reported.

Nucleus	$\alpha_{\mathrm{K,BrIcc}}$	$\alpha_{\mathrm{K,exp}}$	$\alpha_{\mathrm{K,exp}}/\alpha_{\mathrm{K,BrIcc}}$
^{72}Ge	0.001 053(15)	0.001 16(6)	1.10(6)
^{74}Ge	0.001 125(16)	0.0011(3)	1.0(2)
^{76}Ge	0.001 475(21)	0.001 61(14)	1.09(10)
^{78}Ge	0.001 361(20)	0.001 31(4)	0.96(4)

4.3 Upper Limits on *E0* $0_2^+ \rightarrow 0_1^+$ Transition Intensities

The conversion electron spectra acquired with the PACES crystals in the 2019 dataset do not show peaks corresponding to the $0_2^+ \rightarrow 0_1^+$ transition via internal conversion decay of ^{74,76,78}Ge. Therefore, upper limits for the intensity of such transitions in ^{74,78}Ge have been set, following the method described in Section 3.7.3, in order to obtain an upper limit for the associated $E0$ strength. No upper limit could be set in the case of ^{76}Ge,

since an escape peak dominates the energy region of interest in the PACES spectra of this isotope, preventing to successfully determine an upper limit for the $0_2^+ \rightarrow 0_1^+$ transition intensity.

As discussed in Section 3.6, in the case of a $0_2^+ \rightarrow 0_1^+$ transition the $E0$ strength can be determined measuring the mixing ratio $q^2(E0/E2)$, which was defined in Eq. (3.21). For the K-shell, this reads as:

$$q^2_{\mathrm{K}}(E0/E2) \equiv \frac{\lambda_{\mathrm{ce,K}}(E0)}{\lambda_{\mathrm{ce,K}}(E2)} \tag{4.2}$$

where the considered $E2$ intensity corresponds to a $0^+ \rightarrow 2^+$ branch competing with the $E0$ decay mode. Reminding that [see Eq. (3.20)]:

$$\alpha_{\mathrm{K}}(E2) = \frac{\lambda_{\mathrm{ce,K}}(E2)}{\lambda_{\gamma}(E2)} \tag{4.3}$$

it follows that the mixing ratio $q^2_{\mathrm{K}}(E0/E2)$ can be calculated from the experimental quantity $\lambda_{\mathrm{ce,K}}(E2)/\lambda_{\gamma}(E2)$. An upper limit for such a ratio has been set, using the upper limit on the electron peak area and the $0_2^+ \rightarrow 2_1^+$ γ-ray peak area, both corrected by the detector efficiencies. The obtained results are listed in Table 4.7. Note that in the case of ^{74}Ge, a limit for this ratio was already published in literature, as indicated in the table, and such a limit was more stringent than the result obtained in this work. Therefore, the previous result provides a more stringent upper limit for $\rho^2(E0; 0_2^+ \rightarrow 0_1^+)$, as will be shown in the following section.

Table 4.7: Upper limits on the ratio $\lambda_{\mathrm{ce,K}}(E2)/\lambda_{\gamma}(E2)$ for the $0_2^+ \rightarrow 0_1^+$ transitions of the ^{74,78}Ge isotopes. The $E2$ transition of reference is the transition to the 2_1^+ state. Both the experimental values obtained in this work and the results from literature are listed, with subscript *exp* and *lit*, respectively.

Nucleus	$I_i^\pi \rightarrow I_f^\pi$	$[\lambda_{\mathrm{ce,K}}(E2)/\lambda_{\gamma}(E2)]_{\mathrm{exp}}$	$[\lambda_{\mathrm{ce,K}}(E2)/\lambda_{\gamma}(E2)]_{\mathrm{lit}}$	Reference
^{74}Ge	$0_2^+ \rightarrow 0_1^+$	$<5.59 \times 10^{-3}$	$<5 \times 10^{-5}$	[89]
^{78}Ge	$0_2^+ \rightarrow 0_1^+$	$<2.19 \times 10^{-3}$	–	–

4.4 *E*0 Transition Strengths

Combining the results about internal conversion coefficients α_{K} and mixing ratio δ obtained in this work with information on lifetime values for the 2_2^+ states of ^{72,74,76,78}Ge reported in literature [40, 41, 42, 43], the $E0$ strength of $2_2^+ \rightarrow 2_1^+$ transitions of these isotopes has been determined. These results are presented in Table 4.8.

Upper limits on the $E0$ strengths of $0_2^+ \rightarrow 0_1^+$ transitions in ^{74,78}Ge have also been set. They can also be found in Table 4.8, together with previously known values, if available. In the case of ^{74}Ge, the upper limit determined in this work is less stringent that the one already present in literature. Therefore, the literature value will be adopted in the discussion which will follow in Section 4.6. Note that no new measurement has been

performed for the $\rho^2(E0; 0_2^+ \rightarrow 0_1^+)$ of ^{72}Ge. Indeed, in such a case, a direct application of Eq. (3.16) is used to determine $\rho^2(E0)$, since the only possible decay branch of the 0_2^+ state of ^{72}Ge is to the 0_1^+ ground state. Thus, the partial lifetime $\tau(E0)$ coincides with the total state lifetime τ. For this reason, only the lifetime τ of the 0_2^+ state and the atomic electron factor Ω are needed to determine the $E0$ strength, and further experimental information was not required.

Table 4.8: $E0$ transition strength measurements, ρ^2_{exp}, for the $2_2^+ \rightarrow 2_1^+$ and $0_2^+ \rightarrow 0_1^+$ transitions of ^{72,74,76,78}Ge. The half lives of the 2_2^+ and 0_2^+ states are reported in the third column and are taken from literature [40, 41, 42, 43]. Literature values of the $E0$ strength, ρ^2_{lit}, are taken from Ref. [44].

Nucleus	$I_i^\pi \rightarrow I_f^\pi$	$T_{1/2}(I_i^\pi)$	$\rho^2_{\text{exp}}(E0) \times 10^3$	$\rho^2_{\text{lit}}(E0) \times 10^3$
^{72}Ge	$2_2^+ \rightarrow 2_1^+$	4.5^{+8}_{-6} ps	100(50)	–
	$0_2^+ \rightarrow 0_1^+$	444.2(8) ns	–	8.3(4)
^{74}Ge	$2_2^+ \rightarrow 2_1^+$	5.4(8) ps	<0.22	–
	$0_2^+ \rightarrow 0_1^+$	$6\ ^{+15}_{-3}$ ps	<450	<5.3
^{76}Ge	$2_2^+ \rightarrow 2_1^+$	8.0(15) ps	<120	–
	$0_2^+ \rightarrow 0_1^+$	>0.8 ps	–	–
^{78}Ge	$2_2^+ \rightarrow 2_1^+$	12(6) ps	<6.5	–
	$0_2^+ \rightarrow 0_1^+$	25(11) ps	<120	–

4.5 γ-ray Decay Branching Ratios and Transition Probabilities

Exploiting the great sensitivity of the GRIFFIN spectrometer, it was possible to determine branching ratios for the γ-ray decay from the 0_2^+ state of ^{74,76,78}Ge, or to set a limit for them, by observing for the first time the $0_2^+ \rightarrow 2_2^+$ decay branch in ^{76,78}Ge. Such branching ratio measurements allowed to re-calculate $B(E2)$ reduced transition probabilities for the $0_2^+ \rightarrow 2_1^+$ transitions, but also to determine them for the first time in the case of the $0_2^+ \rightarrow 2_2^+$ transitions. The discussion that follows concerns only the isotopes ^{74,76,78}Ge, since in the case of ^{72}Ge the only possible decay of the 0_2^+ state (first excited state) is directly to the 0_1^+ ground state via an $E0$ transition.

Firstly, the branching ratio measurements are presented for each nucleus. Afterwards, the $B(E2)$ values are presented.

4.5.1 ^{74}Ge

In the γ-ray energy spectrum of ^{74}Ge, the $0_2^+ \rightarrow 2_2^+$ transition, expected at 278.6 keV, was not observed. A reduced level scheme of the ^{74}Ge nucleus is shown in Fig. 4.13, which shows the placement of the transitions of interest for the discussion. The GRIFFIN coincidence spectrum gated on the 715-keV, $2_3^+ \rightarrow 0_2^+$ transition shows only background counts in the region where the 279-keV peak would be expected. This gated spectrum can be seen in Fig. 4.12. In particular, the region of interest is shown in the inset. Gates were also set from below, in particular on the 608-keV, $2_2^+ \rightarrow 2_1^+$ and 1204-keV, $2_2^+ \rightarrow 0_1^+$

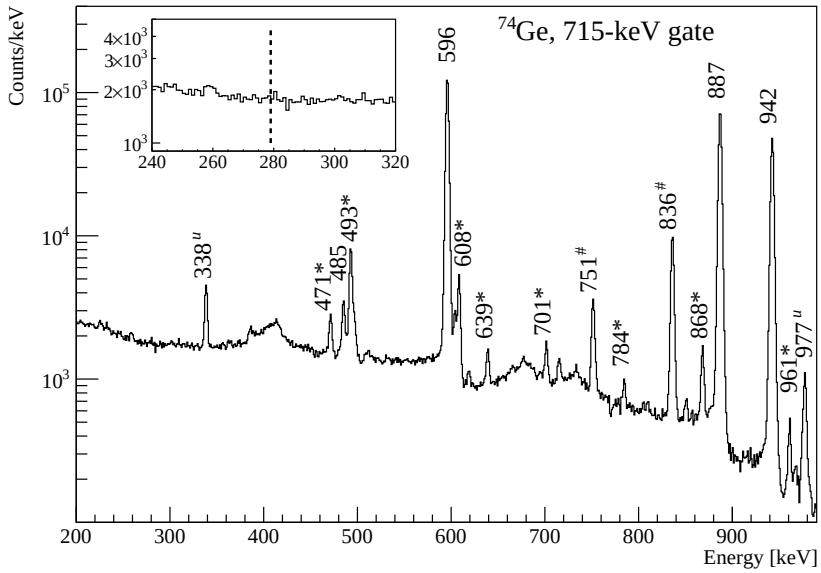

Figure 4.12: GRIFFIN coincidence energy spectrum for ^{74}Ge, gated on the 715-keV transition. Transitions are labeled with their energy value. Newly observed γ-rays which are in coincidence with the 715-keV, $2_3^+ \rightarrow 0_2^+$ line and have been placed in the level scheme are denoted by a #. The region where a 279-keV, $0_2^+ \rightarrow 2_2^+$ transition would be expected shows only background, as highlighted in the inset plot with the dashed line. A number of transitions, indicated with a star, are in coincidence with a γ-ray of $\approx$715 keV, previously unobserved, which could not be decoupled from the 715-keV, $2_3^+ \rightarrow 0_2^+$ line. The transitions indicated with a u were previously unknown and have not yet been placed in the level scheme.

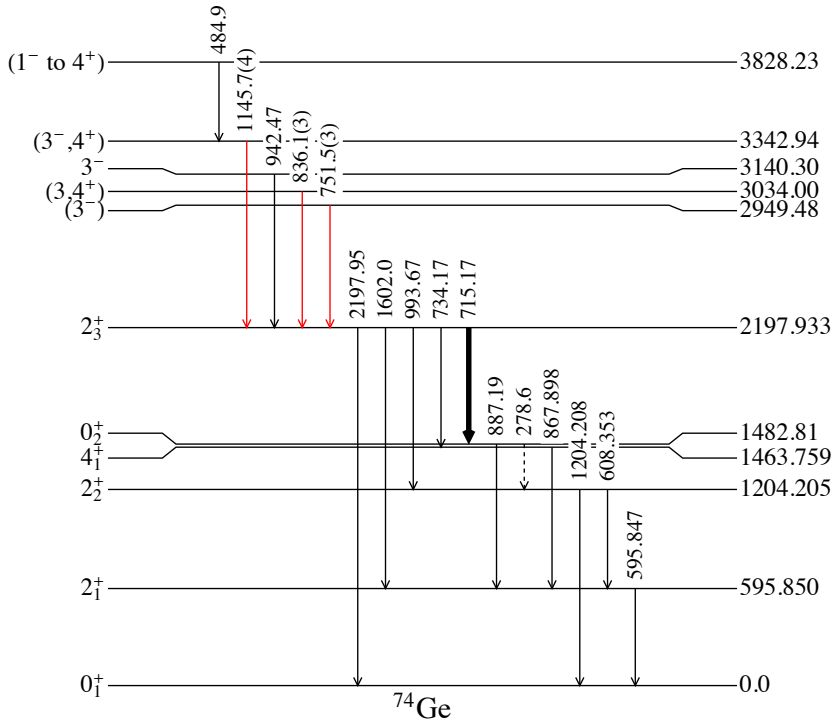

Figure 4.13: Partial level scheme for ^{74}Ge. Newly observed γ-ray transitions are marked in red, and both their measured energy and uncertainty are reported. Transition and state energy values are adopted from literature for the previoulsy known cases [41]. The 715-keV, $2_3^+ \rightarrow 0_2^+$ transition used as the gate in the branching ratio measurements for the 0_2^+ state is highlighted in bold. The $0_2^+ \rightarrow 2_2^+$ transition is dashed, to indicate that it has not been observed in the data. All the states have been included up to the 0_2^+ one; above it, only the states that show the transitions in cascade with the 715-keV, $2_3^+ \rightarrow 0_2^+$ line are shown, to be compared with the gated spectrum shown in Fig. 4.12.

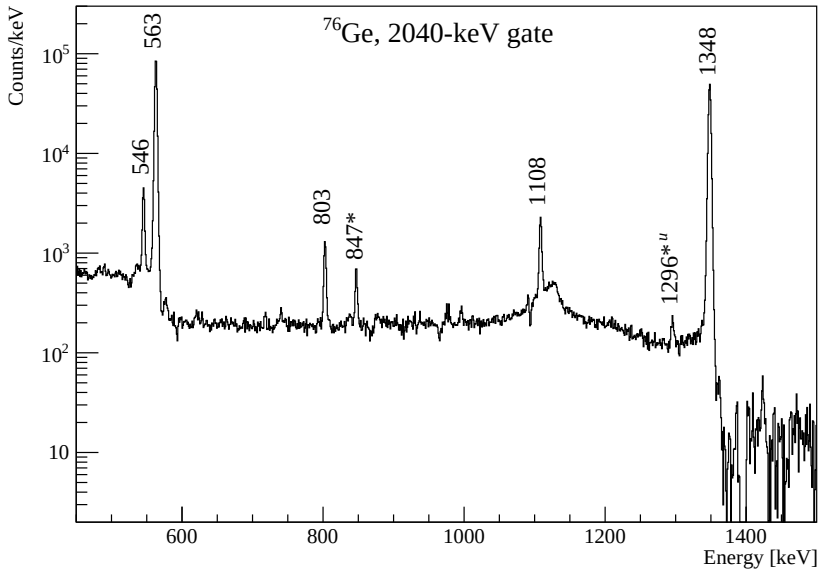

Figure 4.14: GRIFFIN coincidence energy spectrum for ^{76}Ge, gated on the 2040-keV transition. The transitions which are in coincidence with it are labeled with their energy value. Other transitions, marked with a star, are in coincidence with a γ-ray of 2037 keV, previously unobserved, which could not be completely separated from the 2040-keV line. The transition indicated with a u was previously unknown and has not yet been placed in the level scheme.

transitions, and even in these cases no transition was obvserved at 278.6 keV. Only an upper limit to the area of the $0_2^+ \rightarrow 2_2^+$ transition, and hence to its branching ratio, could be placed. In particular, the branching ratio results less than 0.03%.

4.5.2 ^{76}Ge

The $0_2^+ \rightarrow 2_2^+$ transition of 802.8(3) keV was observed for the first time in the ^{76}Ge γ-ray spectrum. This transition can be seen in the spectrum shown in Fig. 4.14, which is gated on the 2040-keV transition populating the 0_2^+ state. To calculate the branching ratios for the γ-ray decay branches from the 0_2^+ state, a gate from above could be applied, using three different transitions of 1008, and 1230 and 2040 keV, respectively. Note that the 1008.5(4) keV transition has been observed for the first time in this experiment, and is a new decay branch of the 2920-keV level. The transition of 1230 keV, instead, was previously observed only in (n,n'γ) experiments [40]. Figure 4.15 shows a reduced level scheme of ^{76}Ge, where the placement of the aforementioned transitions can be seen. Table 4.9 summarizes the measured branching ratio values obtained by setting the gates from above previously described. An average of such values has been adopted as the final value for the branching ratios. This is reported in the last column of Table 4.9.

The technique of gating from below could not be used in this case to establish the

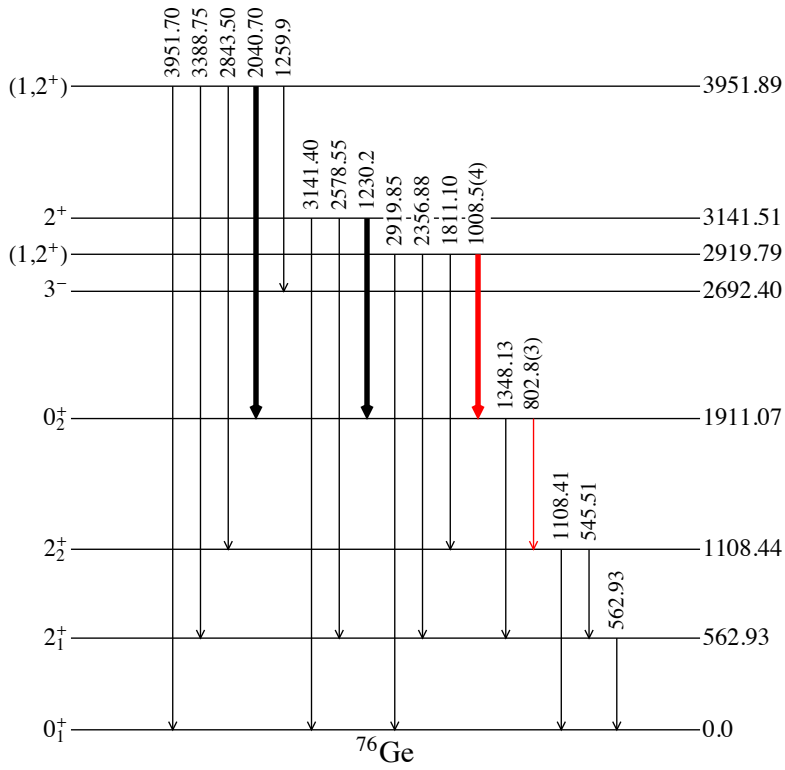

Figure 4.15: Partial level scheme for ^{76}Ge. Newly observed γ-ray transitions are marked in red, with both their measured energy and uncertainty reported. Transition and state energy values are reported from literature for the previoulsy known cases [40]. The transitions used as gates in the branching ratio measurements for the 0^+_2 state are highlighted in bold. All the states have been included up to the 2^+_2 one; above it, only the states relevant for the discussion are shown.

branching ratios from the 0_2^+ level, since the 802.8-keV transition is a doublet with the transition of 804.3(4) keV (observed here for the first time and not yet placed in the level scheme). The transitions of 546 and 563 keV that would have been used as gates from below are in coincidence with the 804-keV transition as well.

Table 4.9: Branching ratio (B.R.) measurements for the γ rays depopulating the 0_2^+ state of ^{76}Ge. Both the energy of the $I_i \rightarrow I_f$ γ-ray transitions and the energy of the gating transitions are reported, in the first and third column, respectively. All the measurements are performed gating from above. The last column shows the adopted average branching ratio values, B.R.$_{ave}$.

Transition Energy (keV)	$I_i \rightarrow I_f$	Gating Energy (keV)	B.R.	B.R.$_{ave}$
1348.13	$0_2^+ \rightarrow 2_1^+$	2040	98.41(3)%	98.45(4)%
		1230	98.47(10)%	
		1008	98.46(5)%	
802.8	$0_2^+ \rightarrow 2_2^+$	2040	1.59(3)%	1.55(4)%
		1230	1.53(10)%	
		1008	1.54(5)%	

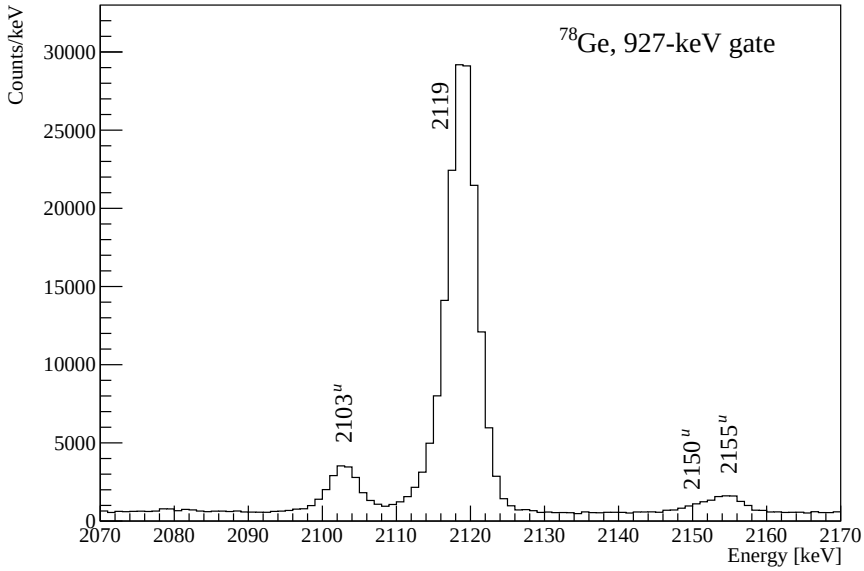

Figure 4.16: GRIFFIN coincidence energy spectrum for ^{78}Ge, gated on the 927-keV transition. Transitions are labeled with their energy value. The transitions indicated with a u are previously unknown and currently unplaced in the level scheme.

4.5.3 ^{78}Ge

The $0_2^+ \rightarrow 2_2^+$ transition of 360.1(2) keV was observed in the ^{78}Ge γ-ray energy spectrum. This can be seen in the GRIFFIN gated projections shown in Fig. 4.17, which are gated on the 2119-keV and 1186-keV transitions, respectively. A reduced level scheme of ^{78}Ge is shown in Fig. 4.18 for reference. Both the gating from above and below techniques were applied. The gate from above was set on the 2118.9(4) keV transition, observed here for the first time. This originates from the decay of a level at 3665.7(3) keV, which was previously unknown. In literature, a level at 3667(10) keV is reported, observed in a (t,p) reaction [43]. This level, though, cannot coincide with the one identified here, since its spin and parity is firmly assigned as 0^+. Therefore, a γ-ray transition from such a level to the 0_2^+ state would be forbidden, while in this work a 2119-keV transition to the 0_2^+ state is observed, and is used to perform the branching ratio measurement. Figure 4.16 shows the 2119-keV γ-ray peak in a coincidence projection gated on the 927-keV, $0_2^+ \rightarrow 2_1^+$ line. The observation of the level at 3665.7 keV has been confirmed by the observation of five other γ-ray decay branches, that are listed in Table 4.10 and shown in the level scheme in Fig. 4.18. Table 4.11 summarizes the measured branching ratio values. An average of such values has been adopted as the final value and is reported in the last column of Table 4.11.

Table 4.10: Summary of the γ-ray decay branches E_γ from the 3666-keV level identified in this work. No spin and parity I_i^π were assigned yet to this level. The energy values E_f of the final state are taken from literature [43]. For each γ-ray branch, the branching ratio (B.R.) measured in this work is also reported in the last column. This was obtained with the gating-from-below method. The γ-ray transitions used as a gate are indicated in the sixth column. As branching ratio B.R.$_{\gamma d}$ for the decaying transition of 927 keV, the value measured in this work and previously presented (see Table 4.11) has been used.

E_i (keV)	I_i^π	E_f (keV)	I_f^π	E_γ (keV)	Gating Energy (keV)	B.R.
3665.7(3)	–	2857.14	(2, 3, 4^+)	808.9(3)	1212	4.3(5)%
		2706.01	(2^+)	960.0(3)	2706	26(2)%
		1842.73	2^+	1823.0(4)	1223	19.4(7)%
		1546.6	0^+	2118.9(4)	927	9.3(3)%
		1186.51	2^+	2479.0(4)	1186	19(2)%
		619.36	2^+	3046.3(5)	619	21.3(7)%

4.5.4 Reduced Transition Probabilities

Since branching ratio measurements have been performed in this work for the γ-ray decay branches which depopulate the 0_2^+ state of ^{74,76,78}Ge, it was possible to determine $B(E2)$ reduced transition probability values previously absent in literature. Such results are summarized in Table 4.12. Half life values from literature have been adopted for the 0_2^+ states. It is to note that, in the case of ^{74,76}Ge, such values have been determined starting from $B(E2; 0_2^+ \rightarrow 2_1^+)$ values measured via Coulomb excitation measurements.

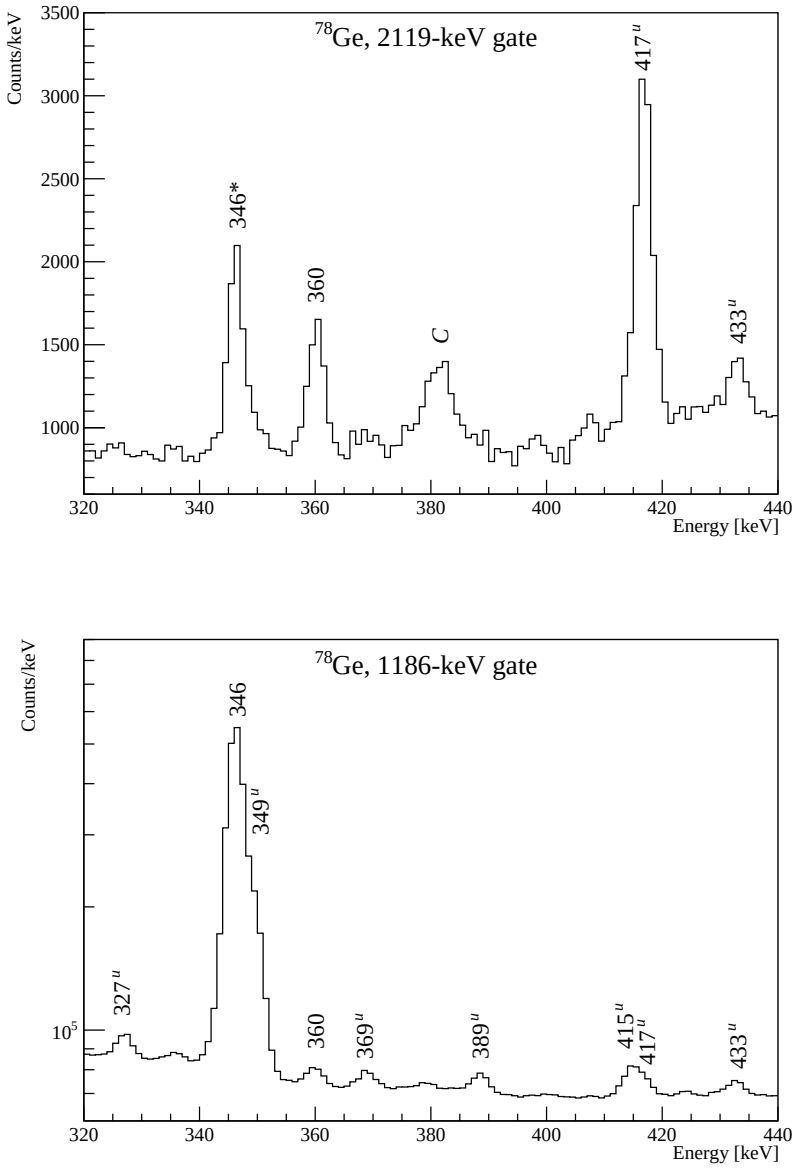

Figure 4.17: GRIFFIN coincidence energy spectrum for ^{78}Ge, gated on the 2119-keV and the 1186-keV transitions in the top and bottom panel, respectively. Note that the top spectrum is shown in linear scale, while the bottom one is in logarithmic scale. Transitions are labeled with their energy value. The transitions indicated with a u are previously unknown and currently unplaced in the level scheme. The letter C denotes a Compton diagonal component that could not be succesfully removed in the 2119-keV gated projection, despite applying a Compton-background subtraction. The 346-keV known transition which appears in the 2119-keV gated projection and is marked with a star cannot be in coincidence with the 2119-keV transition to the 0_2^+ state. This points to the fact that the 2119-keV line is a doublet, which could not be resolved.

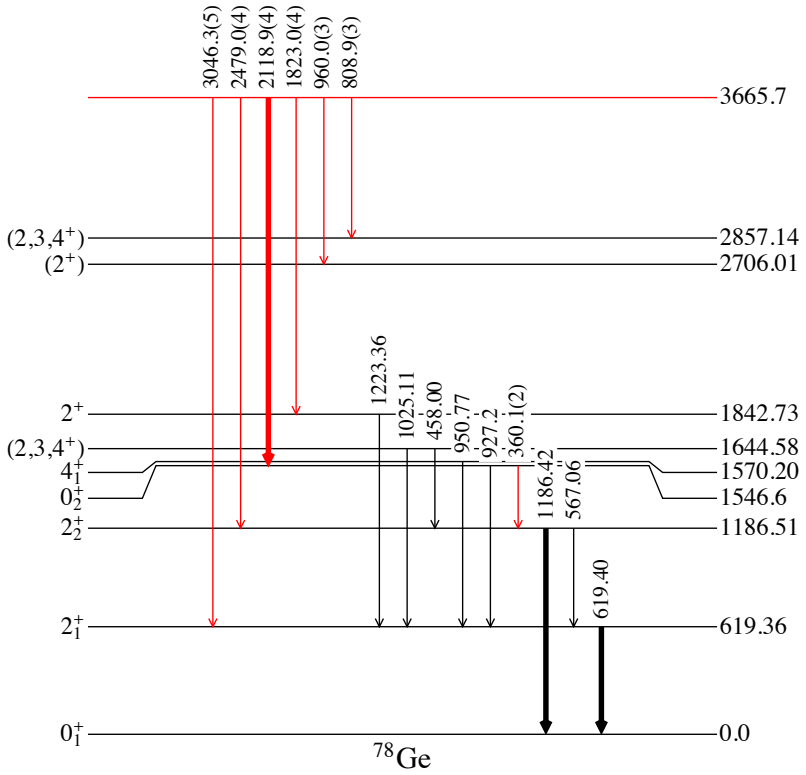

Figure 4.18: Partial level scheme for ^{78}Ge. Newly observed γ-ray transitions are marked in red, and both their measured energy and uncertainty are reported. Transition and state energy values are reported from literature for the previoulsy known cases [43]. The state at 3665.7(3) keV has been identified in this work for the first time; it is marked in red. The transitions used as gates in the branching ratio measurements for the 0^+_2 state are highlighted in bold. All excited states are shown up to 1.8 MeV, with their decaying transitions. Above this, only the states that are relevant to show the newly observed decay-branches from the 3666-keV level are included.

Table 4.11: Branching ratio (B.R.) measurements for the γ rays depopulating the 0_2^+ state of ^{78}Ge. Both the energy of the $I_i \rightarrow I_f$ γ-ray transitions and the energy of the gating transitions are reported, in the first and third column, respectively. A superscript to the gating energy indicates if the measurement was performed setting a gate from above or below. The last column shows the adopted average branching ratio values, B.R.$_{\text{ave}}$.

Transition Energy (keV)	$I_i \rightarrow I_f$	Gating Energy (keV)	B.R.	B.R.$_{\text{ave}}$
927.2(3)	$0_2^+ \rightarrow 2_1^+$	2119^{above} 619^{below}	98.29(14)% 98.33(12)%	98.31(9)%
360.1(2)	$0_2^+ \rightarrow 2_2^+$	2119^{above} 1186^{below}	1.71(14)% 1.67(12)%	1.69(9)%

Therefore, in the case of ^{76}Ge where the second γ-ray branch, $0_2^+ \rightarrow 2_2^+$, was previously unknown, the obtained half life (>0.9 ps) is a *partial* half life, under the simplest assumption that the Coulex analysis is not biased by an incomplete knowledge of the decay pathways of the considered state. Here, it was possible to determine the total half life, knowing the branching ratios of the two γ-ray transitions and using the relationship in Eq. (1.20). The limit, though, results unchanged, since the $0_2^+ \rightarrow 2_1^+$ branch is dominant relative to the other one [98.45(11)% and 1.55(11)%, see Table 4.9].

Table 4.12: $B(E2)$ reduced transition probabilities for the $0_2^+ \rightarrow 2_1^+$ and $0_2^+ \rightarrow 2_2^+$ γ-ray branches which depopulate the 0_2^+ state of ^{74,76,78}Ge. As discussed in Section 4.5, only the $0_2^+ \rightarrow 2_1^+$ branch has been observed for ^{74}Ge, therefore only the $B(E2)$ value of this branch is reported. The half life values are taken from literature and have been obtained either through Coulomb excitation measurements [hence, from the measured $B(E2; 0_2^+ \rightarrow 2_1^+)$ values] or from direct lifetime measurements via $\beta\gamma\gamma(t)$ fast timing, as indicated in the third column. References for such values are provided, either in correspondence of the $T_{1/2}$ or the $B(E2)$ measured value. The $B(E2)$ values have been calculated in this work for the first time, unless otherwise noted.

Nucleus	$T_{1/2}$ (ps)	Technique	$B(E2; 0_2^+ \rightarrow 2_1^+)$ (W.u.)	$B(E2; 0_2^+ \rightarrow 2_2^+)$ (W.u.)
^{74}Ge	$6\ ^{+15}_{-3}$	Coulex	$9\ ^{+9}_{-6}$ [41]	–
^{76}Ge	>0.9	Coulex	<7.4 [90]	<1.5
^{78}Ge	25(11) [91]	$\beta\gamma\gamma(t)$	1.6(7)	3.2(15)

4.6 Discussion

The $E0$ strength of $I_i^\pi \rightarrow I_f^\pi$, $I_i = I_f$ transitions with $I = 2$ in ^{72,74,76,78}Ge have been experimentally investigated in this work. Limits have been set, when possible, also in the $I = 0$ case. The results of this analysis have been summarized in Table 4.8.

A finite $\rho^2(E0; 2_2^+ \rightarrow 2_1^+)$ value, 100(50) milliunits, has been found for ^{72}Ge. This indicates that the 2^+ states belonging to the ground-state and γ bands (nominally with

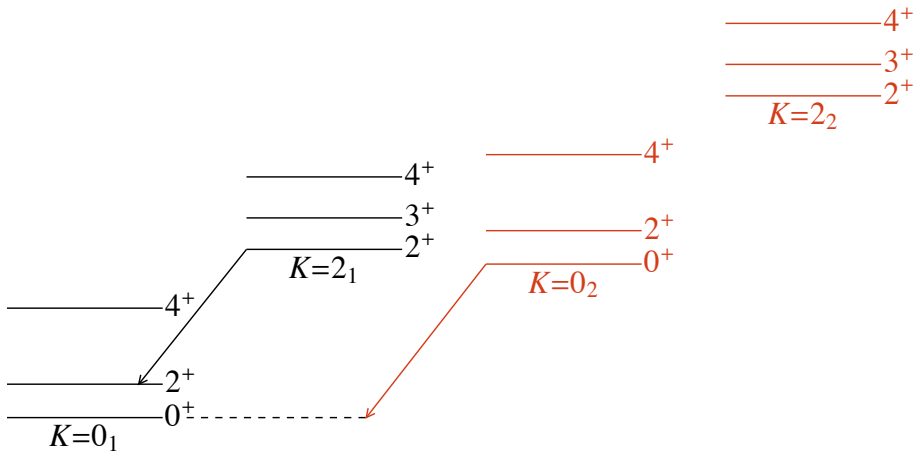

Figure 4.19: Sketch of rotational bands with $K = 0$ and $K = 2$, respectively (not to scale). Values of K correspond to those of unmixed states, in which K is a good quantum number. The states drawn in black belong to the 0_1^+ configuration, while the red ones belong to the 0_2^+ configuration. The black arrow indicates the $2_2^+ \rightarrow 2_1^+$ transition, and the red arrow indicates the $0_2^+ \rightarrow 0_1^+$ one.

$K = 0$ and $K = 2$, respectively, and represented by the states in black in Fig. 4.19) cannot have pure wave functions and must be mixed to some degree. This is consistent with previous results, in particular those published by Ayangeakaa *et al.* [3], where evidence of coexistence involving two triaxial configurations has been found. In the aforementioned publication, as previously discussed in Section 1.6, calculations were performed within the shape-coexisting generalized triaxial rotor model (GTRM×2) [49]. These calculations have been found to reproduce $E2$ matrix elements of ^{72}Ge more successfully than the generalized triaxial rotor model (GTRM) [92, 93]. This result supported the description of the 0_1^+ and 0_2^+ states in terms of coexistence of two triaxially deformed configurations. In the GTRM, a mixing of the ground-state and γ bands ($K = 0_1$ and $K = 2_1$, respectively) is allowed. Such K-mixing is a result of the triaxiality of the considered configuration. Therefore, in contrast to the axially symmetric rotor model case (see Section 1.1.2), where the ground state and γ bands are distinct, here mixing occurs between those two. The relevant components playing a role in such a case are represented by the states in black in the sketch shown in Fig. 4.19. In GTRM×2, a coupling of two such triaxial rotors is considered. The second triaxial rotor configuration is represented by the states in red in Fig. 4.19. Such coupling can result in $K = 0$ and $K = 2$ components in the wave function of a 2^+ state from multiple configurations. For ^{72}Ge, the GTRM×2 calculations yielded the following wave functions for the first and second

2^+ excited states [94]:

$$\left|2_1^+\right\rangle = 0.67\,|2, K=0_1\rangle + 0.287\,|2, K=2_1\rangle + 0.593\,|2, K=0_2\rangle + 0.342\,|2, K=2_2\rangle \quad (4.4)$$

$$\left|2_2^+\right\rangle = -0.368\,|2, K=0_1\rangle + 0.858\,|2, K=2_1\rangle - 0.18\,|2, K=0_2\rangle + 0.312\,|2, K=2_2\rangle \quad (4.5)$$

where each component of the wave functions is given as $|IK\rangle$, with I total angular momentum of the system and K projection of the total angular momentum onto the symmetry axis in the intrinsic reference system, according to the notation introduced in Section 1.1.2. In such wave functions, an overlap of $\Delta K = 0$ components is found, which can generate the observed $E0$ strength. This is the result of mixing of the configurations associated with the 0_1^+ and 0_2^+ states, and not simply of the K-mixing of 2^+ states within a single configuration as per the single triaxial rotor model (GTRM). Hence, the $E0$ strength of the $2_2^+ \rightarrow 2_1^+$ transition may be taken as an indirect measure or probe of the mixing between the two configurations.

The value of $\rho^2(E0; 0_2^+ \rightarrow 0_1^+)$ in ^{72}Ge was already known in literature and reported to be equal to 8.3(4) milliunits [44]. Such a value is not among the largest known, which reach hundreds of milliunits (see, for reference, the most recent compilation of $E0$ strength values published by Kibédi and Spear [77]). In Section 1.4, the relationship $\rho(E0) \simeq \alpha\beta\Delta\langle r^2\rangle$ was derived [see Eq. (1.33)], that points to large $E0$ strength occurrance in case of strong mixing, within a simple two-state mixing model. This was based in the assumption that the states involved in the mixing were associated with very different mean square charge radii. If such an assumption is relaxed, though, the aforementioned relationship could not hold anymore. In ^{72}Ge, the $0_2^+ \rightarrow 0_1^+$ transition connects the bandheads belonging to two different configurations, while the $2_2^+ \rightarrow 2_1^+$ transition occurs between states built on the same intrinsic configuration. These transitions are represented by the black arrow and the red arrow in Fig. 4.19, respectively. Given the different nature of such transitions, a similarity in their $E0$ strength is not necessarily expected. An effective theoretical understanding of the emergence of $E0$ strength in states with $I > 0$ is still lacking, and improvements are required also in the predictions for the $I = 0$ cases.

For the higher mass isotopes ^{74,78}Ge, stringent upper limits have been set on $\rho^2(E0; 2_2^+ \rightarrow 2_1^+)$ (<0.22 and <6.5 milliunits, respectively), pointing to near zero $E0$ strength in such cases. The conclusions previously drawn from transfer reaction data indicate weak mixing for the even-even Ge isotopes with $N > 40$, as summarized in the review by Heyde and Wood [1]. For ^{76}Ge, an upper limit of $\rho^2(E0; 2_2^+ \rightarrow 2_1^+) < 120$ milliunits has been determined. This limit is still broad and must be refined in order to provide more sensitive information on the presence of an $E0$ component for the $2_2^+ \rightarrow 2_1^+$ transition of ^{76}Ge. Broad upper limits have been set in this work also on the $\rho^2(E0; 0_2^+ \rightarrow 0_1^+)$ of ^{74,78}Ge. Despite not being in contrast with the weak mixing description where no $E0$ strength is expected, they also do not provide stringent results to support it. In the case of ^{74}Ge, a smaller upper limit was already reported in literature (<5.3 milliunits [44]), which points to near zero $E0$ strength. Further experimental effort is required to measure the $E0$ strength for the $0_2^+ \rightarrow 0_1^+$ transition of ^{76,78}Ge. Note that even the nuclei

^{74,76,78}Ge, as well as ^{72}Ge, are expected to present triaxial ground state configurations, on the basis of theoretical calculations [52], an analysis of the energy staggering parameter $S(I)$ introduced in Eq. (1.5) [51, 52], and Coulomb excitation experiment results [4]. Therefore, multiple K components could emerge in the first and second 2^+ excited states as a result of triaxiality. Nonetheless, in the cases of ^{74,78}Ge where weak mixing is indicated between the 0^+ configurations, near zero $E0$ strength is observed in the $2_2^+ \rightarrow 2_1^+$ transition, which points to the fact that both triaxiality and configuration mixing are necessary for a large $E0$ strength to arise between $I > 0$ states belonging to the same configuration.

A two-state mixing description has been proposed by Fortune as a more general, simpler description of the configuration mixing in ^{72}Ge relative to the GTRM$\times$2 calculations, since it does not require the assumption of shape coexistence among predetermined shapes [95]. From an analysis of the recently measured $m(E2)$ matrix elements by Ayangeakaa *et al.* [3] and allowing mixing between the 0_1^+ and 0_2^+ states and the 2_1^+ and 2_3^+ states, Fortune's analysis points to the 0^+ configurations being maximally mixed. Note that the mixing between the first and third 2^+ states assumed by Fortune (instead of mixing between the first and second 2^+ states, belonging to the ground-state and γ bands) is consistent with the results of the GTRM$\times$2 calculations, which better describe the matrix elements compared to the GTRM, where only the first and second 2^+ states ($K = 0_1$ and $K = 2_1$) can mix. The model used by Fortune, though, does not require that the mixed configurations are triaxial. Anyway, Coulomb excitation data bring evidence of triaxiality for the observed 0_1^+ and 0_2^+ states of ^{72}Ge [3].

A similar analysis cannot be performed yet in the case of the neighbouring isotopes, ^{74,76,78}Ge, for which weak mixing would be expected, according to the results from transfer data discussed in Section 1.6. This is momentarily prevented from a lack of experimental data on the third 2^+ state of these isotopes and its associated properties, such as $B(E2)$ reduced transition probabilities and lifetimes.

In conclusion, the $E0$ strength of the $2_2^+ \rightarrow 2_1^+$ transition of ^{72,74,76,78}Ge have been measured, and upper limits have been set for the $0_2^+ \rightarrow 0_1^+$ transition of ^{74,78}Ge. These results support the interpretation of the structure of Ge isotopes from previous works, which points to strong mixing between deformed configurations in ^{72}Ge and to a lessening of such mixing in the neighbouring isotopes, where the excited 0^+ states move higher in energy. They indicate that both triaxiality and configuration mixing are elements needed for a large $E0$ strength to occur between $I > 0$ states within the same configuration. Further studies, both on the theoretical and experimental sides, will be required to shed light on the origin of $E0$ strengths in atomic nuclei.

5

CONCLUSIONS

In this thesis, an experimental investigation of mixing between different configurations in even-even Ge isotopes with mass $A = 72, 74, 76, 78$ has been presented. The measurement of $E0$ strength has been used as a means to probe such mixing. The focus has been set on the $2_2^+ \rightarrow 2_1^+$ transition of each of those isotopes. Upper limits on the $E0$ strength of the $0_2^+ \rightarrow 0_1^+$ transitions of ^{74,78}Ge have also been set.

Two β-decay experiments have been carried out at the TRIUMF laboratory, in 2017 and 2019, to populate and study the nuclei of interest. High-intensity radioactive ion beams of ^{72,74,76,78}Ga ($\sim 10^{4-6}$ pps) were delivered to the GRIFFIN decay station in the ISAC facility and ultra-high-statistics datasets were collected. Details on the experiments and on the employed setups have been given in Chapter 2 of this thesis.

Internal conversion coefficient (α_{K}) measurements have been performed, exploiting the data collected by both the PACES and GRIFFIN arrays for conversion electrons and γ-rays, respectively. Moreover, an analysis of $\gamma\gamma$ angular correlations of γ-ray transitions has been carried out, to measure the $E2/M1$ mixing ratio (δ) of the $2_2^+ \rightarrow 2_1^+$ transitions of ^{72,74,76,78}Ge. A new δ value has been measured in ^{78}Ge, while previously known values for the other isotopes were re-measured with much higher precision (the uncertainty was reduced by a factor $\sim$10), thanks to the high-statistics provided by the dataset used for this analysis and the large number of angular bins available with the GRIFFIN spectrometer (up to 51), and hence the large number of experimental data points in the correlations. The high-efficiency of the GRIFFIN spectrometer, again combined with the high statistics collected, also allowed the observation for the first time of γ-ray branches from the first excited 0^+ state of ^{76,78}Ge to the second 2^+ state. The techniques used to perform such analyses have been discussed in Chapter 3, while Chapter 4 contains the presentation of all the experimental results.

By combining the measured α_{K} and δ values with literature lifetime τ of the 2_2^+ state, the $E0$ strength of the $2_2^+ \rightarrow 2_1^+$ transitions of ^{72,74,76,78}Ge has been determined. A finite value of 100(50) milliunits has been found in the case of ^{72}Ge. This implies the

presence of different K components in the wave functions of the 2_1^+ and 2_2^+ states, so that $\Delta K = 0$ transitions are allowed and $E0$ strength can emerge. This is consistent with the interpretation drawn from GTRM$\times$2 calculations [49], according to which the matrix elements of ^{72}Ge recently measured by Ayangeakaa *et al.* [3] can be effectively described considering mixing between two triaxial 0^+ configurations. This results in the presence of multiple K components in the 2_1^+ and 2_2^+ states, as illustrated by Eqs. (4.4) and (4.5) [94]. In the neighbouring nuclei, ^{74,78}Ge, for which weak mixing is expected, near zero $E0$ strength has been found in the $2_2^+ \rightarrow 2_1^+$ transitions ($<$0.22 milliunits in ^{74}Ge and $<$6.5 milliunits in ^{78}Ge). In the case of ^{76}Ge, only a broad upper limit could be set [$\rho^2(E0; 2_2^+ \rightarrow 2_1^+) < 120$ milliunits]. Therefore, further experimental studies are needed to refine such measurement. The observation of near zero $E0$ strength in the $2_2^+ \rightarrow 2_1^+$ transitions of even-even Ge nuclei with $N > 40$, in contrast to the large value determined for ^{72}Ge, points to the fact that both shape mixing and triaxiality are necessary ingredients for a large $E0$ strength to manifest in $I > 0$ transitions within the same configuration.

In conclusion, the experimental investigation presented here is consistent with the description of the structure of even-even Ge isotopes around $N = 40$ drawn from previous works, according to which strong mixing occurs in the ^{72}Ge nucleus between the 0_1^+ and 0_2^+ states, while only weak mixing is presented between such states in the neighbouring isotopes. The measurements presented in this thesis, which for the first time investigate the $E0$ strength of $2_2^+ \rightarrow 2_1^+$ transitions in Ge isotopes, reinforce such a description, providing a new probe of their structure. A comprehensive theoretical description of the $E0$ strength, though, is still lacking, and further effort is required to address it, complemented by experimental studies that expand our knowledge of $E0$ strengths both in Ge nuclei and across the nuclear chart.

Appendices

A

RADIOACTIVE-ION BEAM INTENSITY CALCULATION

This appendix aims at summarizing the procedure to calculate the beam intensity of a radioactive-ion beam delivered at GRIFFIN.

GRIFFIN uses a moving tape collector system which can be operated in cycle mode, as described in Section 2.2.1. To properly calculate the beam intensity of a nucleus ^{A}X delivered at the center of the array and β-decaying into the daugther nucleus ^{A}Y, it is necessary taking into account the applied cycle times. In the following, we will refer to the cycle fraction in which data are collected while the beam is implanted on the tape as *beam-on time*, while we will define *beam-off time* the cycle part in which data are collected without beam being delivered to GRIFFIN.

The radioactive decay law [25] with the addition of a source term is used to perform this calculation. During beam-on time, it holds:

$$\frac{dN}{dt} = -\lambda N + R \tag{A.1}$$

with N number of ^{A}X nuclei present at the center of the array at a certain time t, λ decay constant of the nucleus ^{A}X, λN decay rate and R beam rate. The solution of this equation, with boundary condition $N(t=0) = N_0$ initial number of particle, is:

$$N(t) = N_0 e^{-\lambda t} + \frac{R}{\lambda}\left(1 - e^{-\lambda t}\right) \tag{A.2}$$

In the case here considered, at $t = 0$ there are no particles at the implantation point, since all the previously deposited activity has been removed from the center of the array via the moving tape collector. Therefore, the first term of the equation is null.

To calculate the total number of ^{A}X nuclei delivered during the beam-on time (from

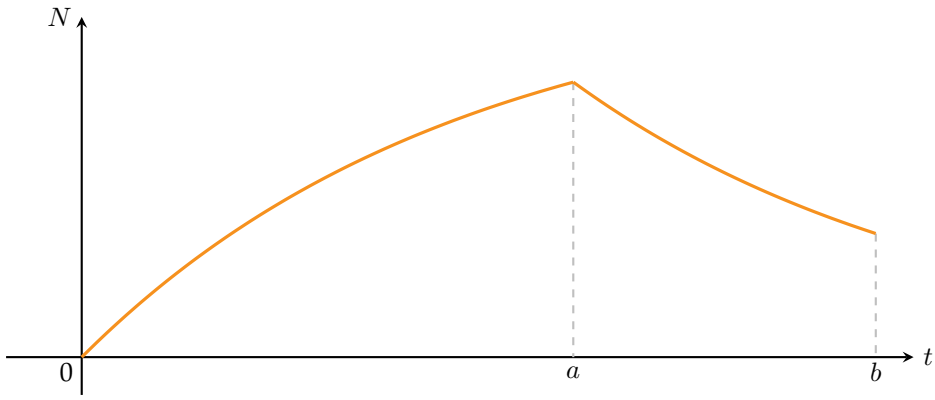

Figure A.1: Example of cycle with beam on from $t = 0$ to $t = a$ and beam off from $t = a$ to $t = b$. The curve represents the number of particle N at the implantation point at a certain time t.

$t = 0$ to $t = a$, see Fig. A.1), we need to integrate the positive term in Eq. (A.1):

$$N_{\text{del}} = \int_0^a R\,dt = Ra \tag{A.3}$$

and to calculate the number of those decayed we need to integrate the negative term in Eq. (A.1), with $N = N(t) = R(1 - e^{-\lambda t})/\lambda$:

$$N_{\text{dec. Beam-On}} = \int_0^a R\,dt - \int_0^a Re^{-\lambda t}\,dt = Rt\Big|_0^a - R\left(-\frac{e^{-\lambda t}}{\lambda}\right)\Big|_0^a = Ra - R\left(\frac{1 - e^{-\lambda a}}{\lambda}\right) \tag{A.4}$$

During beam-off time, the source term present in Eq. (A.1) is dropped:

$$\frac{dN}{dt} = -\lambda N \tag{A.5}$$

The solution of this equation is:

$$N(t') = N_0 e^{-\lambda t'} \tag{A.6}$$

with $t' = t - a$. In this case, the initial number of particle N_0 is the number of particles at time $t' = 0$ ($t = a$), which we find subtracting Eq. (A.4) from Eq. (A.3):

$$N_0 = R\left(\frac{1 - e^{-\lambda a}}{\lambda}\right) \tag{A.7}$$

The number of nuclei decayed during beam-off time is:

$$N_{\text{dec. Beam-Off}} = N_0 - N|_{t'=b-a} = \tag{A.8}$$

$$= N_0 - N_0 e^{-\lambda(b-a)} = \tag{A.9}$$

$$= R\left(\frac{1-e^{-\lambda a}}{\lambda}\right)\left(1-e^{-\lambda(b-a)}\right) \tag{A.10}$$

The total number of β decays observed in a cycle is then obtained summing Eqs. (A.4) and (A.10):

$$N_{\text{dec}} = Ra - R\left(\frac{1-e^{-\lambda a}}{\lambda}\right) + R\left(\frac{1-e^{-\lambda a}}{\lambda}\right)\left(1-e^{-\lambda(b-a)}\right) \tag{A.11}$$

$$= Ra - \frac{R}{\lambda}e^{-\lambda a}e^{-\lambda(b-a)} \tag{A.12}$$

After these considerations, it is possible to obtain the beam intensity through a γ-ray intensity measurement. Indeed, the number of γ-ray decays of the daughter nucleus ^{A}Y observed in a cycle (corrected for the γ-ray intensity and the γ-ray efficiency) is also equal to the number of β decays which happened during one cycle. This leads to:

$$N_{\text{dec}} = \frac{A_\gamma \times \Delta T_{\text{cyc}}}{I_\gamma \epsilon_\gamma \times \Delta T} \tag{A.13}$$

where A_γ is the number of counts of a γ-ray in the set of data collected, I_γ is its intensity in the β decay, ϵ_γ is the GRIFFIN array efficiency at the energy of the considered γ ray, ΔT_{cyc} is the duration of one tape cycle and ΔT the duration of the data collection.

Finally, from Eqs. (A.11) and (A.13) it is possible to calculate the beam intensity delivered to GRIFFIN:

$$R = \frac{A_\gamma \times \Delta T_{\text{cyc}}}{I_\gamma \epsilon_\gamma \times \Delta T \times \left\{a - \frac{e^{-\lambda a}e^{-\lambda(b-a)}}{\lambda}\right\}} \tag{A.14}$$

B

ANGULAR CORRELATION ANALYSIS: ADDITIONAL PLOTS

In this appendix, plots relevant for the $\gamma\gamma$ angular correlation analysis discussed in Section 4.1 are presented. In particular, Fig. B.1 shows the correlation of the $4_1^+ \rightarrow 2_1^+ \rightarrow 0_1^+$ cascade of ^{72}Ge. Figures B.2 and B.3 show the correlations of the $4_1^+ \rightarrow 2_1^+ \rightarrow 0_1^+$ and $0_2^+ \rightarrow 2_1^+ \rightarrow 0_1^+$ cascades of ^{74}Ge, respectively. Finally, the correlations of the $4_1^+ \rightarrow 2_1^+ \rightarrow 0_1^+$ and $0_2^+ \rightarrow 2_1^+ \rightarrow 0_1^+$ cascades of ^{76}Ge are presented in Figs. B.2 and B.3.

In all the plots, the experimental angular correlation points and uncertainties are presented in the top panel, with black dots and error bars. The best-fit curve $Z_{\text{sum}}(\theta)$, defined in Eq. (3.13), of the simulated distributions to the data is represented by the red curve. The thickness of the curve indicates the statistical uncertainty on the simulations. The fits were performed using A_{00} as the only free parameter, with the requirement that $\delta_1 = \delta_2 = 0$, since the transitions considered are stretched $E2$. The bottom panel shows the residuals of the datapoints relative to the fitted curve; here, the error bars include both the experiment and simulations uncertainties, added in quadrature.

The reduced χ^2 calculated for $\nu = 49 - 1 = 48$ degrees of freedom ($N = 49$ data points and one free parameter in the fit, A_{00}) is also shown in the plot. The results of the fits were already summarized in Table 4.2.

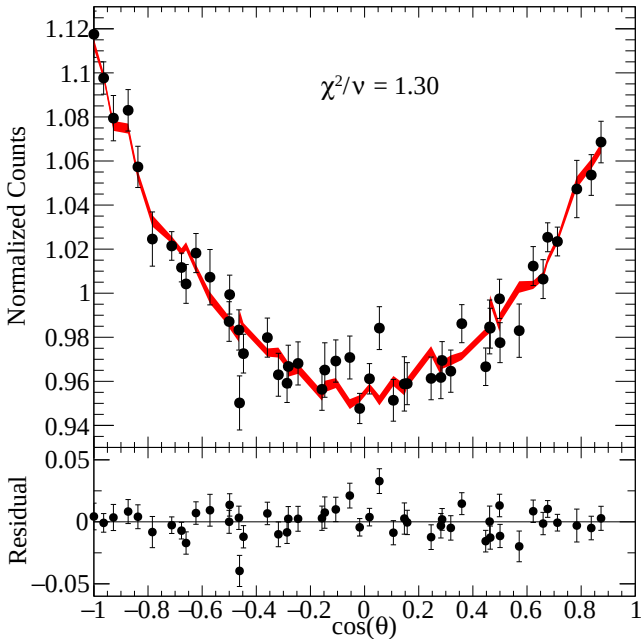

Figure B.1: Experimental angular correlation of the $4_1^+ \rightarrow 2_1^+ \rightarrow 0_1^+$ 894-834 keV γ-ray cascade of ^{72}Ge. Data are fitted to the simulated $Z_i(\theta)$ distributions using A_{00} as the only free parameter, fixing $\delta_1 = \delta_2 = 0$.

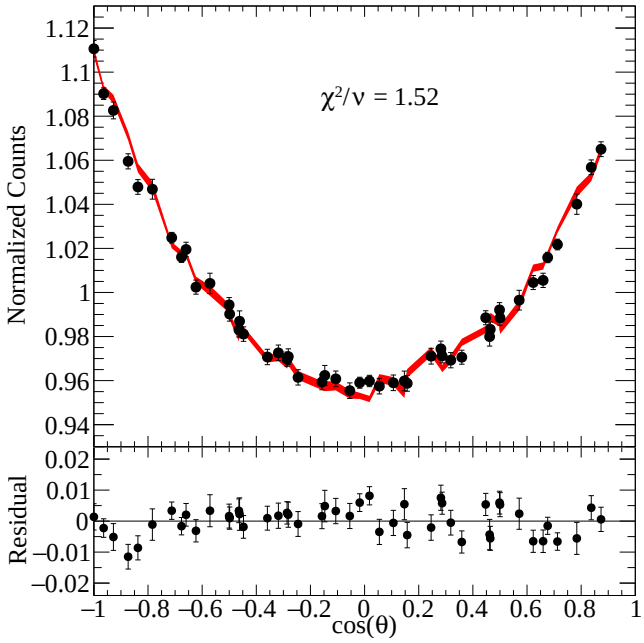

Figure B.2: Experimental angular correlation of the $4_1^+ \rightarrow 2_1^+ \rightarrow 0_1^+$ 868-596 keV γ-ray cascade of ^{74}Ge. Data are fitted to the simulated $Z_i(\theta)$ distributions using A_{00} as the only free parameter, fixing $\delta_1 = \delta_2 = 0$.

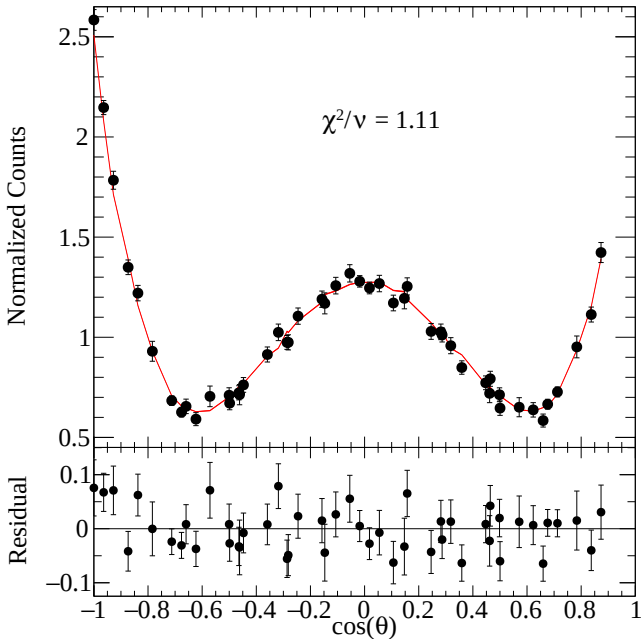

Figure B.3: Experimental angular correlation of the $0_2^+ \rightarrow 2_1^+ \rightarrow 0_1^+$ 887-596 keV γ-ray cascade of ^{74}Ge. Data are fitted to the simulated $Z_i(\theta)$ distributions using A_{00} as the only free parameter, fixing $\delta_1 = \delta_2 = 0$.

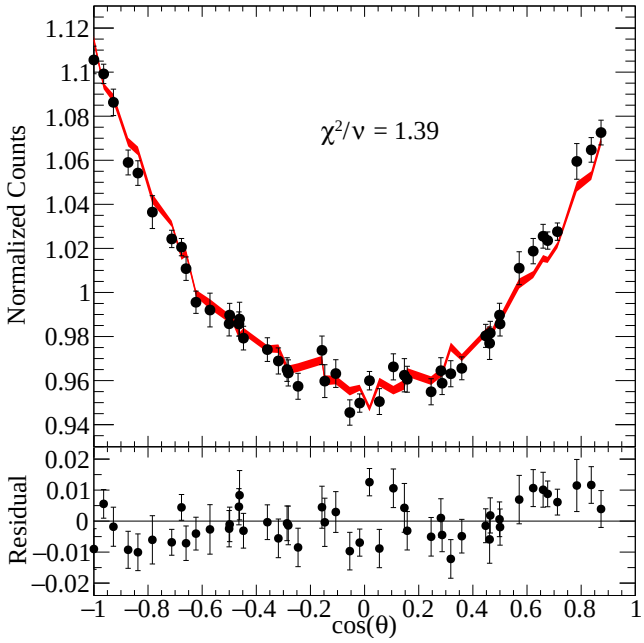

Figure B.4: Experimental angular correlation of the $4_1^+ \rightarrow 2_1^+ \rightarrow 0_1^+$ 847-563 keV γ-ray cascade of ^{76}Ge. Data are fitted to the simulated $Z_i(\theta)$ distributions using A_{00} as the only free parameter, fixing $\delta_1 = \delta_2 = 0$.

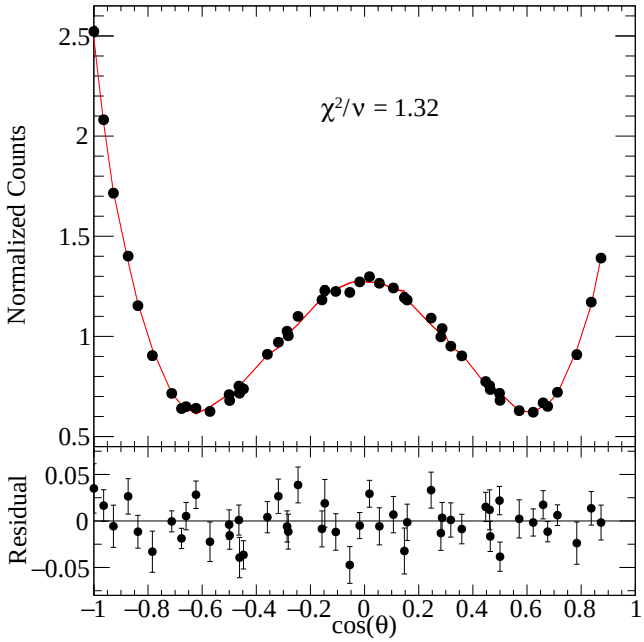

Figure B.5: Experimental angular correlation of the $0_2^+ \rightarrow 2_1^+ \rightarrow 0_1^+$ 1348-563 keV γ-ray cascade of ^{76}Ge. Data are fitted to the simulated $Z_i(\theta)$ distributions using A_{00} as the only free parameter, fixing $\delta_1 = \delta_2 = 0$.

C

ANGULAR CORRELATION ANALYSIS: COVARIANCE MATRICES

In this Appendix, the covariance matrices obtained from the linear fit of the angular correlations discussed in Section 4.1.2 are presented. The linear fit has been performed using a_2 and a_4 as free parameters, together with the scaling factor A_{00} (see Section 3.4.1 for a description of the analysis technique). Since only the correlation between the a_2 and a_4 parameters is of interest, only the relevant matrix elements will be presented in the following. Note that the uncertainty on the a_2^{exp} and a_4^{exp} parameters reported in Table 4.3 has been inflated by $\sqrt{\chi^2/\nu}$, where the number of degrees of freedom is $\nu = 46$, since each correlations has $N = 49$ data points and there are three free parameters in the fit.

The covariance matrices C are presented in the form:

$$C = \begin{bmatrix} \text{var}(a_2) & \text{cov}(a_2, a_4) \\ \text{cov}(a_2, a_4) & \text{var}(a_4) \end{bmatrix} \tag{C.1}$$

where $\text{var}(a_i)$ is the variance of a_i and $\text{cov}(a_2, a_4)$ is the covariance between a_2 and a_4. The covariance matrices are listed in Table C.1 for each of the considered $2_2^+ \xrightarrow{\gamma_1} 2_1^+ \xrightarrow{\gamma_2} 0_1^+$ γ-ray cascades in the ^{72,74,76,78}Ge nuclei.

Table C.1: Results of the linear fit of the angular correlations for the $2_2^+ \xrightarrow{\gamma_1} 2_1^+ \xrightarrow{\gamma_2} 0_1^+$ γ-ray cascades of the ^{72,74,76,78}Ge nuclei. The γ-ray energies, E_{γ_1} and E_{γ_2}, are reported in the second column (in keV). The parameters a_2^{exp} and a_4^{exp} obtained from the linear fit of the correlations are presented, together with the reduced χ^2 values of such fits. The uncertainty on the a_2^{exp} and a_4^{exp} values has been inflated to take into account the excess above unity of the reduced χ^2 value. In the last column, the covariance matrix C between a_2 and a_4 is presented for each fit.

Nucleus	E_{γ_1}-E_{γ_2}	a_2^{exp}	a_4^{exp}	χ^2/ν	C
^{72}Ge	630-834	$-0.104(2)$	$0.327(3)$	1.473	$\begin{pmatrix} 3.878 \times 10^{-6} & 4.744 \times 10^{-7} \\ 4.744 \times 10^{-7} & 6.328 \times 10^{-6} \end{pmatrix}$
^{74}Ge	608-596	$-0.2691(14)$	$0.294(2)$	1.696	$\begin{pmatrix} 1.155 \times 10^{-6} & 9.78 \times 10^{-8} \\ 9.78 \times 10^{-8} & 1.884 \times 10^{-6} \end{pmatrix}$
^{76}Ge	546-563	$-0.3096(12)$	$0.2539(15)$	1.502	$\begin{pmatrix} 9.002 \times 10^{-7} & 5.723 \times 10^{-8} \\ 5.723 \times 10^{-8} & 1.448 \times 10^{-6} \end{pmatrix}$
^{78}Ge	567-619	$-0.2847(12)$	$0.178(2)$	1.796	$\begin{pmatrix} 8.709 \times 10^{-7} & 7.901 \times 10^{-8} \\ 7.901 \times 10^{-8} & 1.419 \times 10^{-6} \end{pmatrix}$

BIBLIOGRAPHY

[1] Heyde, K. & Wood, J. L. Shape coexistence in atomic nuclei. *Rev. of Mod. Phys.* **83**, 1467(55) (2011). https://doi.org/10.1103/RevModPhys.83.1467.

[2] Wood, J. L. & Heyde, K. A focus on shape coexistence in nuclei. *Journal of Physics G: Nuclear and Particle Physics* **43**, 020402 (2016).

[3] Ayangeakaa, A. *et al.* Shape coexistence and the role of axial asymmetry in ^{72}Ge. *Physics Letters B* **754**, 254 – 259 (2016).

[4] Ayangeakaa, A. D. *et al.* Evidence for rigid triaxial deformation in ^{76}Ge from a model-independent analysis. *Phys. Rev. Lett.* **123**, 102501 (2019).

[5] Wood, J., Zganjar, E., De Coster, C. & Heyde, K. Electric monopole transitions from low energy excitations in nuclei. *Nuclear Physics A* **651**, 323 – 368 (1999).

[6] Garnsworthy, A. B. *et al.* The GRIFFIN facility for Decay-Spectroscopy studies at TRIUMF-ISAC. *Nuclear Instruments and Methods in Physics Research Section A: Accelerators, Spectrometers, Detectors and Associated Equipment* **918**, 9–29 (2019).

[7] Bohr, A. & Mottelson, B. *Nuclear Structure, Volume II: Nuclear Deformation* (World Scientific, Singapore, 1998).

[8] Ring, P. & Schuck, P. *The Nuclear Many-Body Problem* (Springer, Germany, 1980).

[9] Garrett, P. E. Characterization of the β vibration and 0_2^+ states in deformed nuclei. *Journal of Physics G: Nuclear and Particle Physics* **27**, R1–R22 (2000).

[10] Garrett, P. E., Wood, J. L. & Yates, S. W. Critical insights into nuclear collectivity from complementary nuclear spectroscopic methods. *Physica Scripta* **93**, 063001 (2018).

[11] Sharpey-Schafer, J., Bark, R., Bvumbi, S., Dinoko, T. & Majola, S. "Stiff" deformed nuclei, configuration dependent pairing and the β and γ degrees of freedom. *Eur. Phys. J. A* **55**, 15 (2019).

[12] Davydov, A. & Filippov, G. Rotational states in even atomic nuclei. *Nuclear Physics* **8**, 237–249 (1958).

[13] Wilets, L. & Jean, M. Surface oscillations in even-even nuclei. *Phys. Rev.* **102**, 788–796 (1956).

[14] Zamfir, N. & Casten, R. Signatures of γ softness or triaxiality in low energy nuclear spectra. *Physics Letters B* **260**, 265–270 (1991).

[15] Caurier, E., Martínez-Pinedo, G., Nowacki, F., Poves, A. & Zuker, A. P. The shell model as a unified view of nuclear structure. *Rev. Mod. Phys.* **77**, 427–488 (2005).

[16] Vautherin, D. & Brink, D. M. Hartree-Fock Calculations with Skyrme's Interaction. I. Spherical Nuclei. *Phys. Rev. C* **5**, 626 (1972).

[17] Vautherin, D. Hartree-Fock Calculations with Skyrme's Interaction. II. Axially Deformed Nuclei. *Phys. Rev. C* **7**, 296 (1973).

[18] Bender, M., Heenen, P.-H. & Reinhard, P.-G. Self-consistent mean-field models for nuclear structure. *Rev. Mod. Phys.* **75**, 121–180 (2003).

[19] Möller, P. *et al.* Axial and reflection asymmetry of the nuclear ground state. *Atomic Data and Nuclear Data Tables* **94**, 758–780 (2008).

[20] Möller, P., Sierk, A., Bengtsson, R., Sagawa, H. & Ichikawa, T. Nuclear shape isomers. *Atomic Data and Nuclear Data Tables* **98**, 149–300 (2012).

[21] Tsunoda, Y., Otsuka, T., Shimizu, N., Honma, M. & Utsuno, Y. Novel shape evolution in exotic Ni isotopes and configuration-dependent shell structure. *Phys. Rev. C* **89**, 031301 (2014).

[22] Shimizu, N. *et al.* New-generation Monte Carlo shell model for the K computer era. *Progress of Theoretical and Experimental Physics* **2012** (2012).

[23] Rutherford, E. & Soddy, F. XLI. The cause and nature of radioactivity. – Part I. *The London, Edinburgh, and Dublin Philosophical Magazine and Journal of Science* **4**, 370–396 (1902).

[24] Rutherford, E. & Soddy, F. LX. Radioactive Change. *The London, Edinburgh, and Dublin Philosophical Magazine and Journal of Science* **5**, 576–591 (1903).

[25] Krane, K. S. *Introductory Nuclear Physics* (John Wiley and Sons, Hoboken, 1988).

[26] Tiesinga, E., Mohr, P. J., Newell, D. B. & Taylor, B. N. The 2018 CODATA Recommended Values of the Fundamental Physical Constants (2020). Database developed by J. Baker, M. Douma, and S. Kotochigova. Available at `http://physics.nist.gov/constants`, National Institute of Standards and Technology, Gaithersburg, MD 20899.

[27] Frauenfelder, H. & Steffen, R. M. XIX. Angular Distribution of Nuclear Radiation – Angular Correlations. In Siegbahn, K. (ed.) *Alpha-, Beta- and Gamma-Ray Spectroscopy*, 997 – 1195 (North-Holland Publishing Company, Amsterdam, 1966).

[28] Krane, K. S. & Steffen, R. M. Determination of the $\frac{E2}{M1}$ Multipole Mixing Ratios of the Gamma Transitions in Cd^{110}. *Phys. Rev. C* **2**, 724–734 (1970).

[29] Bohr, A. & Mottelson, B. *Nuclear Structure, Volume I: Single-Particle Motion* (World Scientific, Singapore, 1998).

[30] Weisskopf, V. F. Radiative Transition Probabilities in Nuclei. *Phys. Rev.* **83**, 1073–1073 (1951).

[31] Church, E. L. & Weneser, J. Nuclear Structure Effects in Internal Conversion. *Annual Review of Nuclear Science* **10**, 193–234 (1960).

[32] Church, E. L. & Weneser, J. Electric-Monopole Transitions in Atomic Nuclei. *Phys. Rev.* **103**, 1035–1044 (1956).

[33] Dowie, J., Kibédi, T., Eriksen, T. & Stuchbery, A. Table of electronic factors for $E0$ electron and electron–positron pair conversion transitions. *Atomic Data and Nuclear*

Data Tables **131**, 101283 (2020).

[34] Browne, E. & Tuli, J. Nuclear Data Sheets for $A = 238$. *Nuclear Data Sheets* **127**, 191–332 (2015).

[35] Kantele, J. *et al.* Observation of an $E0$ Isomeric Transition from the ^{238}U Shape Isomer. *Phys. Rev. Lett.* **51**, 91–94 (1983).

[36] Kantele, J. *et al.* Reinvestigation of the gamma branch from the ^{238}U shape isomer. *Phys. Rev. C* **29**, 1693–1698 (1984).

[37] Brown, B. A., Garnsworthy, A. B., Kibédi, T. & Stuchbery, A. E. Microscopic method for $E0$ transition matrix elements. *Phys. Rev. C* **95**, 011301 (2017).

[38] Evitts, L. *et al.* Identification of significant $E0$ strength in the $2^2_+ \rightarrow 2^+_1$ transitions of ^{58,60,62}Ni. *Physics Letters B* **779**, 396–401 (2018).

[39] Walker, P. & Dracoulis, G. Energy traps in atomic nuclei. *Nature* **399**, 35 (1999).

[40] Singh, B. Nuclear Data Sheets update for $A = 76$. *Nuclear Data Sheets* **74**, 63–164 (1995).

[41] Singh, B. & Farhan, A. R. Nuclear Data Sheets update for $A = 74$. *Nuclear Data Sheets* **107**, 1923–2102 (2006).

[42] Abriola, D. & Sonzogni, A. Nuclear Data Sheets update for $A = 72$. *Nuclear Data Sheets* **111**, 1–140 (2010).

[43] Farhan, A. R. & Singh, B. Nuclear Data Sheets update for $A = 78$. *Nuclear Data Sheets* **110**, 1917–2080 (2009).

[44] Kibédi, T., Wood, J. L. & Garnsworthy, A. B. Publication in preparation.

[45] Gürdal, G. & McCutchan, E. Nuclear data sheets for a = 70. *Nuclear Data Sheets* **136**, 1–162 (2016).

[46] Ardouin, D. *et al.* Study of ^{72}Ge with the $^{71}\mathrm{Ga}(^3\mathrm{He}, d)^{72}\mathrm{Ge}$ reaction. *Phys. Rev. C* **11**, 1649–1657 (1975).

[47] Vergnes, M. N. *et al.* (p, t) reactions on ^{75}As and ^{74}Ge and the weak coupling core-excitation model. *Phys. Rev. C* **14**, 58–63 (1976).

[48] Ardouin, D., Hanson, D. L. & Stein, N. Alpha-particle transfer to 0^+ states in the germanium nuclei and the role of proton pairing correlations. *Phys. Rev. C* **22**, 2253–2257 (1980).

[49] Allmond, J. M. & Wood, J. L. Coupled generalized triaxial rotor model (GTRM$\times$2) code (2006). Unpublished.

[50] Toh, Y. *et al.* Evidence for rigid triaxial deformation at low energy in ^{76}Ge. *Phys. Rev. C* **87**, 041304 (2013).

[51] Forney, A. M. *et al.* Novel $\Delta J = 1$ Sequence in ^{78}Ge: Possible Evidence for Triaxiality. *Phys. Rev. Lett.* **120**, 212501 (2018).

[52] Sun, J. *et al.* Spectroscopy of ^{74}Ge: From soft to rigid triaxiality. *Physics Letters B* **734**, 308 – 313 (2014).

[53] Honma, M., Otsuka, T., Mizusaki, T. & Hjorth-Jensen, M. New effective interaction for f_5pg_9-shell nuclei. *Phys. Rev. C* **80**, 064323 (2009).

[54] Nikšić, T., Marević, P. & Vretenar, D. Microscopic analysis of shape evolution and triaxiality in germanium isotopes. *Phys. Rev. C* **89**, 044325 (2014). `https://doi.`

org/10.1103/PhysRevC.89.044325.

[55] Dilling, J., Krücken, R. & Ball, G. ISAC overview. *Hyperfine Interactions* **225**, 1–8 (2014).

[56] Bylinskii, I. & Craddock, M. K. The TRIUMF 500 MeV cyclotron: the driver accelerator. *Hyperfine Interactions* **225**, 9–16 (2014).

[57] TRIUMF Design Office.

[58] Dombsky, M. & Kunz, P. ISAC targets. *Hyperfine Interactions* **225**, 17–23 (2014).

[59] Bricault, P. G., Ames, F., Dombsky, M., Kunz, P. & Lassen, J. Rare isotope beams at ISAC—target & ion source systems. *Hyperfine Interactions* **225**, 25–49 (2014).

[60] Rizwan, U. *et al.* Characteristics of GRIFFIN high-purity germanium clover detectors. *Nuclear Instruments and Methods in Physics Research Section A: Accelerators, Spectrometers, Detectors and Associated Equipment* **820**, 126–131 (2016).

[61] Garnsworthy, A. B. *et al.* The GRIFFIN data acquisition system. *Nuclear Instruments and Methods in Physics Research Section A: Accelerators, Spectrometers, Detectors and Associated Equipment* **853**, 85 – 104 (2017).

[62] Olaizola, B. *et al.* Shape coexistence in the neutron-deficient lead region: A systematic study of lifetimes in the even-even $^{188-200}$Hg with the GRIFFIN spectrometer at TRIUMF. *Phys. Rev. C* **100**, 024301 (2019).

[63] Ritt, S. & Amaudruz, P.-A. In *Proceedings of the 10th IEEE Real Time Conference, Beaune*, 309 (1997).

[64] GRIFFIN Data Format Specification. https://rawgit.com/wiki/GriffinCollaboration/GRSISort/technical-docs/GRIFFIN_Event_Format.pdf.

[65] Martin, M. Nuclear Data Sheets for $A = 152$. *Nuclear Data Sheets* **114**, 1497–1847 (2013).

[66] Duchene, G. *et al.* The Clover: a new generation of composite Ge detectors. *Nucl. Instr. and Meth. A* **432**, 90 (1999).

[67] Radford, D. ESCL8R and LEVIT8R: Software for interactive graphical analysis of HPGe coincidence data sets. *Nuclear Instruments and Methods in Physics Research Section A: Accelerators, Spectrometers, Detectors and Associated Equipment* **361**, 297–305 (1995).

[68] Kibédi, T., Burrows, T., Trzhaskovskaya, M., Davidson, P. & Nestor, C. Evaluation of theoretical conversion coefficients using BrIcc. *Nuclear Instruments and Methods in Physics Research Section A: Accelerators, Spectrometers, Detectors and Associated Equipment* **589**, 202 – 229 (2008).

[69] Bender, P., Dunlop, R., Bildstein, V., Smith, J. & Miller, D. GRSISort – A lean, mean, sorting machine. DOI: 10.5281/zenodo.3520948.

[70] Brun, R. & Rademakers, F. ROOT – An Object Oriented Data Analysis Framework. In *AIHENP'96 Workshop, Lausane*, vol. 389, 81–86 (1996). http://root.cern.ch/.

[71] Smallcombe, J. jROOT Tools. DOI: 10.5281/zenodo.3546313.

[72] Radford, D. RadWare. https://radware.phy.ornl.gov.

[73] Biedenharn, L. C. & Rose, M. E. Theory of angular correlation of nuclear radiations. *Rev. Mod. Phys.* **25**, 729–777 (1953).

[74] Robinson, S. How reliable are spins and δ-values derived from directional correlation experiments? *Nuclear Instruments and Methods in Physics Research Section A: Accelerators, Spectrometers, Detectors and Associated Equipment* **292**, 386 – 400 (1990).

[75] Smith, J. *et al.* Gamma–gamma angular correlation analysis techniques with the GRIFFIN spectrometer. *Nuclear Instruments and Methods in Physics Research Section A: Accelerators, Spectrometers, Detectors and Associated Equipment* **922**, 47 – 63 (2019).

[76] Natzke, C. Private communication.

[77] Kibédi, T. & Spear, R. Electric monopole transitions between 0^+ states for nuclei throughout the periodic table. *Atomic Data and Nuclear Data Tables* **89**, 77 – 100 (2005).

[78] Winter, G. & Sodan, H. $E0/E2$ Mischungsverhältnisse beim Übergang von Betavibrationsniveaus in deformierten Kernen mit ungerader Nukleonenzahl. *Nuclear Physics A* **114**, 629–635 (1968).

[79] Kibédi, T., Dracoulis, G., Byrne, A. & Davidson, P. Low-spin non-yrast states and collective excitations in ^{174}Os, ^{176}Os, ^{178}Os, ^{180}Os, ^{182}Os and ^{184}Os. *Nuclear Physics A* **567**, 183–236 (1994).

[80] Church, E. L., Rose, M. E. & Weneser, J. Electric-Monopole Directional-Correlation Experiments. *Phys. Rev.* **109**, 1299–1306 (1958).

[81] Kibédi, T. *et al.* Publication in preparation.

[82] Lafarge, T. & Possolo, A. The NIST Uncertainty Machine. *NCSLI Measure* **10**, 20–27 (2015). `https://uncertainty.nist.gov`.

[83] Tuli, J. K. *The Evaluated Nuclear Structure Data File. A Manual for Preparation of Data Sets*. National Nuclear Data Center, Brookhaven National Laboratory (2001). `https://www.osti.gov/biblio/779777`.

[84] Kulp, W. D. *et al.* $N = 90$ region: The decays of $^{152}\mathrm{Eu}^{m,g}$ to $^{152}\mathrm{Sm}$. *Phys. Rev. C* **76**, 034319 (2007).

[85] Currie, L. A. Limits for qualitative detection and quantitative determination. Application to radiochemistry. *Analytical Chemistry* **40**, 586–593 (1968).

[86] Gilmore, G. *Practical Gamma-ray Spectrometry – 2nd Edition* (John Wiley and Sons, Chichester, 2008).

[87] Morand, C. *et al.* Niveaux de spin éléve du ^{72}Ge atteints par la réaction ^{70}Zn(α,2nγ) à E$_\alpha$ = 30 MeV. *Nuclear Physics A* **313**, 45 – 76 (1979).

[88] Mukhopadhyay, S. *et al.* Nuclear structure of $^{76}\mathrm{Ge}$ from inelastic neutron scattering measurements and shell model calculations. *Phys. Rev. C* **95**, 014327 (2017).

[89] Passoja, A., Vergnes, M., Kantele, J. & Luontama, M. Electric monopole strengths in even-mass Ge and Se isotopes. *Physica Scripta* 147–148 (1983).

[90] Lecomte, R. *et al.* Coulomb-excitation studies of $^{70}\mathrm{Ge}$, $^{72}\mathrm{Ge}$, $^{74}\mathrm{Ge}$, and $^{76}\mathrm{Ge}$. *Phys. Rev. C* **22**, 2420–2423 (1980).

[91] Chou, W.-T., Brenner, D. S., Casten, R. F. & Gill, R. L. Level lifetime measurements and the structure of neutron-rich $^{78}\mathrm{Ge}$. *Phys. Rev. C* **47**, 157–162 (1993).

[92] Wood, J. L., Oros-Peusquens, A.-M., Zaballa, R., Allmond, J. M. & Kulp, W. D. Triaxial rotor model for nuclei with independent inertia and electric quadrupole tensors. *Phys. Rev. C* **70**, 024308 (2004).

[93] Allmond, J. M. & Wood, J. L. Generalized triaxial rotor model (GTRM) code (2005). Unpublished.

[94] Allmond, J. M. Private communication.

[95] Fortune, H. T. Coexistence and $B(E2)$ values in ^{72}Ge. *Phys. Rev. C* **94**, 024318 (2016).

ACKNOWLEDGMENTS

I would like to thank Silvia Leoni for the constant support she provided me over the years.

I would like to thank Adam Garnsworthy for the care and dedication he put in my supervision. Thanks for everything you taught me, for the encouragement, and for always letting me the space to speak up my mind.

Thanks to Paul Garrett and Adriana Nannini for their constructive comments and corrections to my thesis.

I am grateful for having worked within the GRIFFIN and TIGRESS collaboration, which has been a vivacious and fruitful environment. In particular, thanks to Stephen Gillespie for his attentive support, to Connor Natzke for providing me with the GEANT4 simulations that I used in this work, to Gordon Ball for the time he devoted to helping me out with the angular correlation analysis, and to James Smallcombe for his prompt replies to all my numerous questions, especially the last-minute ones.

Thanks to Xavier Roca Maza and Gianluca Colò for their patient explanations.

Thanks to my dear friends and colleagues Chris Griffin, Daniel Yates, Bruno Olaizola and Marta Polettini, for sharing with me the ups and downs of this long journey and for helping keep me lighthearted throughout the process.

I am grateful for having reached the end of this journey, and let another one begin.